Transport Phenomena in Two-Dimensional Lorentz Gases

Inaugural-Dissertation

zur Erlangung des Doktorgrades der
Mathematisch-Naturwissenschaftlichen Fakultät der
Heinrich-Heine-Universität Düsseldorf

vorgelegt von

Benjamin Ahlin Sanvee

aus Düsseldorf

Düsseldorf, November 2022

aus dem Institut für Theoretische Physik II : Weiche Materie
der Heinrich-Heine-Universität Düsseldorf

Gedruckt mit der Genehmigung der
Mathematisch-Naturwissenschaftlichen Fakultät der
Heinrich-Heine-Universität Düsseldorf

Berichterstatter:

1. Prof. Dr. Jürgen Horbach

2. Prof. Dr. Thomas Heinzel

Tag der mündlichen Prüfung: 21.12.2022

Acknowledgements

I would like to thank Prof. Dr. Jürgen Horbach for his guidance and supervision of this work: It was great working with you! I really enjoyed the friendly and helpful atmosphere at our institute that I will keep in good memories.

Furthermore, I want to thank my second supervisor Prof. Dr. Heinzel for the fruitful discussions we had. It helped me understanding the experimental aspects of this work.

My gratitude also goes to Prof. Eivind Hiis Hauge in Trondheim Norway, who sent me a copy of Ref. [1] via snail mail.

A special thanks goes to my wife Julia. She sacrificed her sleep by taking care of our two little daughters literally every night, so I would be fit in the morning.

I also want to thank everyone else at our institute, especially Stefanie, who helped with all the administrative stuff and also Jo, for his advices concerning nearly everything.

Abstract

πάντα ῥεῖ. In this thesis, we investigate the movement of tracer particles in a two-dimensional plane where randomly distributed fixed obstacles are placed. This system is called a Lorentz gas and is a model system for transport in heterogeneous media. It can exhibit normal and anomalous diffusion depending on the geometry of the obstacles and the obstacle density. For square obstacles all oriented in the same direction and allowed to overlap, the system exhibits anomalous diffusion as the diffusion coefficient vanishes and the mean squared displacements shows sub-diffusive behaviour. In the non-overlapping case, the diffusion is normal. This system is called Ehrenfests' wind-tree model (EWTM). In the case of non-overlapping obstacles, we have computed the third-order term in the density expansion of the diffusion constant. In the EWTM with overlapping obstacles, we show that the mean squared displacement has a density-dependent exponent. This settles the open question about the asymptotic behaviour of the tracer particles in the EWTM with overlapping obstacles. Furthermore, we propose a closed functional form for the van Hove correlation function in the EWTM with overlapping obstacles.

For circular obstacles, the dynamics of the tracer particles are chaotic and one observes normal diffusion in the long-time limit. If a magnetic field is switched on perpendicularly to the Lorentz gas, it then mimics the classical transport of electrons in a two-dimensional electron gas (2DEG) with obstacles. These systems can be realised experimentally and we compare our simulation results with experimental measurements performed in the group of Prof. Heinzel at the Heinrich-Heine University of Düsseldorf. We investigate the robustness of the predictions of the Drude theory for higher densities. Moreover, we analysed the behaviour of the EWTM at low fields where we observe a reversal of the Hall resistance.

As the density of the obstacles is increased, the system undergoes a delocalisation-to-localisation transition at the percolation transition of the free area. At the percolation threshold, an infinite cluster of obstacles traverses the system. This cluster has a fractal structure and the tracer particles

exhibit anomalous diffusion. In the presence of a magnetic field, a second percolation threshold appears. This is due to the fact that for sufficiently large magnetic fields and low densities, the particles are trapped in the vicinity of the obstacles. For circular obstacles, the critical densities are known analytically, but for arbitrary geometries the critical density of this field-induced transition is not known. We have devised a method to compute the critical density of this second percolation transition for any geometrical shape. We have computed the phase diagram for the EWTM in the presence of a magnetic field and computed the universal exponent of the mean squared displacement at both percolation transitions. We find that both transitions are not in the same universality class in agreement with an earlier simulation study.

Zusammenfassung

πάντα ῥεῖ. In dieser Arbeit untersuchen wir die Bewegung von Tracer-Teilchen auf einer zweidimensionalen Fläche, auf der zufällig verteilte, unbewegliche Hindernisse platziert sind. Dieses System nennt sich Lorentzgas und ist ein Modell für den Transport in heterogenen Medien. In Lorentzgasen beobachtet man sowohl normale als auch anomale Diffusion. Dies hängt von der Dichte und der Geometrie der Hindernisse ab. Systeme mit gleich ausgerichteten quadratischen Hindernissen, die sich überlappen, weisen eine anomale Diffusion der Tracer-Teilchen auf: Der Diffusionskoeffizient verschwindet und das mittlere Verschiebungsquadrat weist ein subdiffusives Verhalten auf. Im nicht überlappenden Fall ist die Diffusion normal. Bei diesem System handelt es sich um das Ehrenfestsche Wind-Tree Modell (EWTM). Für den Fall nicht überlappender Hindernisse haben wir die dritte Ordnung in der Dichteentwicklung der Diffusionskonstante errechnet. Im Fall überlappender Hindernisse zeigen wir, dass das mittlere Verschiebungsquadrat einen dichteabhängigen Exponenten aufweist. Hiermit klären wir die Frage des asymptotischen Verhaltens der Tracer-Teilchen im EWTM mit überlappenden Hindernissen. Des Weiteren schlagen wir einen Ausdruck für die Van-Hove-Korrelationsfunction im EWTM mit überlappenden Hindernissen vor.

Für kreisförmige Hindernisse ist die Dynamik der Tracer-Teilchen chaotisch und wir beobachten normale Diffusion im Langzeit-Limes. In Anwesenheit eines Magnetfeldes senkrecht zur Ebene des Lorentzgases, ahmt das System den Magnetotransport von Elektronen in einem zweidimensionalen Elektronengas (2DEG) in Anwesenheit von Hindernissen nach. Diese Systeme können experimentell realisiert werden. Entsprechende Experimente wurden in der Gruppe von Prof. Heinzel an der Heinrich-Heine Universität Düsseldorf durchgeführt. Wir untersuchen an ihnen die Robustheit der Drude-Theorie bezüglich der Vorhersage des Hallkoeffizienten. Des Weiteren untersuchen wir das Verhalten des EWTMs bei kleinen Dichten und beobachten dort einen negativen Hallwiderstand.

Wird die Dichte der Hindernisse erhöht, durchläuft die freie Fläche einen

Lokalisierungsübergang an der Perkolationsschwelle. Es bildet sich ein unendlich zusammenhängendes Gebiet von Hindernissen aus (Cluster). An der Perkolationsschwelle hat der Cluster eine fraktale Struktur und das System weist anomalen Transport auf. In Anwesenheit eines Magnetfeldes entsteht eine zweite Perkolationsschwelle. Dies ist darauf zurückzuführen, dass die Tracer-Teilchen wegen ihrer kreisförmigen Trajektorien nicht mehr in der Lage sind, sich beliebig weit von der Oberfläche der Hindernisse zu entfernen. Dadurch können sie sich nicht mehr durch das komplette System bewegen. Bei genügend niedriger Dichte und hohem Magnetfeld sind sie in der Umgebung der Hindernisse lokalisiert. Für kreisförmige Hindernisse ist der analytische Ausdruck für diese Perkolationsschwellen bekannt, für beliebige Obstacle-Geometrien hingegen nicht. Wir haben eine Methode entwickelt, um die Perkolationsschwellen dieses Übergangs zu berechnen. Mit dieser Methode konnten wir das Phasendiagramm des EWTM bestimmen. Die kritischen Exponenten an beiden Perkolationsschwellen konnten somit bestimmt werden. Wir konnten herausfinden, dass beide Übergänge nicht dasselbe universelle Verhalten aufweisen. Dies ist im Einklang mit einer vorherigen Studie.

Contents

1 Introduction

The fact that a model is soluble is always due to some particular simplifying features, and precisely those features can be decisive for the answers to the questions asked. [2]

— **E.H. Hauge** —

Transport phenomena are ubiquitous. Examples are colloid diffusion in porous media [3–10], the mechanisms of virus spread [11], transport mechanisms in biological cells [12], or the dynamics of financial markets [13–16]. The description of these phenomena is the endeavour of non-equilibrium statistical mechanics. Pioneering work has been done by Boltzmann who proposed the reality of atoms [17–19] and shaped the very foundations of the kinetic theory of gases and of all statistical mechanics. It is on that atomistic basis that Albert Einstein in 1905 [20] derived his theory of the Brownian motion observed in 1827 by the botanist Robert Brown [21]. Brown discovered that pollen immersed in water fulfil a jittery random motion. Einstein found a physical explanation of this phenomenon by assuming that this motion is due to random collisions with the water molecules. Let $f(x,t)$ be the one-dimensional probability distribution of finding a particle at position x at time t. Einstein derived that for particles subjected to random uncorrelated collisions, the distribution function is a solution of the diffusion equation

$$\frac{\partial f(x,t)}{\partial t} = D\frac{\partial^2 f(x,t)}{\partial x^2}, \tag{1.1}$$

where x is the particle position and D the diffusion constant. For simplicity we consider the problem in one dimension, but the results are identical in

three dimensions. By assuming N particles located at position $x = 0$ at time $t = 0$, the solution of this equation is given by

$$f(t, x) = \frac{N}{\sqrt{4\pi Dt}} \exp\left\{-\frac{x^2}{4Dt}\right\}. \tag{1.2}$$

It is a Gaussian distribution centred at $x = 0$ with variance $\sigma = 2Dt$. At the initial time $t = 0$, one has a delta peak that is the limit of a Gaussian distribution with vanishing variance. Then, at times $t > 0$, the Gaussian function broadens and its maximum decays. The Gaussian form of the distribution can be justified by the central limit theorem. On a microscopic level, a particle is subjected to random displacements due to the collisions with the molecules of the solvent. If one looks at the system at regular times intervals $\delta t \gg \tau$, where τ is the mean collision time of the solvent molecules with the particles, then one sees a series of random independent displacements X_i where i is the i^{th} time interval. The position of the particle up to an arbitrary time t is then the sum $S_t = \sum_i X_i$ of these displacements. We assume that there is no drift in the system and therefore, the mean displacement over many realisations $\langle X_i \rangle$ is zero. Also, the variance of the distribution of the displacements is assumed to be finite , meaning that arbitrarily large displacements are considered to be sufficiently improbable. With these assumptions the central limit theorem states that S_t is a random variable with a Gaussian distribution [22]. For the central limit theorem to be valid [22], the displacements X_i must be independent. Thus, if the particle keeps a memory of its former displacements (the displacements are no more independent of each other), or the displacements are dependent on the actual position of the particle, the central limit theorem does not apply and one is faced with anomalous diffusion. For many systems, one is faced with anomalous diffusion at intermediate timescales. Transient memory effects can for example be due to the local behaviour of the particles in biological systems [23, 24]. In this case, the anomalous diffusion is a transient phenomenon as opposed to anomalous diffusion in the limit $t \to \infty$ as we will encounter in this thesis. The second moment or variance of $f(x, t)$ is called the mean squared displacement δx^2. It is proportional to the time t in the case of normal diffusion:

$$\delta x^2 = 2Dt. \tag{1.3}$$

In the case of anomalous diffusion the relationship between the mean squared displacement and time is no longer linear. Writing $\Delta_x^2 \propto t^\alpha$, one speaks of superdiffusion if $\alpha > 1$. The particles exhibit subdiffusive behaviour if $\alpha < 1$.

With the advent of semiconductors, especially transistors and new materials like graphene, transport phenomena in two-dimensional media became

an important field of research. One is for example interested in the transport properties of electrons in these materials. One way to model the transport of particles in a two-dimensional plane is the two-dimensional Lorentz gas. It can exhibit both normal and anomalous diffusion, and due to its simplicity it is still accessible to theoretical exploration and investigation via computer simulations [25–29]. It can also be investigated experimentally as a two-dimensional electron gas in a semiconductor heterostructure with obstacles [29–33].

The two-dimensional Lorentz gas consists of non-interacting point particles moving on a infinite plane on which fixed scatterers/obstacles are placed. The tracer particles are reflected i.e. collide elastically with the boundaries of the obstacles. In this thesis, we consider the case of identical randomly placed obstacles. Historically the Lorentz gas with circular scatterers was first used in an attempt by Hendrik Antoon Lorentz to explain the heat conductivity of metals [34]. Apart from this, the Lorentz model has received an extensive theoretical investigation (see for example [35–39]) to shed light on multiple aspects of linear transport theory. Especially, it has been proven by Galavotti [40] that the Lorentz gas can be modelled via the linear Boltzmann equation at low densities. In the Grad limit, that is in the limit of vanishing obstacle radius but constant mean free path [41], it exhibits normal diffusion. In Ehrenfests' wind-tree model [42], a Lorentz gas with equally oriented quadratic obstacles, subdiffusive behaviour arises in the case of overlapping obstacles in the asymptotic long-time limit. This is due to the geometry of the obstacles and has been investigated with a kinetic theoretical approach by Hauge and Cohen [1, 2, 43, 44] whose results have been hinted at, but not conclusively settled by numerical simulations done by Wood and Lado [25]. In this thesis, we will extensively simulate the wind-tree model and compare our results to the theoretical predictions of Hauge, Cohen and van Beyeren [43, 45].

In the presence of a magnetic B-field perpendicular to the plane of the Lorentz gas, a transverse current, the Hall current, arises [46]. The transport of the tracer particles is now described by a diffusion tensor D_{ij} (with $i, j = x, y$). The Hall effect is used in many technological applications like Hall sensors to detect magnetic fields. In the Drude model, valid in the low-density limit, the interactions between the tracer particles and the obstacles are described on a coarse grained scale as a friction and the relationship between the applied magnetic field and the Hall resistance is linear. Although the Drude theory has been superseded by more involved theories [47–50] that take into account the memory effects introduced by the presence of a magnetic field [51–53], the predictions of the Hall coefficient by the Drude model are quite robust at higher densities. In this thesis, we shall investigate

this phenomenon and also compare our results with experiments conducted on a two-dimensional electron gas with circular obstacles.

With increasing density, the tracer particles are hindered to traverse the entire system. In an infinite system, the maximal density ρ_c where a particle can move trough the whole system is called the percolation threshold. At the percolation threshold an infinite cluster of obstacles forms that has a fractal structure and the diffusion becomes anomalous. The behaviour of the system in the vicinity of the percolation threshold exhibits universal behaviour. If we define the percolation threshold with ρ_c, and the distance from the percolation threshold as

$$\epsilon = \frac{\rho_c - \rho}{\rho_c}, \tag{1.4}$$

where ρ is the actual density of the system, the diffusion coefficient vanishes as

$$D(\rho) \propto \epsilon^{\mu}, \tag{1.5}$$

for $\epsilon > 0$. The exponent μ is only dependent on the dimensionality of the Lorentz gas and does not depend on the geometrical details of the obstacles and the trajectories. In the presence of a magnetic field the tracer particles cannot move as far as two times the cyclotron radius from the obstacles edges. At low densities the average distance between the obstacles increases, the tracer particles cannot traverse the system because they become trapped on isolated islands of obstacles. Therefore, a second B-field-induced percolation transition arises [54]. In this thesis, we compute the phase diagram of the wind-tree model with regard to the field-induced percolation transition. Furthermore, we will compare the exponents at both percolation transitions.

In the following, this thesis will be organized into five main chapters. After this introduction, in **chapter 2**, we will introduce the Lorentz model and discuss the correlation functions computed in the simulations and the information one can extract from them in order to describe the transport properties of the tracer particles. Furthermore we describe the experimental realisation of the Lorentz gas as a two-dimensional electron gas. In **chapter 3**, the theoretical models of the two-dimensional Lorentz gas will be discussed. We start with the simple Drude model and then we derive the linear Boltzmann equation heuristically, and we present the more general Ansatz of Bobylev [47–49]. We shall then turn our attention to the results of the kinetic theory of the wind-tree model by Hauge and Cohen [1, 43]. Finally, we discuss the fundamental properties of the Lorentz gas in the vicinity of the percolation threshold, especially the universal behaviour of the mean squared displacement and the diffusion coefficient. In **chapter 4**, we will present the

computational methods used for the simulations. We will review the handling of the boundary conditions and the implementation of the neighbour lists to speed up the computations. Here, we also show how to overcome the numerical difficulties that arose due to the finite precision of computer arithmetic. Moreover, the method used by Mertens *et al.* [55] to compute the percolation transition is presented and we show how to adapt this method for the computation of the B-field-induced transition. In **chapter 5**, we will present the results of my studies. We begin the chapter by presenting the results of the wind-tree model with non overlapping and overlapping obstacles. Then, we will focus on the Hall effect in the Lorentz gas in the presence of a magnetic field. In the last part, we will present the universal exponents obtained at magnetic-field-induced percolation transition.

2 The Lorentz Gas

In this chapter, we will first consider the Lorentz gas as a theoretical model and give an overview of the quantities needed to characterize the transport properties of the tracer particles. In the second part, we will discuss the experimental realisation of the Lorentz gas as a two-dimensional electron gas (2DEG) with depleted regions acting as the obstacles.

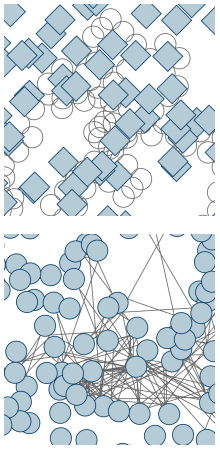

Figure 2.1 Example of tracer trajectories. Top: circular trajectories in the presence of a magnetic field with oriented square obstacles. Bottom: linear trajectory with circular obstacles

2.1 The Lorentz Gas Model

As stated earlier, the two-dimensional Lorentz gas consists of N random distributed immovable obstacles (see figure 2.1) at positions $\mathbf{r}_i$ where $i = 1, \ldots, N$. The vector $\mathbf{r}_i$ points to the centre of obstacle i taken to be its geometric centroid. Between the obstacles non-interacting point particles (tracer particles) move according to Newton's laws of mechanics until they are reflected specularly on the contour lines of the obstacles. The magnitude of the initial velocity $\mathbf{v}_0$ of all tracer particles is set to be identical. Due to the nature of the interactions between the tracer particles and the obstacles, the velocity magnitude of the tracer particles does no change. We define the dimensionless density $\rho = n \cdot a$, where n is the number density of the obstacles and a the surface of an obstacle.

The transport coefficient of interest for the Lorentz gas is the diffusion coefficient D. It is related to the mean squared displacement (MSD) of each tracer particle by the Einstein relation

$$D = \lim_{t\to\infty} \frac{\delta r^2(t)}{2dt}, \tag{2.1}$$

where

$$\delta r^2(t) = \left\langle [\mathbf{r}(t) - \mathbf{r}(0)]^2 \right\rangle = \frac{1}{N} \sum_{i=1}^{N} \left\langle [\mathbf{r}_i(t) - \mathbf{r}_i(0)]^2 \right\rangle \tag{2.2}$$

is the MSD of the tracer particles, and d the dimensionality of the system. The average $\langle\cdot\rangle$ is taken over all possible different obstacles distributions, and all possible start positions of the tracer particles. For the sake of readability, we have written δr^2 instead of $\langle\delta r^2\rangle$. In the long time limit, in the diffusive case, the MSD is therefore proportional to the time:

$$\delta r^2 = 2dDt. \tag{2.3}$$

One can also relate the MSD to the velocity autocorrelation function [56] by noting that the displacement of a tracer particle during the time interval $[0, t]$ is given by the integral

$$\mathbf{r}(t) - \mathbf{r}(0) = \int_0^t \mathrm{d}\tau\ \mathbf{v}(\tau), \tag{2.4}$$

where $\mathbf{v}(\tau)$ is the velocity of the tracer particle at time τ. The mean-squared displacement can therefore be written as

$$\delta r^2(t) = \int_0^t \int_0^t \mathrm{d}\tau \mathrm{d}\tau'\ \langle \mathbf{v}(\tau)\mathbf{v}(\tau')\rangle. \tag{2.5}$$

One takes the time derivative of the equation above to obtain

$$\frac{\mathrm{d}}{\mathrm{d}t}\delta r^2(t) = \int_0^t \int_0^t \mathrm{d}\tau \mathrm{d}\tau'\ \langle \dot{\mathbf{v}}(\tau)\mathbf{v}(\tau')\rangle + \langle \mathbf{v}(\tau)\dot{\mathbf{v}}(\tau')\rangle \tag{2.6}$$

$$= 2\int_0^t \mathrm{d}\tau'\ \langle \mathbf{v}(t)\mathbf{v}(\tau')\rangle. \tag{2.7}$$

For a system in equilibrium, this average is independent of the time origin. One therefore sets τ as the time origin by substituting $s = t - \tau'$ to obtain

$$\frac{\mathrm{d}}{\mathrm{d}t}\delta r^2(t) = 2\int_0^t \mathrm{d}s\ \langle \mathbf{v}(s)\mathbf{v}(0)\rangle. \tag{2.8}$$

By combining equation (2.3) and (2.8), one obtains the Green-Kubo relation (2.9) for the diffusion coefficient:

$$D = \frac{1}{d}\int_0^\infty \mathrm{d}t\ \langle \mathbf{v}(0)\mathbf{v}(t)\rangle. \tag{2.9}$$

In the two-dimensional case the diffusion coefficient becomes a tensor:

$$D_{ij} = \frac{1}{d} \int_0^\infty dt \, \langle v_i(0) v_j(t) \rangle, \tag{2.10}$$

where v_i and v_j with $i, j \in \{x, y\}$ are the Cartesian components of the velocity vector of the tracer particle. We retrieve the longitudinal self diffusion coefficient in two dimensions as

$$D_{ii} = \frac{1}{2} \int_0^\infty dt \, \langle v_i(0) v_i(t) \rangle, \tag{2.11}$$

with $ii = xx$ or $ii = yy$. For the transversal or Hall diffusivity, one has

$$D_{yx} = -D_{xy} = \frac{1}{2} \int_0^\infty dt \, \langle v_x(0) v_y(t) \rangle. \tag{2.12}$$

We note that the off-diagonal elements of the diffusion tensor are only non-vanishing in the presence of a magnetic field component perpendicular to the xy-plane.

A more detailed picture of the behaviour of the tracer particles can be given by also resolving the spatial correlations over time. This information is encoded by the self-part of the van Hove correlation function defined as [57]:

$$G(\mathbf{r}, t) = \frac{1}{N} \left\langle \sum_{i=1}^{N} \delta(\mathbf{r} - (\mathbf{r}_i(t) - \mathbf{r}_i(0))) \right\rangle. \tag{2.13}$$

Here, the function $\delta(\cdot)$ is the two-dimensional Dirac delta function. Due to the spatial isotropy of the Lorentz gas, the van Hove correlation function has radial symmetry. Thus, in polar coordinates one has

$$G_s(r, t) = \int_0^{2\pi} \mathrm{d}\theta \, G_s(\mathbf{r}, t). \tag{2.14}$$

The second moment of the van Hove Correlation function returns the MSD:

$$\begin{aligned} \int \mathrm{d}\mathbf{r} \, \mathbf{r}^2 G_s(\mathbf{r}, t) &= \frac{1}{N} \int \mathrm{d}\mathbf{r} \, \mathbf{r}^2 \left\langle \sum_{i=1}^{N} \delta(\mathbf{r} - (\mathbf{r}_i(t) - \mathbf{r}_i(0))) \right\rangle \\ &= \frac{1}{N} \left\langle \sum_{i=1}^{N} \left[\mathbf{r}_i(t) - \mathbf{r}_i(0) \right]^2 \right\rangle \\ &= \delta r^2(t). \end{aligned} \tag{2.15}$$

Here, we have used the property $\int_\Omega \delta(x-a)f(x)\,\mathrm{d}x = f(a)$ if $a \in \Omega$. Assuming diffusive transport one can make a Gaussian ansatz in two dimensions:

$$G_s(\mathbf{r},t) = \mathcal{A}\exp\left\{-\left(\frac{r}{\Delta_r^2}\right)^2\right\} = \mathcal{A}\exp\left\{-\frac{1}{2}\left(\frac{r}{\sigma}\right)^2\right\}, \tag{2.16}$$

where $\sigma^2 = (1/2)\delta r^2$. The normalisation constant $\mathcal{A}$ is given by

$$\mathcal{A}^{-1} = \int_0^{2\pi}\mathrm{d}\phi\int_0^\infty r\,\mathrm{d}r\exp\left\{-\frac{r^2}{2\sigma^2}\right\} = \pi\delta r^2(t) = 2\pi\sigma^2. \tag{2.17}$$

If we set the tracer particles to be located at the origin at time $t = 0$, we can make the ansatz $G_s(r,0) = \delta(r)$ and the van Hove correlation function is a delta peak at the origin. For the asymptotic behaviour one has:

$$\lim_{r\to\infty} G_s(r,0) = \lim_{t\to\infty} G_s(r,0) = 0. \tag{2.18}$$

Therefore, in the diffusive case, one has a Gaussian distribution that becomes broader as a function of time, and the width of the distribution is described by the MSD.

On way to quantify the deviation from a Gaussian distribution is to use the fact that Gaussian distributions have vanishing moments m_n if n is odd. The even moments are given by:

$$m_{2k} = \int_0^{2\pi}\mathrm{d}\theta\int_0^r r\,\mathrm{d}r\,r^{2k}G_s(r,t). \tag{2.19}$$

Integrating the Gaussian ansatz for $G_s(\mathbf{r},t)$ in polar coordinates, one finds:

$$m_{2k} = 2^k k!(\delta r^2), \tag{2.20}$$

for $k \in \mathbb{N}$. The fourth moment is related to the second moment by $m_4 = 2m_2^2$. Therefore, in the case of a Gaussian distribution the difference $m_4 - 2m_2^2$ must vanish. This fact is used to define the non-Gaussian parameter [58]:

$$\alpha_2(t) = \frac{1}{2}\frac{m_4(t)}{m_2(t)^2} - 1 = \frac{1}{2}\frac{\delta r^4(t)}{[\delta r^2(t)]^2} - 1, \tag{2.21}$$

where $\delta r^4(t)$ is computed as

$$\delta r^4(t) = \frac{1}{N}\sum_{i=1}^{N}\left\langle[\mathbf{r}_i(t) - \mathbf{r}_i(0)]^4\right\rangle. \tag{2.22}$$

The non-Gaussian parameter measures the deviation of the displacement distribution from the Gaussian form, and therefore will serve as an indicator for anomalous diffusion in the limit $t \to \infty$.

Now that we have presented the quantities of interest in the Lorentz model, we shall review the experimental realisation of the Lorentz gas.

2.2 Experimental Realisation of the Lorentz Gas

A two-dimensional electron (2DEG) gas can be formed at the interface of two semiconductors. The experiments discussed in this thesis have been carried out by the group of Prof. Heinzel at the Institute of Experimental Condensed Matter Physics at the Heinrich-Heine University of Düsseldorf. A semiconductor heterostructure of GaAs (Gallium arsenide) and $Al_xGa_{1-x}As$ (Aluminium Gallium Arsenide) is used. The parameter $x \in [0, 1]$ represents the ratio of Aluminium atoms randomly replacing Gallium atoms and is used to tune the conduction band offset ΔE_c in such a manner that a quantum well forms at the interface of the heterostructure (see figure 2.3). This parameter is set to $x = 0.3$ in the experiments. This results in a conduction band offset of $\Delta E_c = 300$ meV between $Al_xGa_{1-x}As$ and GaAs [59] (see figure 2.3). The two semiconductors are grown on top of each other with a thin layer highly doped with silicon atoms (Si δ-layer, see figure 2.2) at 40 nm of the GaAs-$Al_{0.3}Ga_{0.7}As$ interface. The Fermi levels of both materials will equilibrate due to some of the doping electrons (about 10%, see chapt. 3.4.2 of Ref. [59]) diffusing into the GaAs substrate. As a consequence, the conduction band of GaAs bends upwards and that of $Al_{0.3}Ga_{0.7}As$ bends downwards resulting in the band structure depicted in figure 2.3. A triangular quantum well is formed at the interface and one can tune the parameter x and the doping density of the Si δ-layer in such a way that the equilibrated Fermi level E_F of the heterostructure lies above the bottom of the conduction band. The electrons from the doping layer can now occupy states in the potential well. Preferably only the lowest state E_0 must be occupied at low temperatures and therefore the system is engineered such that the Fermi level lies between the lowest and second lowest energy level of the quantum well. The system is built in such a way that the width of the potential well in the z-direction is comparable to the Fermi-wavelength of the electrons, leading to a size quantisation of the wave vectors in the z-direction. Therefore, in the z-direction, the movement of the electrons is highly confined whereas in the xy-plane the electrons form a two-dimensional electron gas (2DEG) with an effective electron mass of $m^* = 0.067m_e$ in GaAs, where m_e is the rest mass of the electrons. The dispersion relation of the 2DEG

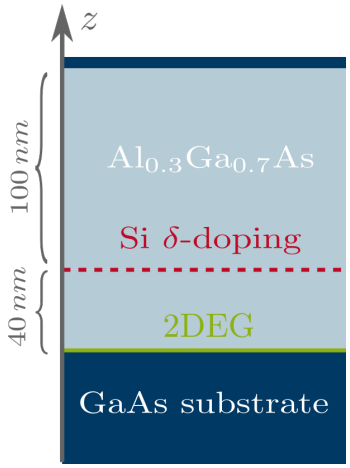

Figure 2.2 Cross-section of a GaAs-$Al_0.3Ga_{0.7}As$ heterojunction with a Si δ-layer.

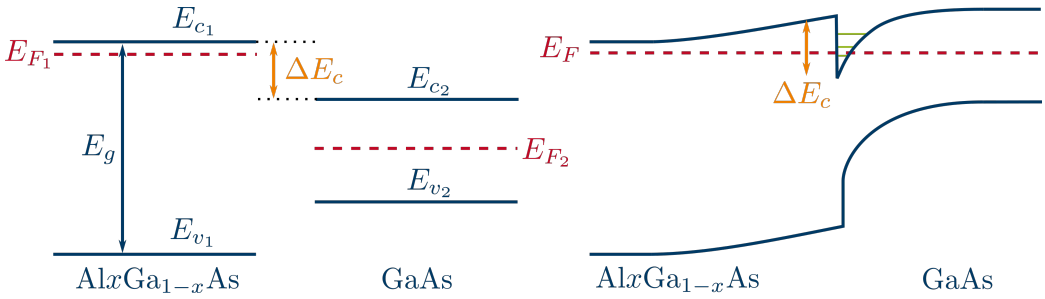

Figure 2.3 Band diagram of a GaAs-Al$_x$Ga$_{1-x}$As heterojuntion. On the left: Band diagrams of Al$_x$Ga$_{1-x}$As and GaAs without contact. E_{F_1} and E_{F_2} are the Fermi levels in both materials shown as red dotted lines. E_{c_1} and E_{c_2} denote the conduction band bottoms, E_{v_1} and E_{v_2} are the top of the valence band in both materials. The conduction band offset ΔE_c depends on the parameter x. On the right: when brought into contact, the Fermi levels equilibrate, the bands of both materials bend while conserving the band offsets at the junction. This results in a quantum well being formed at the interface. Figure adapted from [60].

corresponds to that of a free electron gas in two dimension:

$$\epsilon(\mathbf{k}) = E_0 + \frac{\hbar^2 \mathbf{k}^2}{2m^*}, \tag{2.23}$$

where $\mathbf{k} = (k_x, k_y)$ are the components of the wave vector in the xy-plane. The ground state energy E_0 corresponds to the lowest wave vector k_0 in the z-direction. In the experiments, the thermal energy of the electron is kept below the level spacing of 10meV in the quantum well, therefore no other state than the ground state in the z-direction will be occupied. The velocity of the current-carrying electrons can be assumed to be that of the Fermi velocity v_f at low temperatures and low applied electrical fields. Therefore, the velocity of all electrons can be considered identical and constant. This justifies the choice of a unique velocity magnitude of the tracer particles in the Lorentz gas simulations. In the experiments discussed in this thesis, $v_f \approx 2.1 \times 10^5$ ms^{-1} and the electron density n_e in the 2DEG is $n_e = 2.5 \times 10^{15}$ m^2 [30].

For this 2DEG to be considered as a Lorentz gas, further conditions must be met. Scattering mechanisms of the electrons must be reduced as much as possible. The scattering mechanisms of the electrons are of different nature:

- Scattering due to impurities close or at the interface. This is reduced by the crystal growing technique itself. The heterostructures used in the experiments are grown using molecular beam epitaxy [61]. This method takes place in ultra-high vacuum where the ultra pure solid elements are evaporated. The elements then slowly condense on the target wafer

allowing a build-up of the substrate atomic layer by atomic layer. This method produces ultra-pure samples with interfaces sharply defined on an atomic scale.

- Electrons can scatter at lattice imperfections. Especially at the interface between two different crystals, lattice mismatches occur that will scatter the electrons. The lattice mismatch between the two different components $Al_{0.3}Ga_{0.7}As$ and GaAs is only 0.4% (see chapt. 3.4.2. of Ref. [59]), and therefore this effect is mostly suppressed due to the choice of the materials.

- Scattering will also occur at the sites of the ionized Si donors. This is circumvented by the fact that the doping is bounded to a thin region that is spacially separated from the 2DEG [62]. Therefore, the electrons only see weak shielded potentials that scatter at small angles (see chapt. 3.4.2 of Ref. [59])

- Phonon scattering: This is mostly suppressed as the experiments are carried out at cryogenic temperatures $T < 1K$ [30].

A mean-free path of about 31μm in a 2DEG without obstacles has been achieved in the experiments.

The obstacles etched into the 2DEG have a dimension of the order of 1 μm [30]. In two dimensions, the Fermi wavelength of the electrons in the 2DEG is given by the relation [59]:

$$\lambda_f = \sqrt{\frac{2\pi}{n_e}}. \tag{2.24}$$

With the electron density given earlier, one finds $\lambda_f \approx 50$nm. This is much smaller than the obstacles dimensions and justifies the classical treatment of the electrons in the xy-plane. The obstacles correspond to holes in the 2DEG that form if one removes the doping layer via etching. This depletes the quantum well below the etched region and the electron density is zero. One has to note that the depleted area is slightly larger than the etched region. This depletion length needs to be taken into account as it increases the effective size of the obstacles. In the experiments considered in this thesis, the depletion length was estimated to be approximatively 75 nm [30]. The patterns of the holes are projected via electron beam lithography on the structure coated with a resist, then, the desired regions are etched away. A detailed explanation of the method can be found in reference [60]. These manufacturing procedures allow for sharp edges at which the electrons are scattered elastically.

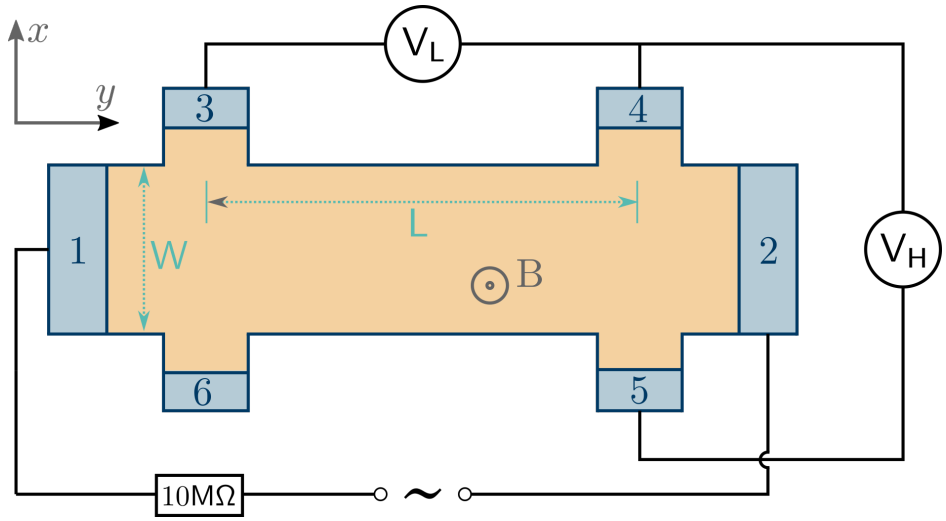

Figure 2.4 Sketch of a Hall bar geometry: The 2DEG is located in the yellow region. Ohmic contacts are attached in the blue zones to allow for injections of currents or voltage measurements. The applied B-field is perpendicular to the xy-plane. In the experimental setup an alternate current of 17Hz is injected between the contacts 1 and 2. Figure adapted from [60].

The final experimental setup is a 2DEG on a Hall bar (see figure 2.4). The 2DEG resides at about 150 nm [30] below the surface in the xy-plane (yellow area). Ohmic contacts have been added (blue areas) to be able to monitor the voltage drop along the system and inject currents. The quantities of interest are the longitudinal voltage drop $\mathsf{V_L}$ and the transversal/Hall voltage drop as response to an injected current. As one can see in figure 2.4, a low-frequency current (17 Hz) [60] is injected between the contacts 1 and 2. The longitudinal voltage is measured between contacts 3 and 4, and the Hall voltage between the contacts 4 and 5. Although the measurements could be carried out with a constant current, using a signal with a frequency reference enables the use of a lock-in amplifier and low pass filters to filter out the noise in the measurements [60]. The measured voltages are still related to the resistances via the common DC Ohms law as the phase shift between current and voltage is negligible at low frequencies. One has

$$\mathsf{R}_{xx} = \frac{\mathsf{V_L}}{\mathsf{I}} = \rho_{xx}\frac{\mathsf{L}}{\mathsf{W}}, \tag{2.25}$$

$$\mathsf{R}_{xy} = \frac{\mathsf{V_H}}{\mathsf{I}} = \rho_{xy}. \tag{2.26}$$

Here, ρ_{xx} and ρ_{xy} are the components of the magnetoresistivity tensor. I is the injected current, L and W are the length and width depicted in figure 2.4.

In the next chapter, it will be shown how to relate the components of the magnetoresistivity tensor ρ_{ij} to the components of the diffusion tensor D_{ij}. Furthermore, we shall explain how to relate the experimental results with the quantities obtained from the simulations.

3

Aspects of Transport Theory in the Lorentz Gas

In this Chapter, we will outline different transport theories of the Lorentz gas. To start, we present the Drude model, then, the Lorentz-Boltzmann model. Both theories assume uncorrelated collisions between the tracer particles and the obstacles. A more general Boltzmann equation derived by Bobylev *et al.* [48], that takes into account the memory effects due to the presence of a magnetic field, is then presented. We will also outline the kinetic theory of a special case of the Lorentz gas, namely Ehrenfests' wind-tree model. In this model, in the case of overlapping obstacles, memory effects cause anomalous diffusion in the limit $t \to \infty$. The end of the chapter will be dedicated to the anomalous diffusion in the vicinity of the percolation threshold in the Lorentz gas.

3.1 Drude Model

The empirical Wiedemann-Franz law

$$\frac{\kappa}{\sigma} \propto T. \tag{3.1}$$

states that the ratio between the heat conductance κ of a metal and its electric conductance σ is proportional to its temperature T and approximately the same for different materials. At the end of the 19th century, in an attempt to explain this law, Paul Drude build a microscopic model by considering free charged point particles and their interactions through collisions with a background of fixed ion cores [63]. Drude was not aware of the exact nature of those charged particles (we have to keep in mind that the Rutherford model dates from 1911 [64]). He assumed positively or negatively charged

currents [65]. It was Hendrik Antoon Lorentz in his paper of 1905 [34] who assumed one kind of charged particles with identical mass known today as the electron.

The main assumptions of this model are as follows [66]:

1. The electrons are considered to be point particles that behave as an ideal gas that moves between fixed ion cores.
2. The ion cores are considered to be hard spheres, and the only interactions between the electrons and the ion cores are instantaneous elastic collisions.
3. Between collisions, the electrons move according to Newton's equations of motion with or without an external field.
4. The collision events occur on average after a mean free time τ and are distributed according to a Poisson distribution.
5. After a collision, an electron has a random velocity direction.

With the assumptions above, we can derive an equation of motion for the electrons. As we have seen in section 2.2, all the electrons move with the Fermi velocity v_f. If we consider the average velocity $\langle \mathbf{v}_f \rangle$, it is clear that it is zero in the inertial frame of reference of the Lorentz gas, as all electrons move in random directions. If we apply a constant external electric field E, the electrostatic force $\mathbf{F} = -e\mathbf{E}$ will induce a drift velocity

$$\mathbf{v}(t) = -\frac{e\mathbf{E}t}{m_e}. \tag{3.2}$$

After the mean free time τ a collision with an ion core occurs that randomizes the built up drift velocity again. On average the drift velocity take the value of

$$\bar{\mathbf{v}} = -\frac{e\tau}{m_e}\mathbf{E}. \tag{3.3}$$

We shall note that the presence of a magnetic field $\mathbf{B}$ will not induce any drift as $\langle \mathbf{v}_f \rangle \times \mathbf{B} = 0$. The collisions of the electrons are now modelled by a frictional force that dissipates the energy and momentum gained during the average period of time τ. One therefore introduces a Stokes type friction term

$$\zeta\bar{\mathbf{v}} = \frac{m_e}{\tau}\bar{\mathbf{v}}, \tag{3.4}$$

and write down a Langevin equation without a noise term as equation of motion

$$m_e\frac{\mathrm{d}\bar{\mathbf{v}}}{\mathrm{d}t} = -e(\mathbf{E} + \bar{\mathbf{v}} \times \mathbf{B}) - \frac{m_e\bar{\mathbf{v}}}{\tau}. \tag{3.5}$$

In the absence of a magnetic field, and if one considers all the spatial directions to be isotropic, equation (3.5) becomes

$$m_e \frac{\mathrm{d}\bar{v}}{\mathrm{d}t} = -eE - \frac{m_e \bar{v}}{\tau}. \tag{3.6}$$

The steady state solution is found by setting $\mathrm{d}\bar{v}/\mathrm{d}t = 0$ and reads

$$\bar{v} = \frac{e\tau}{m_e} E = \mu E, \tag{3.7}$$

where $\mu = e\tau/m_e$ is called the electron mobility. It is the proportionality constant between the applied electric field and the average drift velocity of the electrons. By defining the current density $\mathbf{j} = en_e\bar{\mathbf{v}}$, where n_e denotes the electron density, we get the Ohm's law in the Drude model

$$j = \frac{n_e e^2 \tau}{m_e} E = n_e e \mu E = \sigma_0 E, \tag{3.8}$$

in one dimension, where σ_0 is called the zero-field Drude conductivity.

In the case of a two-dimensional Lorentz gas in the xy-plane subjected to a constant magnetic field in the z-direction $\mathbf{B} = (0, 0, B_z)$, equation (3.5) becomes

$$eE_x + v_y e B_z + \frac{m_e}{\tau} v_x = 0 \tag{3.9}$$

$$eE_y - v_x e B_z + \frac{m_e}{\tau} v_y = 0 \tag{3.10}$$

in the steady state. With the angular cyclotron frequency $\omega_c = \frac{eB}{m_e}$, one can rewrite the equations above in terms of the currents $j_x = en_e\bar{v}_x$, $j_y = en_e\bar{v}_y$ and the zero-field conductivity σ_0 leading to

$$E_x = \frac{1}{\sigma_0} v_x + \frac{\omega_c \tau}{\sigma_0} v_y \ , \tag{3.11}$$

$$E_y = -\frac{1}{\sigma_0} v_y + \frac{\omega_c \tau}{\sigma_0} v_x \ , \tag{3.12}$$

which has the matrix form

$$\begin{pmatrix} E_x \\ E_y \end{pmatrix} = \begin{pmatrix} \rho_{xx} & \rho_{xy} \\ \rho_{yx} & \rho_{yy} \end{pmatrix} \begin{pmatrix} j_x \\ j_y \end{pmatrix}, \tag{3.13}$$

where

$$\rho_{xx} = \rho_{yy} = \sigma_0^{-1} = \frac{m_e}{n_e e^2 \tau} = \rho_0, \tag{3.14}$$

and

$$\rho_{yx} = -\rho_{xy} = \frac{\omega_c \tau}{\sigma_0} = \frac{B}{e n_e} = R_H B. \tag{3.15}$$

Equation 3.13 has the form of Ohm's law

$$\mathbf{E} = \boldsymbol{\rho} \cdot \mathbf{j}, \tag{3.16}$$

where $\boldsymbol{\rho}$ is called the magnetoresistivity tensor. We can see that the longitudinal components $\rho_{xx} = \rho_{yy}$ are independent of the applied magnetic field and only depend on the scattering time τ. The transversal components $\rho_{yx} = -\rho_{xy}$ are linear in B where the slope $R_H = (n_e e)^{-1}$ is called the Hall coefficient.

The inverse of the magnetoresistivity tensor $\boldsymbol{\sigma} = \boldsymbol{\rho}^{-1}$ is called the magnetoconductivity tensor with which we can write Ohm's law as

$$\mathbf{j} = \sigma\, \mathbf{E}. \tag{3.17}$$

For the two-dimensional Lorentz gas, it is obtained by matrix inversion and reads in terms of ω_c and σ_0:

$$\sigma_{xx} = \sigma_0 \frac{1}{1 + \omega_c^2 \tau^2}, \tag{3.18}$$

$$\sigma_{xy} = \sigma_0 \frac{\omega_c \tau}{1 + \omega_c^2 \tau^2}, \tag{3.19}$$

where one also notes that $\sigma_{xx} = \sigma_{yy}$ and $\sigma_{xy} = -\sigma_{yx}$. The components of $\boldsymbol{\sigma}$ and $\boldsymbol{\rho}$ are plotted in figures 3.1 and 3.2. In numerical simulations, one extracts the components of the conductivity tensor from the velocity autocorrelation function and computes the magnetoresistance afterwards using the relationships

$$\rho_{xx} = \frac{\sigma_{xx}}{\sigma_{xx}^2 + \sigma_{xy}^2}, \tag{3.20}$$

and

$$\rho_{xy} = \frac{\sigma_{xy}}{\sigma_{xx}^2 + \sigma_{xy}^2}. \tag{3.21}$$

The components of the magnetoresistivity tensor ρ_{xx} and ρ_{xy} from above, are the quantities also extracted from the experiments (see equations 2.25 and 2.26). We shall see now how to relate these quantities to the results of the simulations. This is done by noting the fundamental relation between the diffusion tensor and the conductivity [67]:

$$\sigma_{ij} = \frac{n_e e^2}{m^* v_0^2} D_{ij}. \tag{3.22}$$

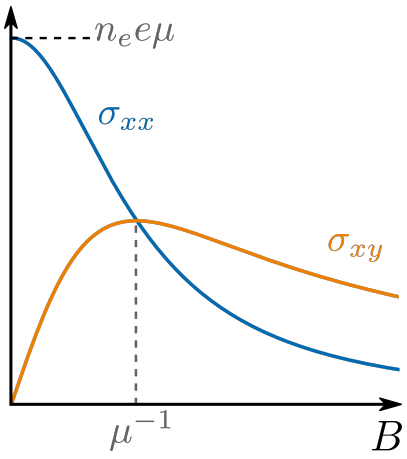

Figure 3.1 Components of the magnetoconductivity tensor for the two-dimensional electron gas. For $B = \mu^{-1}$ one gets $\sigma_{xx} = \sigma_{xy}$, in the framework of the Drude theory

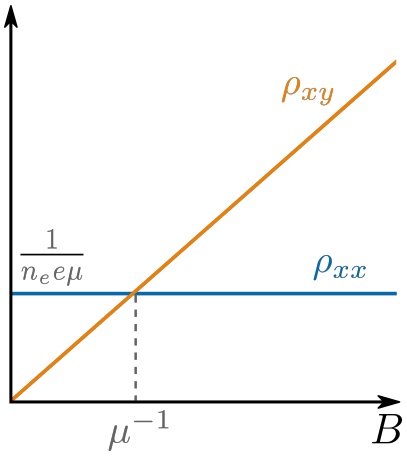

Figure 3.2 Components of the magnetoresistivity tensor for the Drude theory. The slope of xy-component is the Hall coefficient $R_H = (n_e e)^{-1}$

As the simulations and experiments are done with different units, it is advantageous to work with reduced units to be able to compare the results. In the simulations, the Fermi velocity $v_F \equiv v_0$, the effective electron mass $m^* \equiv m_0$, the elementary charge $e \equiv e_0$, and Planck's constant h have been set to unity. Furthermore, the characteristic length scale of the obstacles l_0 (radius or the length of the edges) defines the basis unit of length in the simulations. From this set of basic units v_0, m_0, e_0, l_0 and h we can derive all the other relevant units as given in table 3.1. To compare the results in reduced units one can plot for example D_{ij}/D_0 against B/B_0 by computing the corresponding D_0

time:	$T_0 = \dfrac{l_0}{v_0}$
magnetic field:	$B_0 = \dfrac{m_0}{e_0 T_0}$
diffusivity:	$D_0 = v_0 l_0$
conductivity:	$\sigma_0 = \dfrac{n_e e_0^2 l_0}{m_0 v_0}$
resistivity:	$\rho_0 = \dfrac{1}{\sigma_0}$

Table 3.1 Units derived from v_0, m_0, e_0, l_0, and h

and B_0 from the units of the experiments and the simulation.

One of the shortcomings of the Drude theory of electrical conduction is that electrons do not behave classically. Their velocity distribution is not governed by the classical Maxwell-Boltzmann distribution but by the Fermi-Dirac distribution [68]. The electrons should be treated as a Fermi gas. The details of the quantum mechanical aspects of the Lorentz gas are beyond the scope of this thesis. We shall note that the Drude model does not take into account the exact microscopic interactions between the electrons (or tracer particles) with the atomic cores (or obstacles). It is a theory on a coarse-grained scale, that replaces the interactions with the medium in which the particles move, by a friction force. In the Lorentz-Boltzmann model that we present in the next section, the collisions between the tracer particles and the obstacles are explicitly taken into account.

3.2 Lorentz-Boltzmann Model

In the following, we outline the derivation of the Boltzmann equation in the Grad limit for the two-dimensional Lorentz gas. The starting point is the description of the system in the phase space. The phase space of a two-dimensional Lorentz gas with N particles has $4N$ dimensions and is spanned by the $2N$ dimensional position and momentum vectors $\mathbf{r}^N = \{x_1, y_1, x_2, y_2, \cdots, x_N, y_N\}$ and $\mathbf{p}^N = \{p_{x_1}, p_{y_1}, p_{x_2}, p_{y_2}, \cdots, p_{x_N}, p_{y_N}\}$, respectively. The system can be described by the phase space probability distribution function $\mathbf{f}^N(\mathbf{r}^N, \mathbf{p}^N; t)$, which gives the probability to find the system at a certain point in the phase space. The time evolution of the this probability function is governed by the Liouville equation [69]

$$\frac{\mathrm{d}f^N}{\mathrm{d}t} = \frac{\partial f^N}{\partial t} + \sum_{i=1}^{N} \left(\frac{\partial f^N}{\partial \mathbf{r}_i} \cdot \dot{\mathbf{r}}_i + \frac{\partial f^N}{\partial \mathbf{p}_i} \cdot \dot{\mathbf{p}}_i \right) = 0, \tag{3.23}$$

where $\mathbf{r}_i$ and $\mathbf{p}_i$ are the position and momentum vectors of particle i respectively, and $\mathcal{H}$ the yet to be specified Hamiltonian of the system. Recalling Hamilton's equations of motion

$$\dot{\mathbf{r}}_i = \frac{\partial \mathcal{H}}{\partial \dot{\mathbf{p}}_i}, \quad \dot{\mathbf{p}}_i = -\frac{\partial \mathcal{H}}{\partial \dot{\mathbf{r}}_i}, \tag{3.24}$$

and the Poisson bracket, defined by

$$\{A, B\} = \sum_{i=1}^{N} \left(\frac{\partial A}{\partial \mathbf{r}_i} \cdot \frac{\partial B}{\partial \mathbf{p}_i} + \frac{\partial A}{\partial \mathbf{p}_i} \cdot \frac{\partial B}{\partial \mathbf{r}_i} \right), \tag{3.25}$$

we get the well-known form [69]

$$\frac{\mathrm{d}f^N}{\mathrm{d}t} = \frac{\partial f^N}{\partial t} + \left\{\mathcal{H}, f^N\right\} = 0. \tag{3.26}$$

As we assume that the tracer particles do no interact with each other, their distribution functions must be independent. Therefore, the N-particle distribution function of all particles can be written as a product of identical one-particle distribution functions

$$\mathbf{f}^N(\mathbf{r}^N, \mathbf{p}^N; t) = \prod_{i=1}^{N} f(\mathbf{r}_i,\, \mathbf{p}_i;\, t). \tag{3.27}$$

In an homogenous external field $\mathcal{F}$ the second Hamilton equation for one particle is of the form

$$\dot{\mathbf{p}}_i = \mathcal{F}_i \tag{3.28}$$

and equation (3.23) reduces to

$$\left(\frac{\partial}{\partial t} + \mathbf{v}_i \Delta_r + \frac{\partial}{\partial \mathbf{p}_i} \cdot \mathcal{F}_i\right) f(\mathbf{r}_i,\, \mathbf{p}_i;\, t) = 0. \tag{3.29}$$

Equation (3.29) is called the collisionless Boltzmann equation. We can drop the index i as all particles are considered to be identical.

Up until now, we have considered only the tracer particles of the Lorentz gas. The collisions with the obstacles should now be taken into account. Due to the collisions, the right-hand side of equation (3.29) is no longer zero and one introduces formally a so-called collision term on the right-hand side,

$$\left(\frac{\partial}{\partial t} + \mathbf{v}\Delta_r + \frac{\partial}{\partial \mathbf{p}_i} \cdot \mathcal{F}\right) f(\mathbf{r},\, \mathbf{p};\, t) = \left(\frac{\partial f(\mathbf{r},\, \mathbf{p};\, t)}{\partial t}\right)_{coll}. \tag{3.30}$$

The collision term is non-trivial as it captures the geometry of the obstacles, and also in general needs to account for multiple collisions of the tracer particle with different or identical obstacles. It is therefore impossible to write down this term without any further assumptions.

One possibility to derive a collision term for the Boltzmann equation of the Lorentz gas at low density with circular obstacles of radius r_{obs} is based on the following assumptions [40, 70]:

1. A tracer particle hits the same obstacles only once.

2. Successive collisions are uncorrelated.

3. The size of the obstacles are negligible and the obstacles are circular.

This leads to the notion of mean free path. For small densities $\rho = Nr_{obs}^2/V = nr_{obs}^2$ with $n = N/V$ being the number density, a tracer particle sees a collision after having travelled an average distance $\lambda = (2nr_{obs})^{-1}$. One now takes the Grad limit: in two dimensions it consist of taking the limit $r_{obs} \to 0$ and $N \to \infty$ while keeping the product Nr_{obs} constant [41, 47]. As a consequence, the mean free path λ is kept constant. It is the length scale that characterises the collision process. One sees also that the density $\rho \propto Nr_{obs}^2$ vanishes in that limit. Therefore, the Grad limit is a low-density limit. One can intuitively see that the Grad limit enforces assumptions one and two. If the radius of the obstacles vanishes then the probability to scatter on a previously encountered obstacle by a random collision sequence also vanishes. Now one can make the "Stosszahlansatz" for the collision integral [70]:

$$\left(\frac{\partial f(\mathbf{r},\, \mathbf{p};\, t)}{\partial t}\right)_{coll} = \int \mathrm{d}\mathbf{p}' \left(\mathcal{K}(\mathbf{p}'|\mathbf{p}) f(\mathbf{r},\, \mathbf{p}';\, t) - \mathcal{K}(\mathbf{p}|\mathbf{p}') f(\mathbf{r},\, \mathbf{p};\, t)\right). \quad (3.31)$$

This term can be derived formally in the framework of the BBGKY hierarchy (see for example [71]). But this would be beyond the scope of this thesis as it is not relevant for the further considerations. The term $\mathcal{K}(\mathbf{p}|\mathbf{p}')\ f(\mathbf{r},\, \mathbf{p};\, t)$ represents the loss term, i.e. the probability flux per time unit of particles with momentum $\mathbf{p}$ being scattered and resulting in a momentum of $\mathbf{p}'$ after the collision. The distribution $f(\mathbf{r},\, \mathbf{p};\, t)$ representing the a priori probability of finding a particle at position $(\mathbf{r},\, \mathbf{p})$ in phase space at time t and $\mathcal{K}(\mathbf{p}|\mathbf{p}')$ the transition probability from $\mathbf{p}$ to $\mathbf{p}'$. Conversely the term $\mathcal{K}(\mathbf{p}'|\mathbf{p}) f(\mathbf{r},\, \mathbf{p}';\, t)$ represents the gain term, i.e. the amount of particles being scattered from $\mathbf{p}'$ to $\mathbf{p}$. One gets already the intuition that the quantities $\mathcal{K}(\mathbf{p}|\mathbf{p}')$ and $\mathcal{K}(\mathbf{p}|\mathbf{p}')$ must be related to the differential scattering cross-sections of the obstacles.

Due to the conservation of momentum and kinetic energy during the collision process, the magnitude of the velocity vectors do no change, only the direction of the velocity vector is affected by the collisions. We set the the masses and velocities of all particles to unity. The one-particle distribution function $f(\mathbf{r},\, \mathbf{p};\, t)$ can be written as $f(\mathbf{r},\, \phi;\, t)$, where $\phi = \angle(\mathbf{v}, \hat{\mathbf{x}})$ is the angle between velocity vector of the particle and the x-axis. We also set the external field to zero and assume spatial homogeneity leading to a distribution function independent of position. Gallavotti [40] has proven that in the case of the low-density Grad limit for Poisson distributed scatterers, equation (3.31) is exact in the sense that it is not an approximation and reflects the exact dynamics of the model in that limit in the absence of a magnetic field. The equation takes the form [48]

$$\left(\frac{\partial}{\partial t} + \omega\Delta_\phi\right) f(\phi;\, t) = \nu \int_{-\pi}^{\pi} \mathrm{d}\psi\ g(\psi)\left[f(\phi - \psi;\, t) - f(\phi;\, t)\right]. \quad (3.32)$$

The diffusion term $\omega\Delta_\phi$ with the cyclotron frequency $\omega = eB/m_e$ captures the curvature of the trajectories in the presence of a magnetic field B. The collision frequency is given by $\nu = nv\Sigma = \tau^{-1}$, with $\Sigma = \int_{-\pi}^{\pi} \mathrm{d}\phi\sigma(\psi)$ being the total scattering cross section. The term $g(\psi)/\Sigma$ defines the dimensionless differential cross section with ϕ being the scattering angle. One notes that for circles $\Sigma = 2r$ and therefore in the low-density limit for $v = 1$, one retrieves the mean free time $\tau = (2rn)^{-1}$.

If a finite magnetic field is switched on that is perpendicular to the plane of the Lorentz gas, the trajectories becomes circular invalidating the key assumptions made by taking the Boltzmann-Grad limit (also see figure 3.3):

- Circular trajectories have a finite probability P_0 of not scattering with any obstacle even in the Grad limit. This fraction of trajectories have a scattering time $\tau = \infty$.

- With an increasing magnetic field, the trajectory will have a non-vanishing probability to scatter on the same obstacle multiple times. This is not compatible with the Stosszahlansatz.

To circumvent this problems one can build a model by making some assumptions as in reference [47, 48] that are valid in the Grad limit:

- A tracer particle either remains collisionless (cycling particle) or it collides with infinitely many different obstacles (wandering particle). This assumption is due to the fact that a particle hitting an obstacle multiple times will form a rosette trajectory with uncountably infinitely rotating petals and therefore exploring the surroundings of the obstacle (exceptions are of measure zero). It will therefore encounter another obstacle with a high probability at moderate densities and low B-fields. It shall be noted that we will discuss the notion of moderate densities in conjunction with the percolation transitions later in this chapter.

- An electron can only recollide with a given scatterer if no other scatterer has been hit in the mean time. This assumption is valid in the Grad limit as the probability to return to an obstacle encountered before tends to zero.

- After s collisions with the same obstacle the total scattering angle is $s\phi$ where ϕ is the scattering angle of the first collision.

Using the assumptions above, Bobylev *et al.* [48] derived a more general

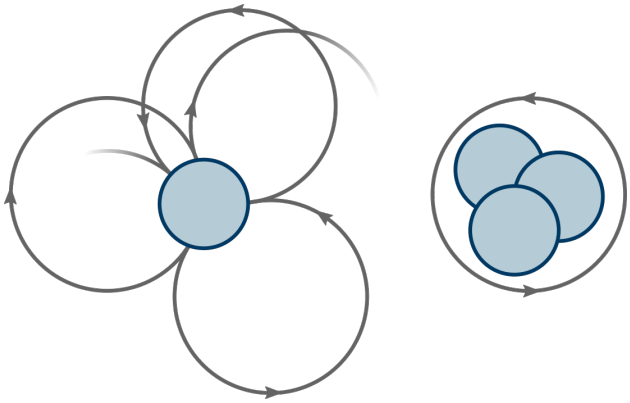

Figure 3.3 Pathological trajectories arising due to a magnetic field that acts perpendicular to the xy-plane: On the left, the tracer particle hits the same obstacle multiple times, whereas on the left no collisions occur. We call the particles with no collision "orbiting" particles.

Boltzmann equation

$$\left(\frac{\partial}{\partial t} + \omega\Delta_\phi\right) f^G(\phi;\, t) = \tag{3.33}$$

$$\sum_{s=0}^{[t/T]} P_0^s \nu \int_{-\pi}^{\pi} \mathrm{d}\psi\; g(\psi) \left[f^G(\phi - (s+1)\psi;\, t - sT) - f^G(\phi - s\psi;\, t - sT)\right]. \tag{3.34}$$

Here, $f^G(\phi; t)$ is the distribution function of the wandering particles only. The collision term can be seen a weighted summation of the collision terms arising after s recollisions with the same scatterer. Setting $s = 0$ retrieves the original equation (3.32). Here T is the cyclotron period, and $[t/T]$ is the number of periods elapsed during time t. Before the result of the equation is given, it is important to note that the one-particle distribution f^G disregards the orbiting particles. Assuming circular obstacles again, for a trajectory not to collide with any obstacle, no obstacle centre must be located between the two circles with radius $r_{tr} \pm r_{obs}$. The area of this ring is $S = 2\pi r_{tr} \cdot 2a = 2\pi r_{tr}/\lambda$. Given a two-dimensional Poisson point process with number density n, the probability of a surface of measure S to be empty is given by

$$P_0 = \exp(-n \cdot S) \implies P_0 = \exp\left(\frac{2\pi r_{tr}}{\lambda}\right). \tag{3.35}$$

The solutions of the more general Boltzmann equation (3.33) are given by

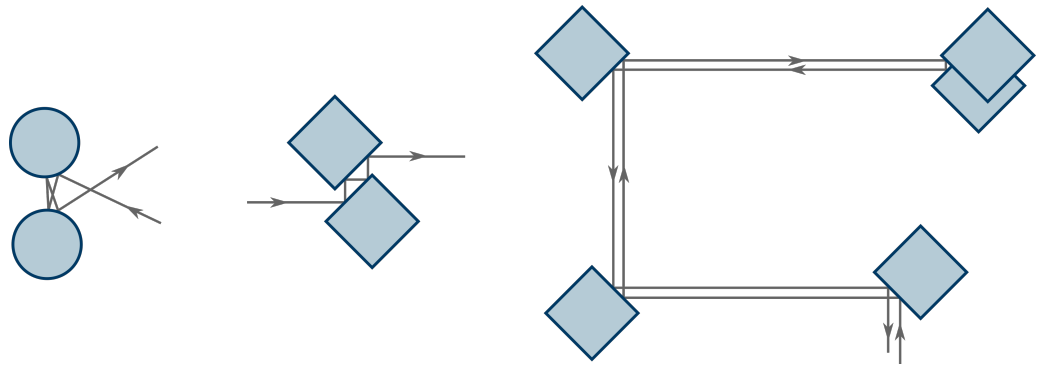

Figure 3.4 Examples of trajectories not captured in the Grad limit. The two examples on the left depict highly correlated collisions between two obstacles. More complex schemes like ring collisions with any amount of obstacles also are not taken into account in the Grad limit. The right side depicts the special case of the wind-tree model with overlapping obstacles. Here due to retroreflection, the trajectory is being folded back onto itself, therefore the same obstacles are being collided in reverse order. This memory effect does no vanish even for infinite times.

[47, 48]:

$$D_{xx} = \frac{v^2}{2}(1-x^2)\tau_D(x)\frac{1}{1+\omega_c^2\tau_D^2(x)} \tag{3.36}$$

$$D_{xy} = \frac{v^2}{2}(1-x^2)\tau_D(x)\frac{\omega_c\tau_D}{1+\omega_c^2\tau_D^2(x)} \tag{3.37}$$

where

$$\tau_D(x)^{-1} = \nu\left[1-\frac{1-x^2}{2x^2}\left(\frac{1-x^2}{2x}\log\left(\frac{1+x}{1-x}\right)-1\right)\right] \tag{3.38}$$

is the effective diffusion mean free time, and $1-x^2 = 1-P_0$ is the fraction of particles traversing the system. In the limit $B \to 0$, it follows $x \to 0$ and $\tau_D(x) \to \tau_0$, then equations (3.36) and (3.37) take the form of equations (3.18) and (3.19) derived in the Drude model.

This generalisation of the linear Boltzmann equation still only holds in the Grad limit and therefore at low densities and vanishing obstacles sizes. For finite-sized obstacles, even at moderate densities, the collisions cannot be considered to be uncorrelated any more. Also, depending on the geometry of the scatterers, the assumption made in the Grad limit that a particle will not scatter with previously encountered obstacles can not be upheld for finite-sized geometries even at very low densities (see figure 3.4). The hope is to tackle these memory effects with a kinetic theory that provides a density

expansion of the diffusion coefficient of the form

$$D = D_B + D_1 \cdot \rho + D_2 \cdot \rho^2 + ... \tag{3.39}$$

The aim of the next chapter is to provide an overview of the possibilities and limitations of such an ansatz for a simpler model, namely Ehrenfests' wind-tree model [42].

3.3 Ehrenfests' Wind-tree Model

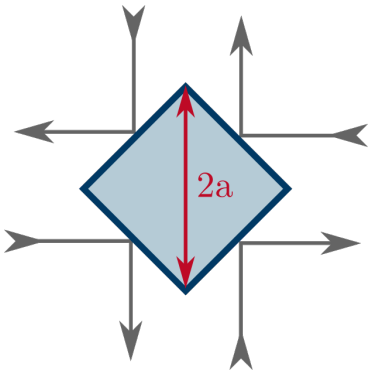

Figure 3.5 T-particle of the wind-tree model with example trajectories of the tracer particles

In the Lorentz-Boltzmann model, we have made the Stosszahlansatz. Thus, we have only considered uncorrelated collisions of one tracer particle with one obstacle. This corresponds to the binary collisions in a monoatomic gas. This assumption makes sense for very dilute gases. For gases at higher densities terms involving more than two particles start to play a role as the interaction between many particles on short timescales become more probable with increasing density. Therefore, it seems natural to attempt a correction of the transport coefficients derived in the low-density limit by taking into account particle collisions of higher order. Such a systematic expansion was first introduced by Bogoliubov [72]. Later Dorfmann and Cohen showed that such an expansion does not exist in general [73], as terms involving three particles diverge in 3 dimensions [36, 37]. For the Lorentz gas with circular obstacles in two dimensions, one can show that terms already involving 2 scatterers (second order in the density expansion) do not converge (see chapt. 5.1 in Ref. [74]). These divergences contain terms in powers of $log(\rho)$, and are due to ring collisions that are overemphasized with growing particle distances and therefore diverge in the limit $\rho \to 0$. Resummations techniques have been developed especially in conjunction with a series expansion of the inverse diffusion coefficient D^{-1} to tackle those divergences [75]. But nevertheless expansions to higher order are only possible in very simple models and are very tedious with limited success. For Ehrenfests wind-tree model (EWTM), the terms involving ring collisions with two obstacles do not diverge as in the case of circular obstacles. The divergence is suppressed because of the discreteness of the velocity space [1, 43]. An expansion of the inverse of the diffusion

coefficient has been done up to the second order in the density by Hauge and Cohen [1, 43]. We shall outline the main steps of their calculations and elucidate why a direct expansion of the diffusion coefficient is not possible. We will also show that for the case of overlapping obstacles one finds a correction of the Boltzmann diffusion term, whereas for overlapping obstacles the diffusion coefficient vanishes in the long time limit.

The EWTM [42] is a two-dimensional Lorentz gas with randomly distributed square obstacles (the trees). The diagonals of length $2a$ are rotated in such a way that one of the diagonals is parallel to the x-axis of the plane. The tracer particles (wind particles) are only allowed to move in four directions, namely up, down, right, and left. In this model one is interested in the behaviour of the self diffusion coefficient D. The staring point of the derivation is the Laplace transform of the Green-Kubo relation given by [67]

$$D = \lim_{\epsilon \to 0} \frac{1}{2} \int_0^\infty \mathrm{d}t \; e^{-\epsilon t} \left\langle \mathbf{v}(0) \cdot \mathbf{v}(t) \right\rangle . \tag{3.40}$$

where $\mathbf{v}(t)$ is the velocity of a tracer particle at time t and the average $\langle \cdot \rangle$ is taken over all possible starting positions with initial velocity $\mathbf{v}_0$ at time $t = 0$ for all possible configurations of the obstacles. The quantity ϵ has the dimension of a frequency, and in the limit $\epsilon \to 0$ one retrieves equation (2.9). In a finite volume, the MSD is bounded. Therefore, one must take the thermodynamic limit $V \to \infty$, $N \to \infty$ with $N/V = n$, before integrating over time.

The magnitude of the velocity is a conserved quantity and one can rewrite the equation above as

$$D = \lim_{\epsilon \to 0} \frac{1}{2} \int_0^\infty \mathrm{d}t \; e^{-\epsilon t} \int_0^\infty \mathrm{d}v \; \phi(t) \mathbf{v} \cdot \vec{\phi}_1(\mathbf{v}, t). \tag{3.41}$$

The average over all directions is now contained in the function $\vec{\phi}_1(t)$ that returns the average velocity of the moving tracer particle after a time t having started at $t = 0$ with the velocity $\vec{v}_0$. The function $\phi(v)$ is the probability distribution of the magnitude of the velocity. As in the EWTM all tracer particles are assumed to have the same magnitude, one sets $\phi(v) = \delta(v - v_o)$. Using the property of the delta function $\int_\Omega \delta(x - a) f(x) = f(a)$, for $a \in \Omega$ in equation (3.41) one obtains

$$D = \lim_{\epsilon \to 0} \frac{1}{2} \, \mathbf{v}_0 \int_0^\infty \mathrm{d}t \; e^{-\epsilon t} \vec{\phi}_1(t) = \lim_{\epsilon \to 0} \frac{1}{2} \, \mathbf{v}_0 \, \vec{\phi}_1^{\mathfrak{L}}(\epsilon). \tag{3.42}$$

One can absorb the integral over ϵ into $\vec{\phi}_1^{\mathfrak{L}}(\epsilon)$, which then is the Laplace transform of $\vec{\phi}_1(t)$. For $\vec{\phi}_1(t)$ to be given explicitly, we shall first look at the

Hamiltonian of one tracer particle in a given configuration of N obstacles with coordinates $\mathbf{Q}^N = \{\mathbf{Q}_1, \cdots, \mathbf{Q}_N\}$:

$$H(\mathbf{r}, \mathbf{Q}^N) = \frac{\mathbf{p}_0^{\,2}}{2m} + \sum_{k=1}^{N} V(\mathbf{r} - \mathbf{Q}_k) + \sum_{k<l} W(\mathbf{Q}_k - \mathbf{Q}_l). \tag{3.43}$$

Here $\mathbf{p}_0$ is the momentum of the tracer particle and $\mathbf{p}_0^2$ is constant. The potential part $V(\mathbf{r}-\mathbf{Q}_k)$ encodes the interaction between the tracer particles and the obstacles. It is given by

$$V(\mathbf{r}, \mathbf{Q}^N) = \begin{cases} \infty, \text{ if } \mathbf{r} \text{ lies inside of an obstacle,} \\ 0, \text{ otherwise.} \end{cases} \tag{3.44}$$

The last part $W(\mathbf{Q}_k - \mathbf{Q}_l)$ encodes the interaction between the obstacles themselves. With this term, one can enforce the two different setups of the Lorentz gas to be investigated, namely the overlapping and the non-overlapping cases. $W(\mathbf{Q}_k-\mathbf{Q}_l) = 0$ for all obstacles, describes the overlapping case. By setting

$$W(\mathbf{Q}_k, \mathbf{Q}_l) = \begin{cases} \infty, \text{ if the obstacles k and l overlap,} \\ 0, \text{ otherwise,} \end{cases} \tag{3.45}$$

one implements non-overlapping obstacles. The time evolution of the velocity is governed by the operator $\hat{O}(t) = e^{t\mathcal{L}(\mathbf{r},\mathbf{Q}^N)}$ where the Liouville operator is given by $\mathcal{L}(\mathbf{r}, Q^N) = \{H(\mathbf{r}, \mathbf{Q}^N), \cdot\}$, and $\{\cdot, \cdot\}$ are the Poisson brackets (see equation (3.25)). The canonical distribution $\rho(\mathbf{r}, \mathbf{Q}^N)$ of one moving particle and N scatterers is given by

$$\rho(\mathbf{r}, \mathbf{Q}^N) = \frac{e^{-H(\mathbf{r},\mathbf{Q}^N)}}{Z_N} \tag{3.46}$$

with

$$Z_N = \int_V \cdots \int \mathrm{d}\mathbf{r}\, \mathrm{d}\mathbf{Q}^N\, e^{-H(\mathbf{r},Q^N)}, \tag{3.47}$$

the canonical partition function. The average $\vec{\phi}_1(t)$ can now be written as

$$\vec{\phi}_1(t) = \lim_{\substack{N\to\infty, V\to\infty \\ N/V=n}} \int_V \cdots \int \mathrm{d}\mathbf{r}\, \mathrm{d}\mathbf{Q}^N\, \rho(\mathbf{r}, \mathbf{Q}^N) e^{t\mathcal{L}(\mathbf{r},\mathbf{Q}^N)} \mathbf{v}_0 \tag{3.48}$$

in the thermodynamic limit. In the Zwanzig scheme [76], this quantity is now used for the formal density expansion of D^{-1}. Using the Laplace transform

$$\int_0^\infty \mathrm{d}t\, e^{-\epsilon t} e^{t\mathcal{L}(\mathbf{r},\mathbf{Q}^N)} = [\epsilon - \mathcal{L}(\mathbf{r}, \mathbf{Q}^N)]^{-1} = G(\epsilon, \mathbf{Q}^N), \tag{3.49}$$

the equation for the diffusion coefficient (3.48) becomes

$$D = \frac{1}{2} v_0 \lim_{\epsilon \to 0} \lim_{\substack{N,V \to \infty \\ N/V = n}} \int_V \cdots \int \mathrm{d}\mathbf{r}\, \mathrm{d}\mathbf{Q}^N\, \rho(\mathbf{r}, \mathbf{Q}^N) G(\epsilon, \mathbf{Q}^N) \mathbf{v}_0. \tag{3.50}$$

Using $\frac{1}{1-x} = 1 + x + x^2 + x^3 + \cdots$, a direct expansion of $G(\epsilon, \mathbf{Q}^N)$ would have the form

$$\frac{1}{\epsilon} \left(\frac{1}{1 - \mathcal{L}(\mathbf{r}, Q^N)\epsilon^{-1}} \right) = \frac{1}{\epsilon} + \frac{1}{\epsilon^2} \mathcal{L}^2(\mathbf{r}, \mathbf{Q}^N) + \cdots \tag{3.51}$$

and therefore even in the first order with $G_0 = \epsilon^{-1}$, the integral

$$D_0 = \frac{1}{2} v_0^2 \lim_{\epsilon \to 0} \epsilon^{-1} \lim_{\substack{N,V \to \infty \\ N/V = n}} \int_V \cdots \int \mathrm{d}\mathbf{r}\, \mathrm{d}\mathbf{Q}^N\, \rho(\mathbf{r}, \mathbf{Q}^N). \tag{3.52}$$

would diverge in the limit $\epsilon \to 0$. This result is not surprising, as for a vanishing obstacle density, the diffusion coefficient grows. At zero density the motion of the particles is ballistic. Therefore, one expects a divergence of D at vanishing densities. To circumvent this problem Zwanzig [76] proposed an expansion of the reciprocal operator that leads to an expansion of the inverse diffusion coefficient. One considers the partial average

$$\vec{\phi}_1^{\mathfrak{L}}(\epsilon, t) = \lim_{\substack{N,V \to \infty \\ N/V = n}} \int_V \cdots \int \mathrm{d}\mathbf{r}\, \mathrm{d}\mathbf{Q}^N\, \rho(\mathbf{r}, \mathbf{Q}^N) G(\epsilon, \mathbf{Q}^N) \mathbf{v}_0, \tag{3.53}$$

and rewrites it as formal series

$$\vec{\phi}_1^{\mathfrak{L}}(\epsilon) = \frac{1}{\epsilon} \left[1 + \sum_{l=1} n^l B_l(\epsilon) \right] \mathbf{v}_0, \tag{3.54}$$

that is inverted to express $\mathbf{v}_0$ as a function of $\vec{\phi}_1^{\mathfrak{L}}(\epsilon)$:

$$\mathbf{v}_0 = \left[\epsilon + \sum_{l=1} n^l K_l(\epsilon) \right] \vec{\phi}_1^{\mathfrak{L}}(\epsilon, t). \tag{3.55}$$

The ϵ is absorbed in the operators K_l that can be computed from the B_l by series reversion [76]. The n^l are powers of the number density. One can set $\phi_1^{\mathfrak{L}} \mathbf{v}_0 = \mathbf{v}_0 \phi_1^{\mathfrak{L}}$, as due to the isotropy of the space one can project the average on the direction of $\mathbf{v}_0$ [36]. Equation (3.42) is then rewritten as

$$D = \lim_{\epsilon \to 0} \frac{1}{2}\, v_0^2\, \phi_1^{\mathfrak{L}}(\epsilon), \tag{3.56}$$

and its inversion reads

$$D^{-1} = \lim_{\epsilon \to 0} \frac{2}{v_0^2 \, \phi_1^{\mathfrak{L}}(\epsilon)} = \lim_{\epsilon \to 0} \frac{2v_0^2}{v_0^4 \, \phi_1^{\mathfrak{L}}(\epsilon)}. \tag{3.57}$$

One now multiplies equation (3.55) with $\vec{v_0}$ from the left to obtain an expression for v_0^2. Inserting the expression in equation (3.57) one gets

$$D^{-1} = \lim_{\epsilon \to 0} \left(\frac{2\epsilon}{v_0^2} + \frac{\vec{v}_0 \left[\sum_{l=1}^{\infty} n^l K_l(\epsilon) \right] \vec{v}_0}{v_0^4} \right). \tag{3.58}$$

Dropping the first term that vanishes in the limit $\epsilon \to 0$, and introducing the dimensionless quantity

$$\gamma(\epsilon) = a v_0^{-3} \vec{v}_0 \left[\sum_{l=1}^{\infty} n^l K_l(\epsilon) \right] \vec{v}_0, \tag{3.59}$$

Hauge and Cohen [1, 43] obtained the formal series

$$D^{-1} = 2a^{-1} v^{-1} \lim_{\epsilon \to 0} \gamma(\epsilon). \tag{3.60}$$

They derived the exact forms of the operators K_l and the contributions up to the second order in n. The first contribution is the Boltzmann term and only accounts for interactions with one obstacle and is therefore identical in the overlapping and non-overlapping case:

$$\gamma_1 = a v_0^{-3} \vec{v}_0 \, n \lim_{\epsilon \to 0} K_1(\epsilon) \vec{v}_0 = 2\rho. \tag{3.61}$$

The second term involving two obstacles is different for the overlapping and non-overlapping case:

$$\gamma_2 = a v_0^{-3} \vec{v}_0 \, n^2 \lim_{\epsilon \to 0} K_2(\epsilon) \vec{v}_0 = \begin{cases} \pi/9\rho^2 & \text{(overlapping)} \\ (\pi/9 + 4)\rho^2 & \text{(non-overlapping)} \end{cases} \tag{3.62}$$

There are collision events with more than 2 obstacles that contribute to the correction in the second order in ρ. These contributions where obtained by resummations of the binary collision expansions of the higher order operators K_l with $l < 3$. Hauge and Cohen [1, 43] classified the main contributions as:

γ_{I} corresponding to ring events of length r, where the tracer particles collide with the obstacles in the order: $1, 2, 3, \cdots, r, 1$.

Order	Name	Overlapping trees	Non-overlapping trees
$\mathcal{O}(\rho)$	γ_1	2ρ	2ρ
$\mathcal{O}(\rho^2)$	γ_2	$(\pi^2/9)\rho^2$	$(\pi^2/9+4)\rho^2$
	γ_{I}	$(4/\pi)\rho^2$	$(4/\pi - 17/24)\rho^2$
	γ_{II}	$\leq 0.1\rho^2$	$\leq 0.1\rho^2$
	γ_{III}	$\log(\infty)\rho^2$	$(91/72 - 4/3\pi)\rho^2$

Table 3.2 Overview of the correction terms to the inverse diffusion coefficient as obtained in [43]. The γ_{III} term diverges, thus, the diffusion coefficient in the overlapping EWTM vanishes for all densities.

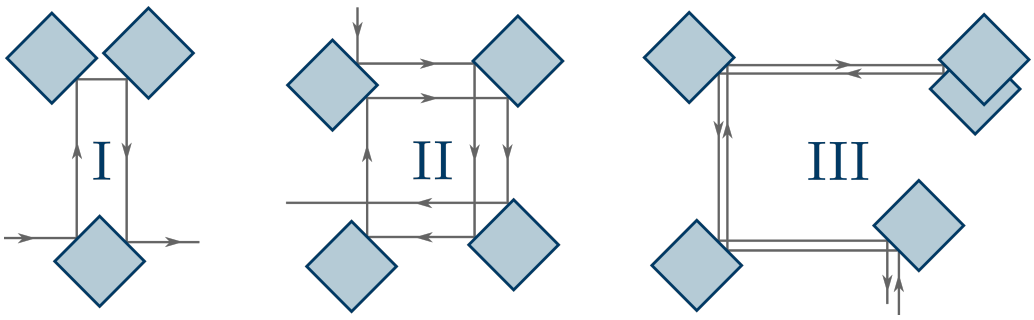

Figure 3.6 Examples of collision events: Type I ring event with $r = 3$. Type II orbiting event with $r = 4$, $p = 1$ and $k = 3$. Type III retracing event in the case of overlapping trees.

γ_{II} corresponding to orbiting events where the tracer particles collides with obstacles in the order: $(1, 2, 3, \cdots, r)^p, 1, 2, \cdots, k$. Here $k > 4$ $p \geq 1$ and $1 \leq k < r$.

γ_{III} corresponding to retracing events where after a certain number of collisions, the obstacles are traversed in reverse order.

Example trajectories of these classes are depicted in figure 3.6, and the corrections to the Boltzmann diffusion term are listed in table 3.2. One can see that in the case of the overlapping wind-tree model, the γ_{III} term diverges logarithmically. This leads to a vanishing diffusion coefficient for all densities and therefore to anomalous diffusion. Hauge and Cohen [43] predicted a subdiffusive asymptotic behaviour of the MSD of the form:

$$\Delta_r^2(t) \propto \frac{3av_0}{4\rho^2}\frac{t}{\ln(t)}. \tag{3.63}$$

Numerical simulations done by Wood and Lado [25] show a different behaviour of the MSD. They found a fractional power law for the behaviour

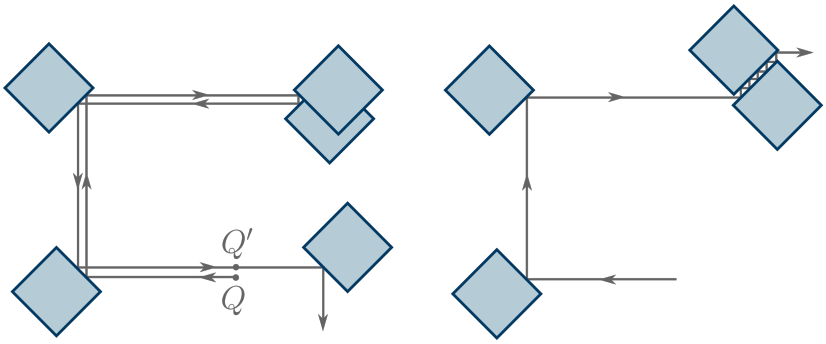

Figure 3.7 The left panel shows a retracing event of a W-particle. The distance between the original and the reflected path can become arbitrarily small. The right panel shows an "escape channel" in the case of non overlapping obstacles. These channels are the reason why retroreflection becomes improbable arbitrarily close to the incoming path.

of the MSD which is a contradiction to the asymptotic behaviour derived in equation (3.63). The kinetic theory seems to predict a wrong asymptotic behaviour. Therefore, Van Beyeren and Hauge [45] tried another approach by considering the retracing events to derive the asymptotic behaviour of the MSD. Their argument is that in the case of overlapping obstacles, apart from uncorrelated collisions the only events to consider are the retracing events. In the case of overlapping obstacles, the tracer particles can be retroreflected arbitrarily close to their original path. This is not possible in the case of non-overlapping obstacles, as there are small escape channels between the obstacles suppressing narrow retroreflection. In figure 3.7, we see that a particle starting at point Q that is retroreflected, will have its contribution to $D(t)$ cancelled as it returned to Q'. By trespassing the point Q' it will on average have a "negative" contribution to $D(t)$. Van Beyeren and Hauge derived the behaviour of the MSD as [45]

$$\Delta_r^2(t) \propto 4t_0 D_B \left(\frac{t}{t_0}\right)^{\left(1-\frac{4\rho}{3}\right)} \tag{3.64}$$

in the limit $\rho \to 0$. It will be shown in the result section, that this behaviour is surprisingly robust even at higher densities.

We have seen that the difference between overlapping and non-overlapping obstacles is tremendous in the case of the EWTM. For non-overlapping obstacles, the diffusion is still normal with corrections to the Boltzmann diffusion term that have been derived in the low-density limit. In the overlapping case, the diffusion coefficient vanishes in the long time limit and we are faced with anomalous diffusion and a density dependent exponent of the MSD. In

chapter 5 we will present the results of extensive numerical simulations of this system along with an ansatz for the van Hove correlation function in the overlapping case.

All the results of the previous sections are in the low-density limit. For increasing obstacle density, the free surface on which the tracer particle can move across the system gets smaller and smaller. Above a certain obstacle density ρ_c the obstacles can no more traverse the system and are trapped in cages formed by the obstacles. At the density ρ_c, the system undergoes a so-called geometric phase transition where a percolating infinite cluster of obstacles appears. This is a critical phenomenon that also induces anomalous diffusion at the percolation threshold. In the next section, we shall give a brief overview of the main results of percolation theory for the Lorentz gas.

3.4 Percolation in the Lorentz Gas

The percolation transition of the obstacles in the Lorentz gas is an example of a continuum percolation transition as the obstacles can be located anywhere on the two-dimensional plane. It is instructive however to first consider the more special case of lattice bond percolation as depicted in figure 3.8. In this simpler case one considers a square lattice of $N \times N$ sites. All the sites of the cluster have the same probability p to be occupied. If two adjacent sites are occupied, an imaginary walker could freely move between them. Multiple connected sites between which the walker can move are called clusters. If the walker can move from one side of the system to the opposite side, then there exists a percolating cluster. One is now interested in the probability $R_N(p)$ that a percolating cluster forms on a $N \times N$ lattice with an occupation probability p. It is intuitively clear that $R_N(p)$ is a monotonically increasing function from zero to one as with increasing p, the sites of the lattice become more and more connected. On an infinite lattice, $R_N(p)$ becomes a step function $R_\infty(p)$ that jumps from zero to one at a well defined probability p_c called the percolation threshold. Below p_c no percolation cluster exists while above p_c the probability of a percolating cluster with an infinite number of sites is unity. Therefore, the cluster size diverges at p_c. If one defines the relative distance to the percolation threshold

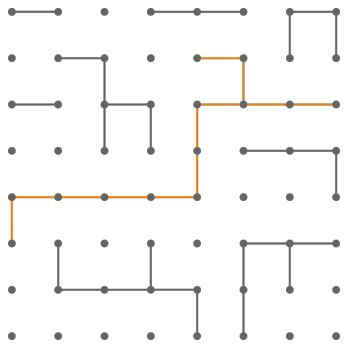

Figure 3.8 example of bond percolation on a 8×8 lattice. The orange cluster percolates through the lattice.

as

$$\epsilon = \left| \frac{p - p_c}{p_c} \right|, \tag{3.65}$$

then one finds that many quantities beside the cluster size vary as $\epsilon^{-\zeta}$. One of the main result of percolation theory is that these exponents ζ are universal. This means that the exponent only depends on the dimensionality of the system and not on the structural details of the system as shape of the obstacles, or the nature of the percolation (lattice percolation, bond percolation or continuum percolation). In the following, an overview of the main universal exponents in two dimensions is given as derived in reference [77] .

The cluster number $n_s(p)$ is defined as the number of clusters of size s per occupied lattice site [77]. At the percolation threshold it decays exponentially with the cluster size as

$$n_s(p_c) \propto s^{-\tau} \tag{3.66}$$

for $s \to \infty$, where τ is called the Fisher exponent [77]. The mean cluster size S is defined as the expectation value of the number of sites in an arbitrary cluster. It is given by

$$S = \frac{\sum_{s=1}^{s<\infty} n_s s^2}{\sum_{s=1}^{s<\infty} n_s s}, \tag{3.67}$$

and its behaviour in the vicinity of the percolation threshold is

$$S \propto |p - p_c|^{-\gamma}. \tag{3.68}$$

The mean cluster size diverges at the percolation threshold as an infinite cluster appears.

The strength of the infinite cluster P gives the probability of an arbitrary site to be part of the percolation cluster and is defined by

$$P = p - \sum_s n_s s. \tag{3.69}$$

Below the percolation threshold P vanishes, as there is no percolation cluster. Above p_c more and more sites are connected to the percolating cluster and close to the percolation threshold P scales as

$$P \propto |p - p_c|^{\beta}, \tag{3.70}$$

with $p > p_c$. If one defines l^2, as the average squared distance of two sites belonging to the same cluster [77], then above the percolation threshold the quantity diverges as

$$l^2 \propto |p - p_c|^{\beta - 2\nu}, \tag{3.71}$$

whereas the biggest cluster radius ξ diverges as

$$\xi \propto |p - p_c|^{-\nu} . \tag{3.72}$$

by approaching p_c from below. ξ is called the correlation length. All the quantities above can also be defined in the continuum case and due to the universality of the above mentioned exponents they are identical to the values of lattice percolation.

At the percolation threshold the structure of the percolating cluster is that of a fractal. To be more precise, one can look at the scaling behaviour of the total area covered by randomly distributed squares, where each square has an area A. If n is the number density and L is the side length of the area where the squares are placed, then, the total covered fraction is given by $\psi = 1 - e^{-nA}$ and the total area covered is given by $S(L) = L^2 \cdot \phi$. In two dimensions the surface $S(L)$ scales with L according to

$$S(\alpha L) = \alpha^2 S(L). \tag{3.73}$$

This behaviour is still valid in higher dimensions if one considers a d-dimensional volume instead of the surface, one has generally

$$S(\alpha L) = \alpha^d S(L), \tag{3.74}$$

with $d \in \mathbb{N}$ being the spatial dimension of the system. If the surface has fractal structure then d is no longer an integer. Especially in the two-dimensional case for the percolation cluster we have $d = d_f = 91/48$. The structure of equation (3.74) exhibits the self similarity of the percolation cluster. It shows that if one rescales the spacial dimension by a factor of α then it is sufficient to rescale $S(L)$ by a factor of α^{d_f} and therefore the system on large length scales is just a rescaled version of the system at small length scales. Such systems show the same behaviour over all length scales. For continuum percolation in the Lorentz gas the equivalent of occupancy probability p is the dimensionless quantity $\rho = n \times A$, where A is the surface of the two-dimensional T-particle. An overview of all the critical exponents mentioned above is given in table 3.3.

The self-similarity and scaling behaviour of the percolating cluster has a tremendous effect on the transport coefficients of the tracer particles moving on the free surface. In the case of the Lorentz gas, the diffusion becomes anomalous and exhibits universal behaviour in the vicinity of ρ_c and is governed by a set of so-called dynamical universal exponents. For times much greater than the mean collision time τ, the MSD is no longer proportional to the time as in the case of normal diffusion, and one has

$$\Delta_r^2(t) \propto t^{2/d_w}. \tag{3.75}$$

Exp.	Exact	Approx.
τ	187/91	2.05
γ	43/18	2.39
β	5/36	0.0139
ν	4/3	1.33
d_f	91/48	1.89

Table 3.3 Critical exponents as given in [77]

The value d_w is called the walk dimension, and takes the value of 2.878(1) [78] in two dimensions. If one considers the tracer particles moving on all clusters and not solely on the percolating cluster, then on all finite clusters, the MSD converges to a constant in the limit of infinite times. This reduces the critical exponent of the MSD, and in equation (3.75) the walk dimension d_w is replaced by [79]:

$$z = \frac{d_w}{1 - \frac{1}{2}(d - d_f)}. \tag{3.76}$$

As one approaches the percolation transition from below, the diffusion coefficient must vanish. This behaviour is also governed by a universal conduction exponent μ that is related to the walk dimension and the fractal dimension via the relation

$$\mu = \nu(d_w - 2 + d - d_f). \tag{3.77}$$

Here, the exponent also changes to $\mu_\infty = (\nu(d_w - 2))$ if one restricts the tracer particles to the incipient percolating cluster. In numerical simulations, one can therefore infer the universality class of the system by extracting the exponents from the MSD and the diffusion coefficient near the percolation threshold. Another aim of this work was to derive the percolation thresholds for different geometries. One makes use of a result from conformal field theory [80] that predicts the probability $R_L(\rho_c)$ to find a percolating cluster on an lattice of size L at the percolation transition. The probability $R_L(\rho_c)$ is independent of the shape of the obstacles and can be computed exactly in the limit $L \to \infty$ [80, 81]. With periodic boundary conditions one considerers the formation of wrapping clusters in the x- and y-directions (see figure 3.9). The probability R^e_∞ is defined as the probability of having any kind of wrapping clusters, whereas R^b_∞ gives the probability to have a cluster that wraps in both directions. These probabilities are known exactly [55, 80]:

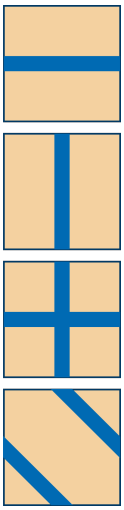

Figure 3.9 Wrapping clusters types from top to bottom: x-axis, y-axis. The last type is only possible with periodic boundary conditions.

$$R^e_\infty = 0.690473724570168677230\ldots$$
$$R^b_\infty = 0.351642853927474898465\ldots$$

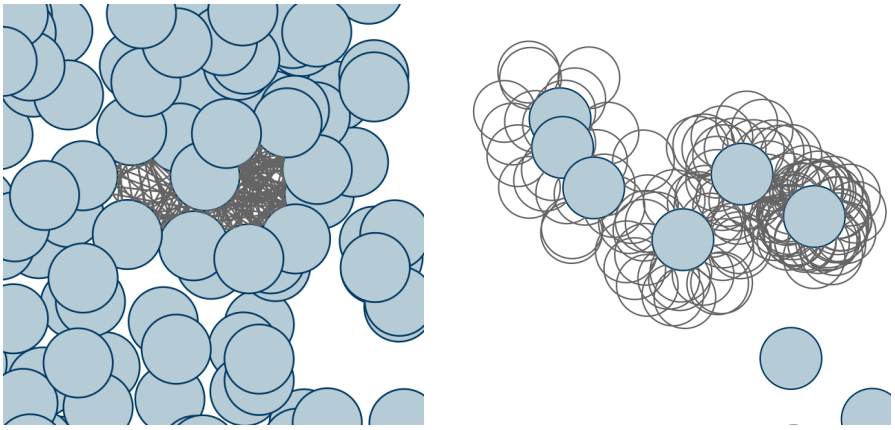

Figure 3.10 On the left panel a localised particles at high densities versus a localised particle in the low-density limit on the right panel.

Therefore, one can define an η_L^e and η_L^b by reading off the abscissa of the probability distributions $R_L^e(\rho)$ and $R_L^b(\rho)$ at the ordinates R_∞^e and R_∞^b, receptively. It has been shown [81] that the finite size scaling obeys

$$\eta_L - \eta_c \sim L^{-11/4} \tag{3.78}$$

for the rate of convergence. Therefore, by plotting η_L against $L^{-11/4}$, one obtains a straight line that can be extrapolated to zero in order to obtain an estimation of $\eta_c^e = \eta_c^b = \eta_c$.

In the presence of a magnetic field, a second percolation transition arises at the low density ρ_c^B. This is due to the fact that for sufficiently large B-fields, the cyclotron radius of the tracer particle becomes so small that the particles can no longer traverse the system as it cannot jump from obstacle cluster to obstacle cluster. Therefore, in contrast to the high density percolation transition where the tracer particles become trapped in cages formed by the obstacles, the particles are trapped around cluster islands that they cannot leave (see figure 3.10). Therefore, at low densities the particles become also localized and the diffusion coefficient vanishes. While approaching the percolation threshold by increasing the density, the length scale of the clusters that can be reached diverges and also has a fractal structure at the percolation threshold. It is still an open question whether the critical exponents of both percolation transitions are identical [82].

We have devised a method to compute the percolation threshold of the magnetic-field-induced percolation transition. As shown in figure 3.11, we use an effective obstacle that is formed by a dilation (Minkowski sum) of the original obstacle by a disk of radius r_{tr}. The radius r_{tr} corresponds to the cyclotron radius of the tracer particle in the magnetic field for which the

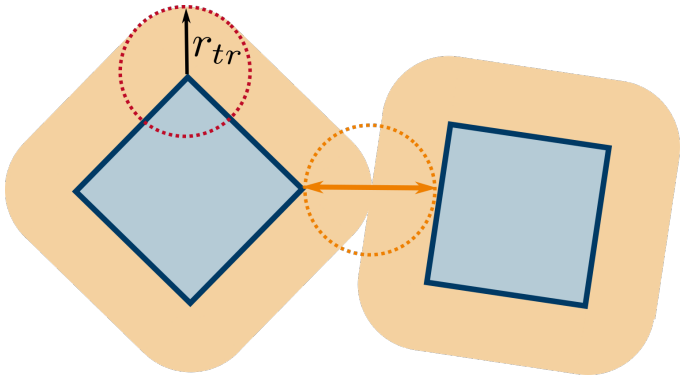

Figure 3.11 Effective T-particle (orange area) with the maximal extent of the tracer particles trajectory with cyclotron radius r_{tr}. The orange circle represents the outermost trajectory extent.

percolation transition is to be computed. If two effective obstacles overlap, this means that the distance between the surfaces of the obstacles is smaller than $2r_{tr}$ and therefore, a tracer particle can jump between the two obstacles. We compute the percolation threshold $\tilde{\rho}_c^B$ of the effective obstacles and the percolation threshold ρ_c^B is then simply given by the corresponding density of the "real" obstacles. The details for the computation of the percolation threshold for different obstacle geometries are given in the next chapter.

4 Numerical Simulations

In this chapter, the implementation of the simulation methods used in this work are explained in detail. In the first section, the methods used for the time evolution of the tracer particles will be explained. We will also give an overview of the methods implemented to find the loci of the collisions between the tracer particles and the trajectories. Then, in the following sections, we will tackle the numerical problems encountered and explain the novel type of neighbour lists that we have developed in order to accelerate the simulations. In the last section of this chapter, we will review the algorithm used by Mertens *et al.* [55] and the modifications we made to compute the percolation transitions in the Lorentz gas. The complete code of the simulation is provided via USB stick in addition to this thesis. An overview of the header files, and directions for compilation and configuration are given in the file `README.TXT`. Minimal working scripts are provided.

4.1 Event Driven Simulations

In the simulation approach called incremental time progression, the time evolution of the system is broken into small time slices S_i separated by some time step δ_t. Starting at the initial configuration S_0, the system state is updated every time step bringing it from the state S_i to the state S_{i+1}. For hard core potentials, where the particles do not feel any interaction with the obstacles upon collision, this method is not suitable. This is the case in the Lorentz gas where the obstacles are formed by line segments or curves. The collisions are instantaneous and they will mostly lie in between the time slices. This will result in a computational overhead as we need the exact position and time of the collisions. Secondly, the trajectory of the tracer particle between two collisions is so simple (a line or a circular arc), that

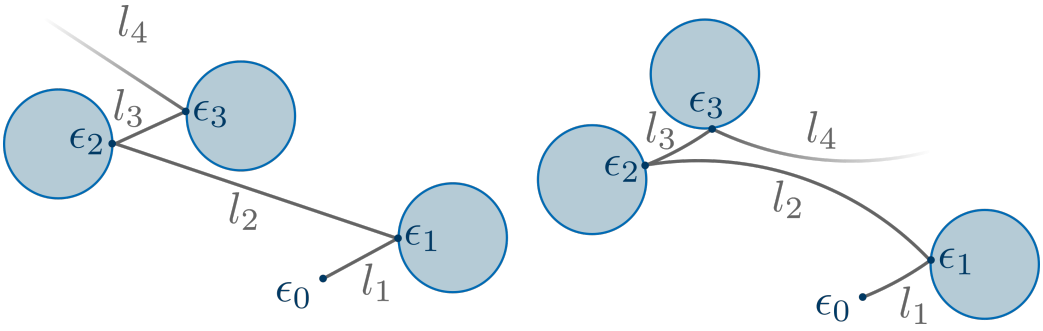

Figure 4.1 Examples of successive collision events ϵ_i for straight and circular trajectories. The length of the trajectory segment l_i is given by the travelled distance of the tracer particle between the two collisions events ϵ_{i-1} and ϵ_i. The starting position of the tracer particle can be considered as event ϵ_0.

it does not need any further computation. Therefore, it is computationally more efficient to hop from collision event to collision event instead of hopping from time slice to time slice. This approach is called event-driven simulation and the details of its implementation in the case of the Lorentz gas will be given in the following sections of this chapter.

4.1.1 The Tracer Trajectories

The trajectory of the tracer particle can be seen as a succession of collision events $\epsilon_0, \epsilon_1, ...$ of the tracer particle with the obstacles (see figure 4.1). Between each collision the trajectory is either a line segment, or in presence of a magnetic field, a circular arc. The total length l of the trajectory measured from its starting position is related to the time via $l_{tr} = v_{tr} \cdot t$, where t is the time elapsed from the start at the initial position of the tracer particle. Without loss of generality, as v_{tr} is constant, we can set the velocity v_{tr} of the tracer particle to one. We can then relate the time directly to the length of the trajectory. The total time elapsed from the initial position until the last collision event ϵ_f is therefore given by the sum of the length of all paths in between the collisions

$$t_f = \sum_{i=1}^{f} l_i, \tag{4.1}$$

where the length l_i corresponds to the distance travelled by the tracer particle between the two events ϵ_{i-1} and ϵ_i. From this coarse set of events, we can extrapolate the entire trajectory for every time $\tilde{t}$ we want to compute. One only needs the enclosing collision events ϵ_α at position A and ϵ_β at position B, with the corresponding times $t_\alpha \leq \tilde{t} \leq t_\beta$ (see figure 4.3). Therefore, one

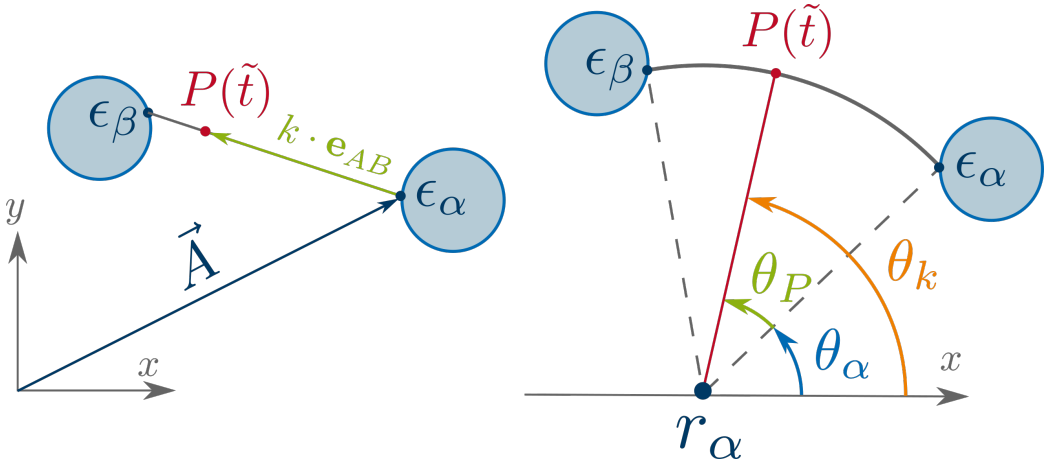

Figure 4.3 On the left: every position and velocity between two events ϵ_α and ϵ_β can be computed via $\vec{P}(\tilde{t}) = \vec{A} + k \cdot \mathbf{e}_{AB}$ if the trajectory is linear. On the right: the angle of the particle position is given by $\theta_k = (\tilde{t} - t_\alpha)/r_{tr} + \theta_\alpha$.

propagates the system to the first event ϵ_β with $t_f < \tilde{t}$.

For a linear trajectory, the position at time $\tilde{t}$ is given by

$$\vec{P}(\tilde{t}) = \vec{A} + k \cdot \mathbf{e}_{AB}, \tag{4.2}$$

with $k = \tilde{t} - t_\alpha$, where $\vec{A}$ is the vector from the origin of the coordinate system to the the collision point of the event ϵ_α. The vector $\mathbf{e}_{AB}$ is the unit vector in the direction of the vector $\vec{AB}$ between the loci of the events ϵ_α and ϵ_β, as shown in figure 4.3. For a circular trajectory, the procedure is similar. As the length of a circular arc is given by the central angle of the arc times the trajectory radius r_{tr}, namely $l_i = \theta_i \cdot r_{tr}$, equation (4.1) becomes

$$t_f = r_{tr} \sum_{i=0}^{f} \theta_i. \tag{4.3}$$

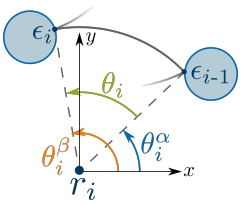

Figure 4.2 The central angle θ_i is given by the difference $\theta_i^\beta - \theta_i^\alpha$ those angles are stored on the fly at each timestep.

Here, the central angle θ_i of each trajectory piece is given relative to the momentary centre of the trajectory circle r_i as depicted in figure 4.2. The position is then given by

$$\vec{P}(\tilde{t}) = \vec{r}_\alpha + \begin{pmatrix} r_{tr} \cdot \cos\theta_k \\ r_{tr} \cdot \sin\theta_k \end{pmatrix}, \tag{4.4}$$

where $\theta_k = (\tilde{t} - t_\alpha)/r_{tr} + \theta_\alpha$. Here, θ_α is the angle of the beginning of the arc with centre $\vec{r}_\alpha$ on which the tracer particle is at time $\tilde{t}$ (see figure 4.3). We have arbitrarily set the trajectory to evolve counterclockwise relative to its

Algorithm 1 Generate Obstacle Distribution

Require:
- Container with N distributed non-overlapping obstacles
- Δ_{max} maximum shift distance

for (sweeps$\times N$) **do**
  Choose a random obstacle.
  Shift it by $\binom{\Delta_x}{\Delta_y}$ with $\Delta_x < \Delta_{max}$ and $\Delta_y < \Delta_{max}$.
  if (Obstacles overlap) **then**
    Accept the new configuration.
  else
    Reject the new configuration.
  end if
end for
return Fluid of non-overlapping obstacles at desired density

axis of rotation. Also, we need a normalized angle in the interval $[0, 2\pi]$ to be able to add each central angle in order to get the total propagation time. As the function `std::atan2()` of the `C++` standard library used to compute the angles returns values between $-\pi$ and π, the normalisation is done by computing

$$\theta_{norm} = \theta - \left\lfloor \frac{\theta}{2\pi} \right\rfloor \cdot 2\pi \tag{4.5}$$

to shift the values to the desired interval.

4.1.2 Obstacle Placement

Three types of obstacles are used in the simulations: circles, squares and crosses. The obstacles are placed in a container of area $A = L_x \cdot L_y$. Two different cases of obstacle distribution have been considered, namely randomly distributed overlapping and non-overlapping obstacles. In the overlapping case, the distribution of the obstacles is a homogenous Poisson point process that can be sampled by simply drawing random coordinates $\binom{x}{y}$ from a uniform distribution where $0 < x < L_x$ and $0 < y < L_y$. In the non-overlapping case two protocols where used to generate the obstacle configurations. The first protocol is called random sequential adsorption, referred to as RSA in the following. Here, random coordinates are drawn as in the overlapping case, but the coordinates are rejected if the obstacle to be inserted overlaps with any obstacle already in place. This process is limited by the jamming

transition at the maximum coverage[1] θ_j. At this transition the rejection rate converges to one, and the algorithm never terminates. The second protocol consist in performing a canonical Monte Carlo relaxation on the non-overlapping obstacles placed by RSA beforehand. The interaction potential between two obstacles i and j is given by:

$$\mathcal{U}_{ij} = \begin{cases} 0, & \text{obstacles } i \text{ and } j \text{ do not overlapp} \\ \infty, & \text{else} \end{cases} \tag{4.6}$$

With this potential the acceptance criterion becomes very simple as the move is simply rejected if the obstacles overlap after a random shift. The method is implemented as described by Algorithm 1. The maximal shift distance Δ_{max} should be chosen in such a way to obtain an acceptance rate of about 50%. For each class of obstacles a member function is implemented to decide if two obstacles overlap.

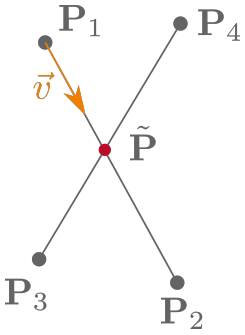

Figure 4.4 Segment $\mathbf{L}_1$ between the points $\mathbf{P_1}$ and $\mathbf{P}_2$, and segment $\mathbf{L}_2$ between $\mathbf{P_3}$ and $\mathbf{P}_4$ with intersection point $\tilde{\mathbf{P}}$

4.1.3 Collision Detection

To detect the collision events between the tracer particles and the obstacles, three types of intersections need to be considered: segment-segment, segment-circle and circle-circle intersections. In the case of a straight trajectory that intersects square obstacles, crosses or more generally any polygon, the first type of intersections is to be computed. The representation of two line segments as in figure 4.4 can be written as

$$\begin{aligned} \mathbf{L}_1 &= \mathbf{P}_1 + k(\mathbf{P}_2 - \mathbf{P}_1) \\ \mathbf{L}_2 &= \mathbf{P}_3 + l(\mathbf{P}_4 - \mathbf{P}_3), \end{aligned}$$

with $k \in [0,1]$ and $l \in [0,1]$. Setting $\mathbf{L}_1 = \mathbf{L}_2$ and solving for k leads to the solution [85]:

$$k = \frac{(y_3 - y_4)(x_1 - x_3) - (x_3 - x_4)(y_1 - y_3)}{(y_2 - y_1)(x_3 - x_4) - (x_2 - x_1)(y_3 - y_4)}. \tag{4.7}$$

As k is restricted to the unit interval, we can compare the magnitude of the numerator in equation (4.7) against the denominator as suggested in reference [85] (see Algorithm 2)

The starting point of the trajectory segment is the last collision point. The end point is set by adding k times the unit velocity vector. Therefore, the parameter k can directly be identified with the elapsed time to the next

[1] As an example $\theta_j = 0.5470735(28)$ for hard spheres [83], and $\theta_j = 0.562009(4)$ for parallel squares [84].

Algorithm 2 Test Segment Overlap

```
if denominator > 0 then
    if (numerator < 0 || numerator > denominator) then
        no intersection.
    end if
else
    if (numerator > 0 || numerator < denominator) then
        no intersection.
    end if
end if
```

collision. If many obstacles lie in the direction of the trajectory path, multiple intersections will be found. All the resulting k's are stored and the smallest k is chosen as the next collision point. We note here that due to numerical inaccuracy the situation is more involved and one also needs to store the second smallest k value as will be explained in section 4.1.4. For circular obstacles and linear trajectories, instead of algebraically solving the intersection points, it is easier to use geometric considerations to obtain the intersection points. As one can see in figure 4.5, the two intersection points $P_{1,2}$ are given by

$$\vec{P}_{1,2} = \vec{O} + \vec{h} \pm \vec{b}, \tag{4.8}$$

where $\vec{O}$ is the location of the obstacle centre. Given $\vec{v}_\perp$, the unit vector perpendicular to the trajectory rotated clockwise, the vector $\vec{h}$ is given by

$$\vec{h} = \vec{OC} \cdot \vec{v}_\perp, \tag{4.9}$$

where $\vec{OC}$ is the vector pointing from the centre of the obstacle to the starting point of the trajectory. Using the Pythagorean theorem in the triangle highlighted in figure 4.5, we get

$$\|\vec{b}\| = \sqrt{R^2 - h^2} = \sqrt{(R+h)(R-h)}. \tag{4.10}$$

By taking the scalar product between the velocity vector $\vec{v}$ of the trajectory and the vectors $\vec{CP}_{1,2}$ between the starting point of the trajectory and the intersection points, we directly get the distances $k_{1,2}$ to the next collisions

$$k_{1,2} = \vec{v} \cdot \vec{CP}_{1,2}. \tag{4.11}$$

For circular trajectories with polygonal obstacles, the algorithm is identical. The point O is then the centre of the trajectory, but instead of the length k, we store the normalized angles θ_c of the collision points. For circular

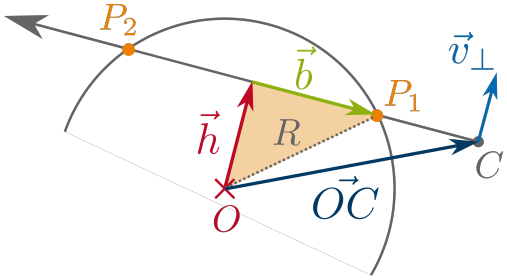

Figure 4.5 Circle-line intersection: The vector $\vec{h}$ is computed first via $\vec{h} = \vec{OC} \cdot \vec{v}_\perp$. Then, the Pythagorean theorem is applied to the highlighted triangle to calculate $\|\vec{b}\|$. The two intersection points are then retrieved according to equation (4.8).

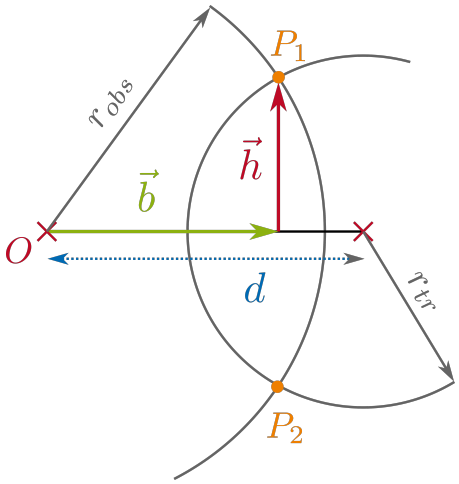

Figure 4.6 Circle-circle intersection: The vector $\vec{b}$ is computed first according to equation (4.12). Then, the Pythagorean theorem is applied to compute $\|\vec{h}\|$.

obstacles and circular trajectories as depicted in figure 4.6, the calculation is similar. The norm of $\vec{b}$ is given by

$$\|\vec{b}\| = \frac{d^2 - r_{obs}^2 + r_{tr}^2}{2d}. \tag{4.12}$$

If the distance d is greater than the distance between the obstacle midpoint and the centre of the trajectory, there will be no intersection and we can pass to the next obstacle. Furthermore, if $d < |r_{obs} - r_{tr}|$, there will be no intersection as well, and we can pass to the next obstacle saving further calculations. The vertical offset $\|\vec{h}\|$ is again computed using the Pythagorean theorem

$$\|\vec{h}\| = r_{obs}^2 - b^2. \tag{4.13}$$

Having found the intersection points, the next step is now to mirror the trajectory across the normal line to the surface at the intersection point, in order to propagate the trajectory. Here too, we have four general cases, associated with the reflection of a linear or a circular trajectory on a line or a circle. The reflections are calculated using Householder transformations. Given the unit normal vector $\hat{\mathbf{t}}$ of the reflection hyperplane, the Householder matrix is given by

$$\mathbf{H} = \mathbb{1} - 2\hat{\mathbf{t}}\hat{\mathbf{t}}^T. \tag{4.14}$$

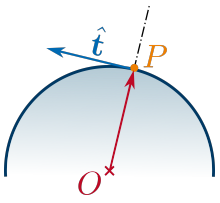

Figure 4.7 Tangent verctor at the intersction point P on a cicrcle

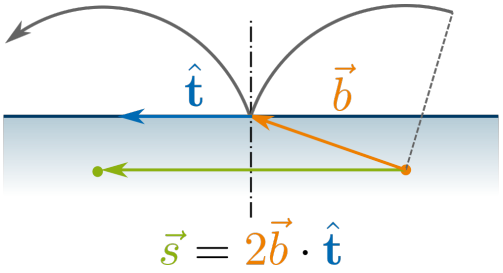

Figure 4.8 Reflection of the circular trajectory: The reflected centre of the trajectory is computed by a simple translation.

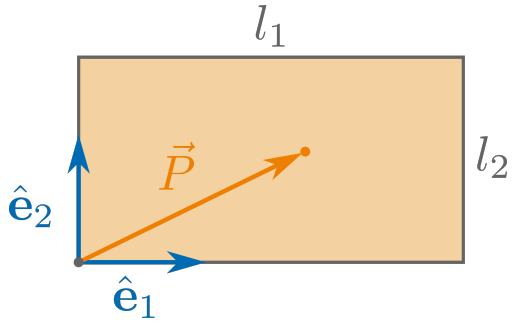

Figure 4.9 The vector $\vec{P}$ is the vector from an arbitrary corner of the rectangle to the point P. The vectors $\hat{\mathbf{e}}_1$ and $\hat{\mathbf{e}}_2$ are the unit vectors along the edges of the rectangle staring from that very same corner.

For reflections across a segment, one can directly compute the transformation matrix as the normal vectors of all the segments of an obstacle are stored in an array. For circles (see figure 4.7), the normal vector is the tangent vector at the intersection point given by

$$\hat{\mathbf{t}} = \begin{pmatrix} -\overrightarrow{OP}_y \\ \overrightarrow{OP}_x \end{pmatrix} \cdot \left\| \overrightarrow{OP} \right\|^{-1}, \tag{4.15}$$

where O is the centre of the trajectory, and P the last collision point. For circular trajectories the principle is the same. But this time the centre of the trajectory is mirrored instead of the direction vector of the trajectory. There is no need to compute the whole Householder matrix. As one can see in figure 4.8, the trajectory centre can just be translated by the vector $\vec{s} = 2\vec{b} \cdot \hat{\mathbf{t}}$, where $\vec{b}$ is the vector from the centre of the trajectory to the collision point.

So far we have considered particle-obstacle collisions, but we also need to consider obstacles-obstacle overlaps, especially for the sampling of non-overlapping obstacle distributions or the computation of the percolation threshold. We can use the same methods already described in the last paragraphs. First, the overlap of the bounding circles of two obstacles is checked. If they overlap, then all segments of both obstacles are checked against each other for intersection. If any two segments intersect, then both obstacles intersect. Furthermore, we also need to detect if a point lies in an obstacle, as at the beginning of the simulation the starting positions of the trajectories are to be set. This is done by rejection sampling: The stating coordinates $\binom{x_s}{y_s}$ are

drawn from a uniform distribution with $0 < x_s < l_x$ and $0 < y_s < l_y$. If a starting point lies inside of an obstacle it is rejected and new coordinates are drawn. To detect if a point lies in a circular obstacle is trivial. For squares or rectangles one can use the scalar product between unit vectors $(\hat{\mathbf{e}}_1, \hat{\mathbf{e}}_2)$ along the edges of the rectangle and a vector $\vec{P}$ from one vertex to the point to test (see figure 4.9). The point lies inside of the rectangle if $0 < \vec{P} \cdot \hat{\mathbf{e}}_1 < l_1$ and $0 < \vec{P} \cdot \hat{\mathbf{e}}_2 < l_2$. Crosses are considered as two overlapping rectangles and the method above is applied to each of them.

All the methods used to setup the Lorentz gas and to propagate the tracer particles have been presented. However, due to the finite precision of floating point numbers, numerical problems arise. In the next section we will explain the nature of these problems and how they were solved.

4.1.4 Numerical Problems

Floating point numbers have a finite precision. As an example, the data model on the 64 bit Unix systems used for these simulations is `LP64`. This means that the data type `int` has a size of 32 bits and the data type `double` has a size of 64 bits and a precision of 16 digits. This finite precision can lead to major problems in the computations described in the two last sections.

The first problem that arises naturally is that the intersection points computed are not exact. Therefore, they lie either slightly inside or slightly outside the obstacles. This leads to a problem if an intersection point is inside of an obstacle. While searching the collision of the trajectory with the next obstacle, an intersection point with the same obstacle will be found. This is due to the fact that the tracer particle "leaves" the obstacle thus leading to an additional intersection point very close to the last one. If one now mirrors the trajectory on this point, the trajectory propagation is erroneous and the tracer particle can become trapped inside the obstacle.

In the case of linear trajectories and convex obstacles, this problem can be solved quite easily by just ignoring the new intersection point if it lies on the same obstacles as the previous one. For circular trajectories or concave obstacles, the problem is more involved. In these cases, we use the sign of the scalar product of the velocity vector of the trajectory at the impact point with the normal vector pointing outwards of the obstacle at the impact location. As one can see in figure 4.10, an intersection will be considered as valid if the velocity vector points towards the interior of the obstacle. If the velocity vector points outside of the obstacle, then the next collision point is just an artefact due to the finite machine precision. Due to this phenomenon one needs to keep track of the closest and second closest intersection point. If the closest point is invalid one has to take the second closest point as new

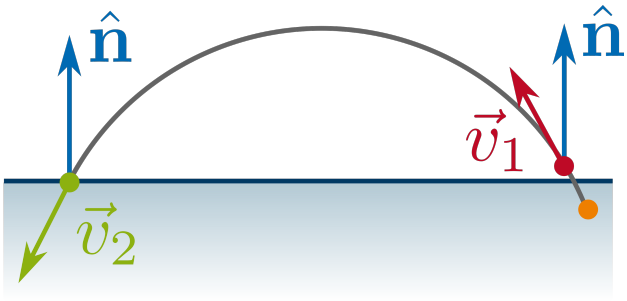

Figure 4.10 The scalar product $\hat{\mathbf{n}} \cdot \vec{v}_1$ with an erroneous intersection will always be positive in contrast to the case where the velocity vector points to the interior of the obstacles at the intersection point.

intersection point.

Other problems arise while using the Householder transformations as the computed Householder matrix (see equation 4.15) is neither exactly orthogonal nor normed. To avoid an error propagation, it is crucial to normalise the velocity vector of the trajectory after each multiplication with the transformation matrix, as it induces a tiny error in the norm at each step. This error can blow up such that the norm of the velocity vector diverges causing undefined behaviour of the whole program. Even with the norm of the velocity vector stabilized, tiny angular errors are introduced by the Householder transformation. These error are still big enough to destroy the retroreflection in the wind-tree model at long times. The only way to solve this problem is to set the orientation of the obstacles in such a way that no computations are needed for the reflections of the trajectories. For squares and crosses as obstacles, this can be done by orienting them such that all segments have an angle of 0 or $\pi/2$ with the x-axis. Consequently, one just needs to swap the signs of the velocity components according to which edge of the obstacle they collide with (figure 4.11). One could also orient the obstacles so that their edges form angles of $k \cdot \pi/4$ with the x-axis. Then one would also swap the velocity components of the trajectories as shown in figure 4.11 (right panel).

Subtraction and addition of floating point numbers are also prone to errors. Subtracting two floating point numbers with a similar magnitude will lead to the cancellation of the most significant digits [86]. This is worse in expressions like $a^2 - b^2$, as an additional rounding error is introduced due to the squaring of the numbers[1]. Therefore, all the expressions containing

[1] As an example if we considere $a = 1 + 2^{-29}$ then $a^2 = 1 + 2^{-28} + 2^{-58}$ and the last term is not captured due to the machine precision.

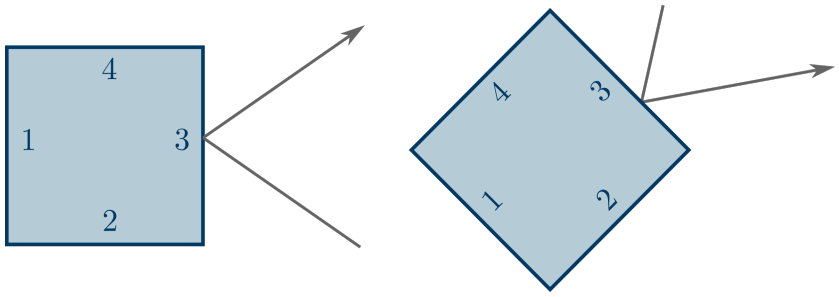

Figure 4.11 Two possible orientations of the square obstacles in order to avoid the computation of the reflection matrix. In the left case the velocity component v_x is replaced by $-v_x$ if the collision happens on the edged 1 and 3, else v_y is replaced by $-v_y$. On the right side if the tracer particles collides with sides 1 and 3 one replaces (v_x, v_y) with $(v_y, -v_x)$, and by (v_y, v_x), if the collision occurs with sides 2 and 4

terms of the form $a^2 - b^2$ are rewritten as $(a+b)(a-b)$ which minimizes the error.

One also needs to choose the random number generator with care. As stated earlier, we keep track of the closest two collision points from the last collision in order to filter out invalid intersections. If two identical oriented obstacles are overlapping and one of the x- or y-coordinates are identical, the segments of two obstacles can overlap at the intersection point. This will result in duplicated intersection points and one might get two identical erroneous intersection coordinates with the third coordinate being the valid one. This causes the simulation to get stuck as the same intersection point is computed again and again. Therefore, one must relay on the fact that this case is very unlikely. This leads us to the birthday paradox. As an example, if the underlying random number generator has a bit width of 24 bits, meaning it has 2^{24} different internal states, then drawing 5000 obstacles coordinates will lead to a probability of $p \approx 0.59$ that two or more obstacles share the same coordinate. Therefore, some obstacles might overlap, and while averaging over 10^5 different containers, at least one simulation did not terminate due to this error. In the case of parallel tasks waiting for the termination of all tasks, this is not acceptable. This problem was solved using the `C++` 64-bit Mersenne twister engine `std::mt19937_64` as the underling random number generator.

4.1.5 Periodic Boundary Conditions

One way of performing the simulation is to place the start position of the tracer particle at the centre of a huge container and abort the program once

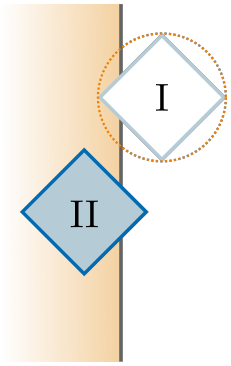

Figure 4.12 Obstacle I is the ghost obstacle of an original obstacle trespassing the right edge of the container. Obstacle II will have its ghost obstacle at position $(x_{\mathrm{II}} - L_x, y_{\mathrm{II}})$. The radius r_{obs} is represented by the orange circle.

the particle has left the container. This approach is inefficient in terms of memory consumption. The second approach that was preferred in this work is to use periodic boundary conditions. Thus, a particle leaving the container will reenter the container on the opposite side. This method is less memory consuming and more efficient, but needs a more careful implementation and is prone to finite size effects if the box size is chosen too small. With periodic boundaries, care must be taken at the edges of the simulation box. If an obstacle protrudes an edge of the simulation box, a copy of it must also be placed at the opposite side of the container. Else, a particle leaving the container can find itself trapped in an obstacle after re-entering the box because the collision with its periodic image was ignored. To detect which obstacles could cross the container boundaries, one considers the radius $r_{obs} = max\{|\vec{r}_i - \vec{r}| : \vec{r} \in \{\mathcal{O}\}\}$ defined as the distance from the coordinate position of the obstacle $r_i = (x_i, y_i)$ (in our case also its centre of mass), to the outermost point of the obstacle O_i in the set of all obstacles $\mathcal{O}$ (see figure 4.12). Any obstacle closer as r_{max} (or $2 \times r_{max}$ in case of Monte Carlo annealing) to any border must have a ghost image on the other side.

With periodic boundary conditions, the behaviour of the tracer particle for linear trajectories is straightforward. If no intersections are found inside the simulation box, the starting point of the last trajectory segment is translated by $\pm L_x$ or $\pm L_y$ according to the side that the particle is leaving the container. In the case of circular trajectories, the situation is more involved if the trajectory radius is of the same order of magnitude as the container length. Valid collisions will be detected that would only come into play in the periodic image of the container as shown in figure 4.13. Therefore, we need to discriminate between collisions before and after the trajectory has "left" the container. In previous simulations, it has been shown to be problematic if one considers the particle intersections with the container walls as real intersections and then shifts the coordinates by one box length and setting it as new starting point of the trajectory. Due to the finite precision, if an obstacle happens to be close to the edge of the container, problems like trapped particles on the boundaries or particles landing inside of obstacles on the other side of the container arise. To avoid those complications a solution is to shift only the trajectory's centre and its starting point. The intersections between the tracer particle and the container edges are only computed to detect if the trajectory can leave the container (see figure 4.13).

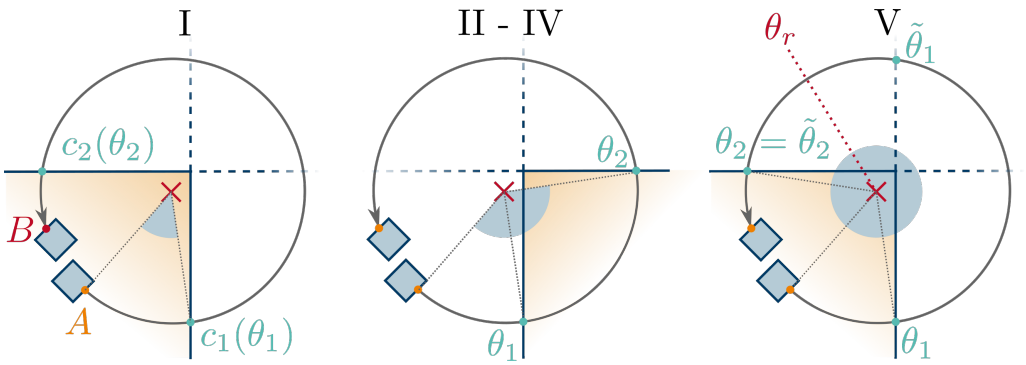

Figure 4.13 As on can see on the left in step I, after the last collision (point A) the trajectory leaves the container at point c_1, hence collision B should be disregarded for now. We keep track of the two angles of the intersections of the trajectory with the container θ_1 and θ_2 relative to the point A. The angles are reordered so that θ_1 is the smallest of the two angles. If the trajectory has not left the container, only intersections with angles smaller than θ_1 are considered (blue coloured sector). As no intersection is found the centre of the particle is moved by $-l_x$ and one gets case II. Here, as the particle has re-entered the box, one only considers intersections with $\theta < \theta_2$. If no intersections are found the same procedure is applied in the other quadrants. In case V the particle has now re-entered his original quadrant. If one still requires $\theta < \theta_2$, no intersection would be found. To differentiate between case I and V a "ratchet" angle $\theta_r = \frac{1}{2}(\tilde{\theta}_1 + \tilde{\theta}_2)$, between the two last container intersections was introduced. It is initialised as $\theta_r = 0$ in the first case and then computed in all the other cases. Now, if θ_1 is smaller than θ_r (as in case V), we set $\theta_1 = \theta_1 + 2\pi$. Reordering swaps the angles and the requirement becomes $\theta < \theta_2 \equiv \theta < \theta_1 + 2\pi$ (blue sector) and therefore intersection B is now the next valid intersection.

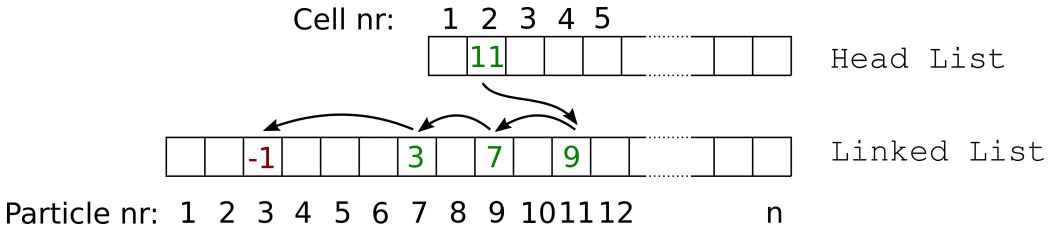

Figure 4.15 Schematic representation of the simply connected list: each list entry points to the next obstacle number in the same cell. If there is no next obstacle, the entry is -1.

4.2 Accelerating the Simulation

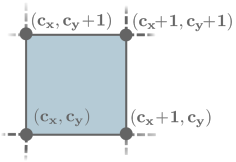

Figure 4.14 All the obstacles in the blue square are associated to the cell with coordinates (c_x, c_y). We can consider the cells as a grid of vertices $\mathbb{G}_c \in \mathbb{Z}^2$

4.2.1 Cell Lists

To accelerate numerical simulations, one can decompose the spatial domain into smaller regions, in order to pick only the relevant subdomains for the computation of particle interactions. The data structure used in many scenarios is the so-called cell list. Its purpose is to reduce the amount of obstacles to check for intersections with the tracer particle. This is done by restricting the collision search to a cell stencil whose geometry is adapted to the form of the trajectory. To this end, the simulation box is divided into smaller quadratic cells of side length l_{cell}. We will show that a good choice is $l_{cell} \geq 2\sqrt{2}r_{obs}$, where $r_{obs} = max\{|\vec{r}_i - \vec{r}| : \vec{r} \in \{\mathcal{O}\}\}$ defined as the distance from the coordinate position of the obstacle $r_i = (x_i, y_i)$ (in our case also its centre of mass), to the outermost point of the obstacle O_i in the set of all obstacles $\mathcal{O}$.

The coordinates (c_x, c_y) of the cell containing the obstacle are then $c_x = \lfloor x_i/l_{cell} \rfloor$ and $c_y = \lfloor y_i/l_{cell} \rfloor$. Therefore, the cells form a regular quadratic lattice $\mathbb{G}_c \subset \mathbb{Z}^2$ with dimensions $N_{cells} = n_x \times n_y$. Each cell has the number $n_c = c_y \cdot n_x + c_x$. Choosing the cells for the stencil is equivalent to the rasterisation of a geometric shape on the points of the lattice $\mathbb{G}_c$.

The cell list is stored as two arrays of integers, `cell_head` of length N_{cells} and `cell_list` of length $N_{obstacles}$. For the latter we used a data structure called "singly linked list": The indices i represent the number of the obstacle $i \in [0, N_{obstacles}]$, and the entries `cell_list[`i`]` contain the index of the next obstacle in the same cell. If there is no next obstacle, the entry at the index is -1 (see figure 4.15). In order to generate the cell list one proceeds according to algorithm 3.

Algorithm 3 Fill Cell List

for each cell number n_c **do**
  `cell_head`$[n_c] \leftarrow -1$
end for
for each obstacle number i **do**
  $n_c \leftarrow$ cell number of obstacle i
  `cell_list`$[i]$ $\leftarrow$ `cell_head`$[n_c]$
  `cell_head`$[n_c] \leftarrow i$
end for

4.2.2 Stencils

In order to calculate the next intersection of the trajectory with an obstacle, we only pick cells that contain obstacles in reach of the trajectory. This is done by traversing a stencil that contains only the cells relevant for the search. There are four different types of stencils that are used in the simulations depending on the presence of a magnetic field and the geometry of the obstacles.

Vertical and Horizontal Stencils

The simplest version is implemented in the wind-tree model with no magnetic field. One simply takes all the cells horizontally or vertically in the direction of the tracer particle, starting one cell behind the cell where the last intersection has occurred until the edge of the container, adding the two neighbouring rows or columns. As the stencil is filled in the direction of the trajectory, one can abort the collision search once a valid intersection has been found. Care has to be taken that a small tail of cells still needs to be checked in order to detect all possible collisions (see figure 4.16).

Linear Stencils

More generally, in the absence of a magnetic field, all directions are allowed. Therefore, the stencil is built by rasterizing a line on the lattice $\mathbb{G}$ between two points A and B. This is done by using the algorithm proposed by Bresenham [87], that we will describe now.

Without loss of generality, we only consider lines with slopes $0 \leq m \leq 1$ where $m = \Delta y/\Delta x$, with $\Delta x = B_x - A_x$ and $\Delta y = B_y - A_y$. This corresponds to the first octant if the starting point was at the origin of the coordinate system. As we can see in figure 4.17, starting at P_1, the closest point to the line with abscissa $x + 1$ will have the ordinate y as $m < 0.5$ in this case.

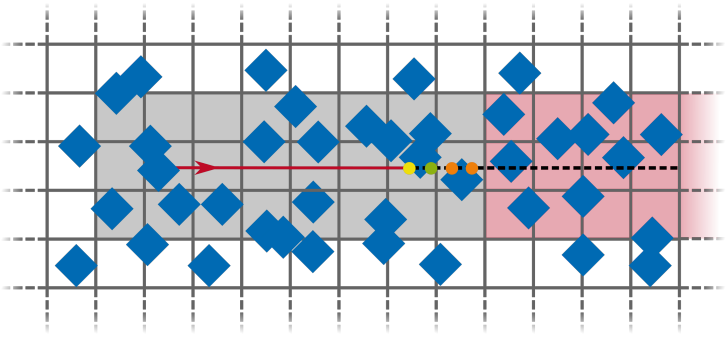

Figure 4.16 In this stencil (grey area) along the trajectory (red line) the collision detection can be aborted one column after a valid collision has been found (green dot). This saves computation time as the red area is not processed. Note that the ordering of the collisions along the trajectory is not conserved between possible collisions in the same cell or on the same obstacle. One can see that the first detected collision (green dot) has been detected before the closest collision from the trajectory's origin (yellow dot).

Algorithm 4 Error Update

$\epsilon \leftarrow m - 0.5$
if $\epsilon \leq 0$ **then**
  $\epsilon \leftarrow \epsilon + m$
else
  $\epsilon \leftarrow \epsilon - 1$
end if

Therefore, the next point in our rasterized line has the coordinates $(x+1, y)$. The error Δ_0 in the y-direction is the slope m. To choose the next point with abscissa $x+2$, one considers the quantity $\Delta_1 = \Delta_0 + m$. If $\Delta_1 < 0.5$, the next point has still ordinate y else, as in our case, it has ordinate $y+1$. Depending on this choice the error Δ_2 or more generally Δ_{i+1} is calculated differently. If we increment the ordinate, we need to account for that by subtracting one from the error. One can resume the procedure of updating the errors as shown in Algorithm 4. In order to avoid floating point operations, instead of checking the sign of $\Delta_i - 0.5$ one can rescale the whole procedure by $2\Delta_x$ as $\Delta_x \geq 0$ and one obtains the Bresenham algorithm (Algorithm 5). In order to draw lines in the other octants, only minor changes to the algorithm as swapping ordinates and abscissas are needed. A table detailing those changes is given in reference [87].

As not only the obstacles in the cells on the rasterized line can interfere with the trajectory but also the obstacles in the surrounding cells, one needs

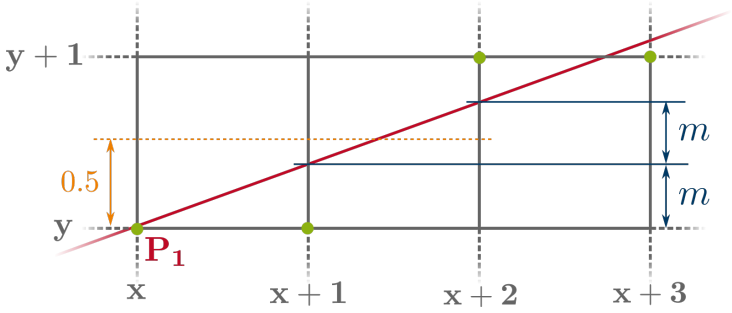

Figure 4.17 Detail of the incrementation process: Starting from the point P_1 with ordinate y, the slope m is added at each step. If the value $y + m$ is greater than $0.5 \cdot ((y + 1) - y)$, then the next point with abscissa $x + 1$ of the line has ordinate $y + 1$, else the next point has ordinate y.

to determine the thickness of the cell stencil. The biggest distance in y-direction between the trajectory and a cell coordinate is $l_{cell}/2$. This is a property of the algorithm. In the first octant, the trajectory can pass below or above the cell with coordinates (c_x, c_y) (blue cells in figure 4.18). To account for this one adds the cell with coordinates $(c_x, c_y - 1)$ and $(c_x, c_y + 1)$ to the stencil (orange cells). Now in the worst case where the trajectory has a slope $m = 1$, the closest point to the trajectory that is not in the stencil is at a distance of $\tilde{l} = \frac{l_{cell}}{2\sqrt{2}}$. Therefore, to avoid that an obstacle that is not in the stencil reaches the trajectory, one must choose $l_{cell} > 2\sqrt{2} \times r_{max}$. One also needs to keep in mind that for a given starting cell A and ending cell B every trajectory $\overline{ab}$ with $a \in A$ and $b \in B$ will be mapped into the same stencil. As one sees in figure 4.18 (red dotted lines), the worst offset in y-direction is then $1.5 \times l_{cell}$. Therefore, the stencil is extended again by two cells (hatched orange squares). This treatment can be generalized to the first quadrant by noting that for $|m| > 1$, we only need to switch the x and y-directions. Consequently, instead of adding extra cells in y-direction, the cells are added in the x-direction. For the other quadrants, one simply maps the situation to the first quadrant by interchanging the start and end points as specified in table I of reference [87].

The end point of the stencil is the cell where the trajectory and the container wall intersect. Here, two extra steps of the algorithm should be performed in order to account for the stencil cells still reaching into the container. Also, one row or column (depending on m), behind the starting point is added to the stencil. The main advantage of this procedure is that one selects the cells in the direction of the trajectory. Therefore, one has a coarse ordering of the obstacles which allows to abort the collision search before the whole stencil is processed. Once a valid intersection has been

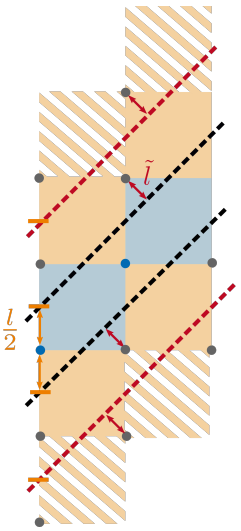

Figure 4.18 Worse case offset (red lines) between the rasterized cells (blue) and the possible trajectory. $\tilde{l}$ is the smallest distance that the center of an obstacle can come close to the trajectory without being listed in the stencil.

Algorithm 5 Bresenham algorithm first octant

Require: coordinates (A_x, A_y) and (B_x, B_y) as integers grid points.

$\Delta_x \leftarrow (B_x - A_x)$
$\Delta_y \leftarrow (B_y - A_y)$
$\epsilon \leftarrow 2\Delta_y - \Delta_x$
$X \leftarrow A_x$
$Y \leftarrow A_y$
while $(X \leq B_x)$ **do**
  if $\epsilon \leq 0$ **then**
    $Y \leftarrow Y$
    $\epsilon \leftarrow \epsilon + 2\Delta_y$
  else
    $Y = Y + 1$
    $\epsilon \leftarrow \epsilon + 2\Delta_y - 2\Delta_x$
  end if
end while

found in one cell (as shown in figure 4.16) and the neighbouring cells have been processed, the collision search can be aborted. This has a major impact on the efficiency of the programme.

4.2.3 Simple Circular Stencils

In the presence of a magnetic field, the trajectories become circular. For stronger fields where the cyclotron radius r_{tr} is much smaller than the side length of the container L, one can use a circular stencil of radius $r_s = r_{tr} + r_{obs}$ around the centre of the trajectory. The stencil has the maximum extent $s_x = s_y = 2\lceil r_s/l_{cell} \rceil + 1$ in the x- and y-directions. As periodic boundary conditions are implemented, we wrap the stencil around the resulting torus and trim the stencil if $s_x > n_x$ or $s_y > n_y$. If n_x or n_y are odd, the stencil indices simply run from $\lfloor -n_x/2 \rfloor$ to $\lfloor n_x/2 \rfloor$ (or accordingly in the y-direction). If n_x or n_y are even, then the stencil indices runs from $-n_x/2+1$ to $n_x/2$ (or accordingly in the y-direction). The stencil offsets are computed only once by checking the closest distance between a cell at the origin and each cell in the index range defined above. If a cell is in the range r_s, its offset coordinates are added to the stencil, else they are discarded. Therefore, one traverses all cells relevant to the collision search by simply adding the offsets of the stencil to the cell containing the centre of the trajectory (see Figure 4.19). Also, to calculate the shortest distance between two cells, one has to remember that one needs to take the closest points of the two cells as shown in figure 4.19.

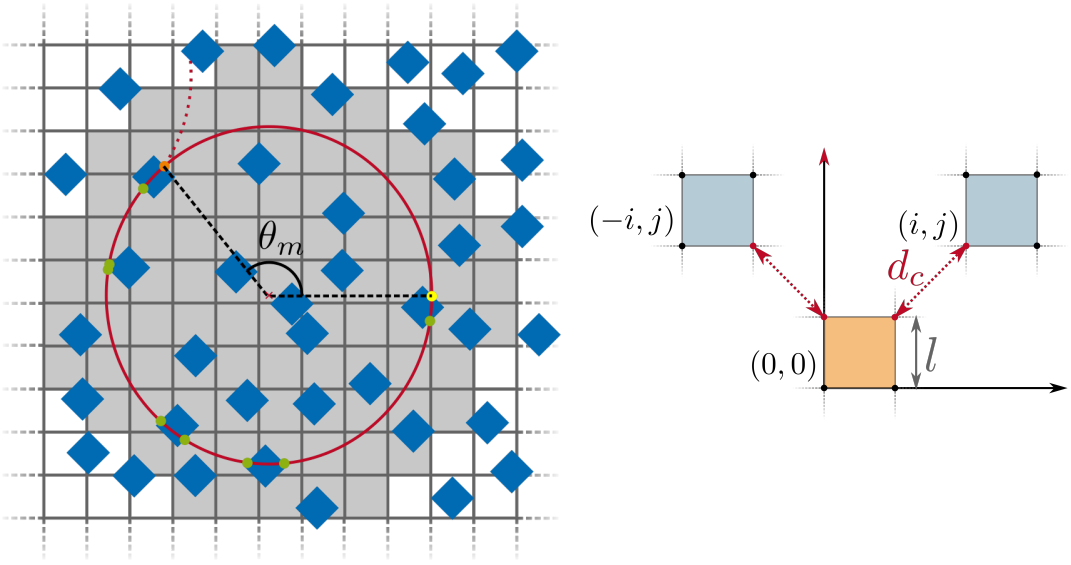

Figure 4.19 Left panel: The grey cells are the cells in the stencil. The yellow point is the starting point of the trajectory. The normalized central angle θ_m between the starting point and each collision point is computed. The point with the smallest angle is a candidate for the next collision point. Right panel: schematic of the cell distance between a cell at the origin and different cells. One chooses the points with the smallest distance between two cells as the cell distance d_c.

4.2.4 Circular Stencils

For increasing trajectory radius, just taking a circular stencil becomes inefficient as the amount of cells to consider increases proportionally to r_{tr}^2. For small B-fields all the obstacles in the simulation box have to be checked for collisions. The solution to this problem is to rasterize the cells into a circular arc that covers the trajectory. This can be done similarly to the linear case by using an incremental drawing algorithm for circular arcs [88]. This method has also the advantage that it induces an ordering of the cells in the propagation direction of the tracer particle. This allows an early abort of the collision detection. Here also, only integer multiplications, additions and subtractions are needed. We restrict ourselves to the first quadrant to outline the algorithm as explained in reference [88]. In the following upper case coordinates (X_i, Y_i) will represent integer numbers whereas lower case symbols (x_i, y_i) represent a vector in $\mathbb{R}^2$.

Starting the rasterisation in the first quadrant and proceeding clockwise, given the coordinates $P_i = (X_i, Y_i)$, there are three translations vectors to

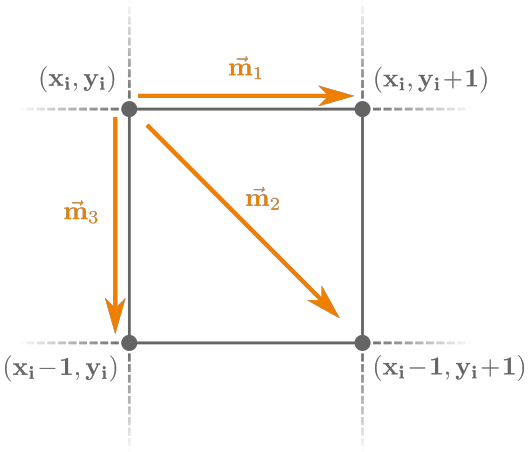

Figure 4.20 Three possible movements to the next pixel used to rasterize the circle in the first quadrant.

attain the next point of the rasterized circle:

$$\vec{m}_1 = \begin{pmatrix} X_i \\ Y_i \end{pmatrix} \rightarrow \begin{pmatrix} X_i + 1 \\ Y_i \end{pmatrix} = \begin{pmatrix} 1 \\ 0 \end{pmatrix}, \tag{4.16}$$

$$\vec{m}_2 = \begin{pmatrix} X_i \\ Y_i \end{pmatrix} \rightarrow \begin{pmatrix} X_i + 1 \\ Y_i - 1 \end{pmatrix} = \begin{pmatrix} 1 \\ -1 \end{pmatrix}, \tag{4.17}$$

$$\vec{m}_3 = \begin{pmatrix} X_i \\ Y_i \end{pmatrix} \rightarrow \begin{pmatrix} X_i \\ Y_i - 1 \end{pmatrix} = \begin{pmatrix} 0 \\ -1 \end{pmatrix}. \tag{4.18}$$

The algorithm now chooses the point with the minimum absolute difference between the squared radius R^2 of the original circle, and the squared radii of the 3 circles that have the same centres but passing through the candidate points $P_i + \vec{m}_{1,2,3}$. The sign of

$$\Delta_i = (P_i + \vec{m}_2)^2 - R^2 \tag{4.19}$$

is evaluated first. If the sign of Δ_i is negative, the point $(X_i + 1, X_i - 1)$ is inside of the original circle, and one needs to decide between the translations $\vec{m}_1$ and $\vec{m}_2$ by evaluating the sign of

$$\delta = |(P_i + \vec{m}_1)^2 - R^2| - |(P_i + \vec{m}_2)^2 - R^2| = 2\Delta_i + 2Y_i - 1. \tag{4.20}$$

If the sign of δ is positive then the point $(X_i + 1, Y_i - 1)$ is closer to the original circle and translation $\vec{m}_2$ is performed, otherwise the vector $\vec{m}_1$ is added to the coordinates of p_i to obtain the next point. If the difference Δ_i

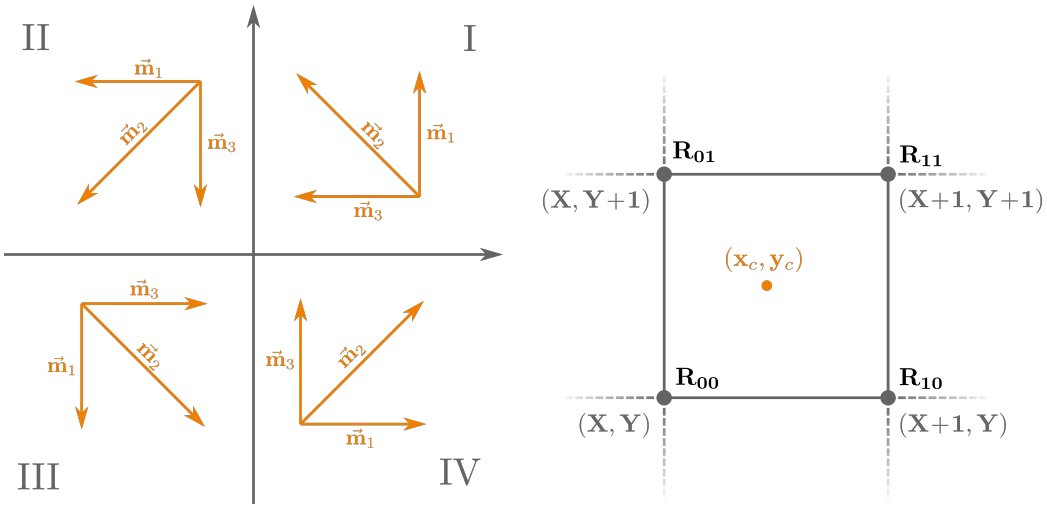

(a) Translations $\vec{m}_1, \vec{m}_2, \vec{m}_3$ corresponding to each quadrant in the counterclockwise case. At each quadrant crossing the vectors are replaced by their equivalent in the new quadrant.

(b) Residues R corresponding to the four corners of the cell with coordinates (X, Y). The point with the smallest residue is chosen as starting or ending point of the circular arc to draw.

Figure 4.21

is positive then the point $(X_i + 1, Y_i - 1)$ is outside of the circle, and the value

$$\delta = |(P_i + \vec{m}_3)^2 - R^2| - |(P_i + \vec{m}_2)^2 - R^2| = 2\Delta_i + 2X_i - 1 \tag{4.21}$$

is evaluated to decide whether $\vec{m}_2$ or $\vec{m}_3$ lead to points closer to the real circle. If δ is positive, then the vector $\vec{m}_2$ is added to coordinates of the point p_i, else the translation $\vec{m}_3$ is performed. The error term Δ_i can also be updated recursively depending on the last movement [88]:

$$\Delta_{i+1} = \begin{cases} \Delta_i + 2X_{i+1} + 1 & \text{after } \vec{m}_1, \\ \Delta_i + 2X_{i+1} - 2Y_{i+1} + 2 & \text{after } \vec{m}_2, \\ \Delta_i + 2X_{i+1} + 1 & \text{after } \vec{m}_3. \end{cases} \tag{4.22}$$

In general, to draw an arc between multiple quadrants, first the number of quadrant crossings is computed. Then, the start and end points (X_s, Y_s) and (X_t, Y_t) are mapped back to the first quadrant as per table I of reference [88] to obtain the corresponding coordinates $(\hat{X}_s, \hat{Y}_s)$ and $(\hat{X}_t, \hat{Y}_t)$, respectively. Then, at each quadrant crossing the translation vectors $\vec{m}_i$ are adjusted accordingly (see figure 4.21a). If no quadrant crossing is left, and $\hat{X}_t > \hat{X}_i$ or $\hat{Y}_t < \hat{Y}_i$, the algorithm terminates.

To use this method for the cell stencil, one first computes the starting point or cell $P_s = (X_s, Y_s)$. Given the coordinates (x_c, y_c) of the last collision, and (r_x, r_y) the coordinates of the centre of the trajectory after the last collision, one computes the initial error of each corner of the cell as in reference [89] page 211:

$$\begin{pmatrix} X \\ Y \end{pmatrix} = \begin{pmatrix} \lfloor (c_x - r_x)/l_{cell} \rfloor \\ \lfloor (c_y - r_y)/l_{cell} \rfloor \end{pmatrix}$$

and the four residuals

$$\begin{aligned} R_{00} &= X^2 + Y^2 - x^2 - y^2, \\ R_{10} &= R_{00} + 2X + 1, \\ R_{11} &= R_{01} + 2Y + 1, \\ R_{01} &= R_{11} - 2X - 1. \end{aligned}$$

The corner with the smallest error is chosen and the initial error is set. If the trajectory does not intersect the container walls, then the end point is set as the start point: $(X_t, Y_t) = P_t = P_s$. If the trajectory intersects the container, this point is taken as end point. The number of quadrant crossings is computed. As the trajectory runs counterclockwise, for the same reason as in the case of linear trajectories, one needs to start the stencil ahead of the first cell. Consequently, a few steps are performed backwards in the clockwise direction before the stencil cells are chosen. The same is done at the end of the stencil where some extra steps are appended. We ha¸ve used a thickness of 5 cells for the linear stencils. Here, there is an additional offset between the real origin of the circle of the trajectory and the rounded origin of the stencil circle. This offset has the maximal extent of $\pm l_{cell}$ in each direction. Therefore, we used a thickness of 7 cells for the circular stencils. One adds three cells to the left and to the right if $X_i > Y_i$, and 3 cells at the top and the bottom if $X_i < Y_i$. Also it is very important that no cells are added twice as we want the list of potential collision coordinates to have only unique elements without any further processing. Thus, care needs to be taken in the cases close to $X_i = Y_i$ to avoid overlapping stencil cells.

4.3 Computing the Percolation Transition

4.3.1 The Union Find Data Structure

All the methods described above used for the propagation of tracer particles can be also used with minor changes to calculate the percolation transition of

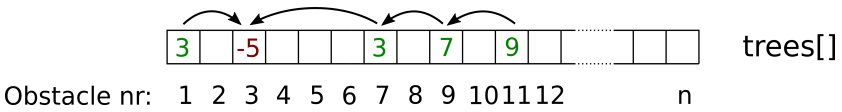

Figure 4.22 Example of a parent pointer tree structure: Obstacles 1, 3, 7, 9 and 11 form a connected cluster of size 5. The root node or representative of the cluster is obstacle number 3.

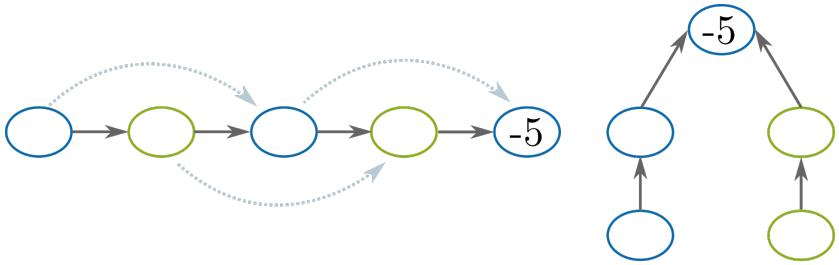

Figure 4.23 Example of path splitting: While traversing the tree, each node is connected to its grand parent leading to a shorter path to the root R.

two-dimensional obstacles following the method of Mertens and Moore [55]. In this method, the main computational task is to add obstacles in a box with periodic boundary conditions until a wrapping cluster is formed. The number of added obstacles is then stored for further computations.

To keep track of the connected components, we used a data structure called union-find data structure. It is implemented as a parent pointer tree, where each node is an obstacle and each tree represents a connected cluster of obstacles. If an obstacle is added that causes two clusters to overlap, they are merged. The root of the bigger cluster is set as parent node of the smaller cluster (see figure 4.24 for details). If the clusters have identical size, the ordering is aleatory. The trees are implemented similarly to the cell list as an integer array `trees[]` (see figure 4.22). To each obstacle we attribute a number. This number is simply the number of obstacles already inserted in the system. To get the parent node of an obstacle `i`, one looks at the value stored in `trees[i]` which is the number of the parent obstacle and also the address of its grand parent. If the number stored is negative, then there is no parent obstacle and one has reached the root node. The magnitude of the number stored at the root returns the tree size.

As the tree sizes grow, traversing trees in order to find the roots becomes expensive as the number of nodes increases. In order to reduce the path length, one can use a technique called path splitting [55]. One can halve the distance to traverse for the next search as shown in figure 4.23 by linking each obstacle to its grand parent instead of its parent [81]. This can be done

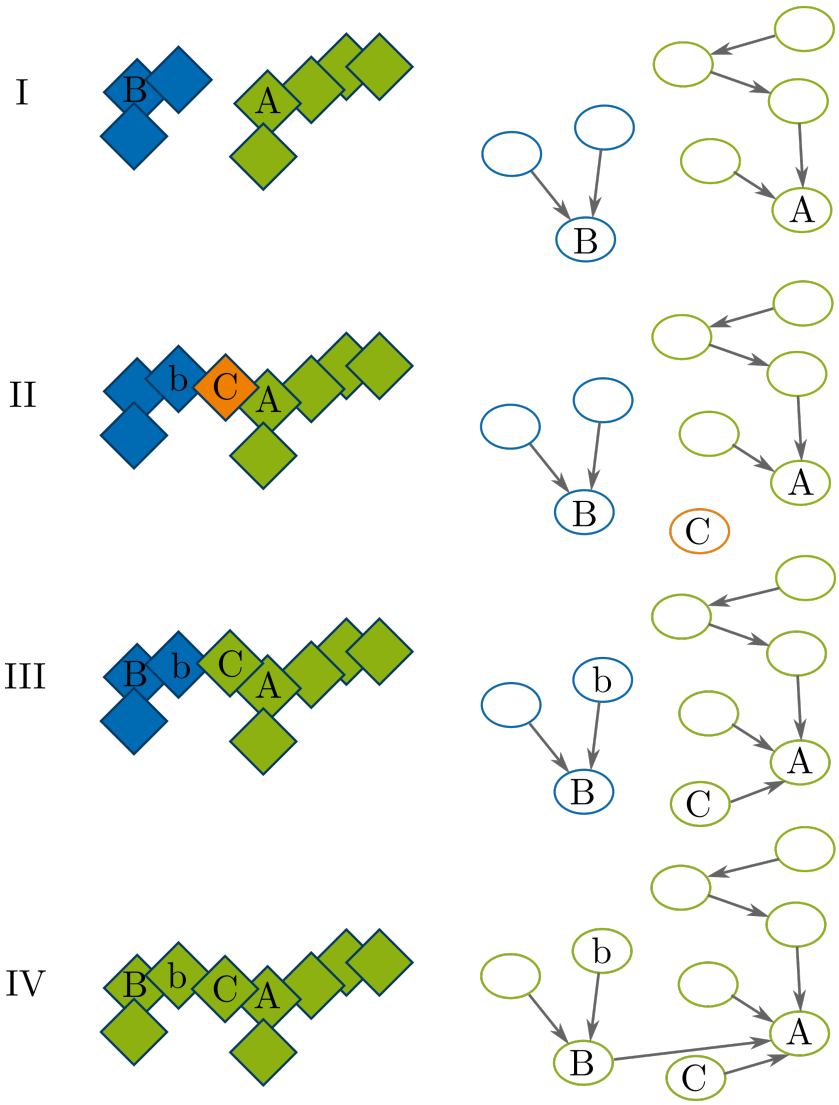

Figure 4.24 Merging procedure of two trees A and B. On the left side we show the possible obstacle configuration and the corresponding trees on the right. In the first step we have two separate clusters with roots A and B. In the second step, a new obstacle C is added to the system. The new obstacle overlaps with the squares b and A. In the third step, the new obstacle is merged with one of the trees of the obstacles it overlaps with. In this case it is tree A. Obstacle C is now part of tree A. As obstacle C also overlaps with tree B, the two trees are merged together. As tree B is larger, the root of tree B is now set as child node of the root of tree A.

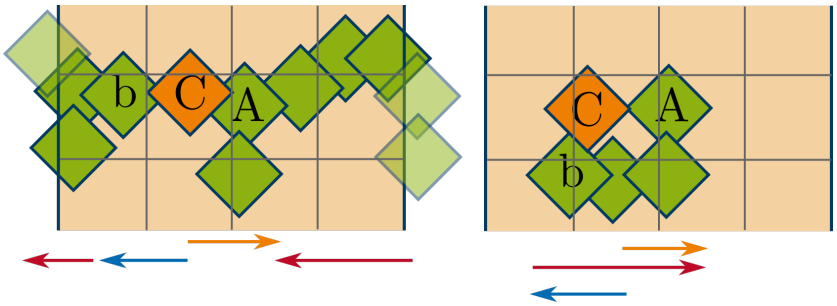

Figure 4.26 Left panel: A wrapping cluster is detected. The horizontal distance CA of obstacle C to the root of its tree (Obstacle A) is 1 cell (orange arrow). The total distance passing through obstacle b is −3 cells, as the distance Cb from obstacle C to obstacle b is −1 cell (blue arrow) and the distance from obstacle b to obstacle A is −2 cells (red arrows). Right panel: Both distances from obstacle C to the root (Obstacle A) are the same. The direct distance CA is 1 cell. The distance Cb is −1 cell (blue arrow) and the distance bA is 2 cells (red arrow). Therefore, passing through obstacle b the same distance is found and no wrapping cluster is detected.

in the `find(i)` method, that returns the root of the tree of obstacle `i` as it needs to traverse the tree anyway.

The stopping rules of the algorithm should be elucidated now. In order to detect a wrapping cluster, the distance from each obstacle to the root of its tree is computed. This is simply done by using the cell list and computing the distance in integer multiples of the cell length. If an obstacle is added that causes a cluster to wrap around the container, then there are two different distances to the root as shown in figure 4.26. The exact computation of the distances especially with periodic boundary conditions and ghost obstacles is a little tedious and not well documented in references [55] and [90]. It shall be explained here in more detail. Firstly, two extra arrays `dist_to_parent_x` and `dist_to_parent_y`, containing the distances to the parent nodes in the x- and y-directions, are needed. Each time a new obstacle `i` is added into the container, the components of the signed distance are $d_p = c_{new} - c_{parent}$, where c_{new} is the cell coordinate of the new obstacle and c_{parent} is the coordinate of the parent obstacle. If two clusters are merged, one needs to update the distance to parent of the transplanted root as described in figure 4.27. Finding the distance of a node to its root is straightforward, one only need to sum up all entries of the arrays `dist_to_parent_x` and `dist_to_parent_y` for each node while traversing the tree.

The handling of the periodic boundary conditions is straightforward. If any obstacle is closer than $2 \times r_{obs}$ of any container edge, a ghost image must

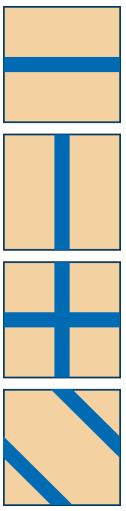

Figure 4.25 Wrapping clusters types from top to bottom: x-axis, y-axis. The next two show the possibility of a cluster wrapping on both axes.

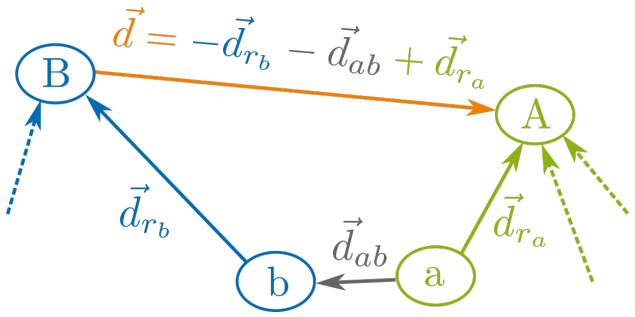

Figure 4.27 Detail of the distance update: Tree B is merged onto the bigger tree A, because obstacles a and b overlap. Root B will become a child node of root A, its distance to parent vector is updated naturally according to $\vec{d} = -\vec{d}_{r_b} - \vec{d}_{ab} + \vec{d}_{r_a}$, where $\vec{d}_{ab}$ is the cell distance between the overlapping obstacles, $vecd_{r_a}$ and $vecd_{r_a}$ their respective cell distances to the root of their trees.

be introduced on the corresponding opposite side. It must be set as child node of the real obstacle but with no distance to parent. Each ghost image of an obstacle must also be checked for overlap. Checking for obstacle overlap is identical with the methods described earlier for the Monte Carlo equilibration for non-overlapping obstacles. To speed up the overlap detection and compute the cell distances, a cell list with $l_{cell} = 2 \times r_{obs}$ can be used and one only needs to check the obstacles in the eight surrounding cells.

As stated earlier, the information needed in order to compute the percolation transition is an estimation of $P_L(a, N)$, the probability distribution that a wrapping cluster exists on a quadratic surface of side length L with N obstacles of area a. There are multiple possibilities for a wrapping cluster to occur (see figure 4.25) and the relevant probabilities required for this algorithm are [55, 90]:

1. $P_L^e(a, N)$: The probability that a cluster exists in either directions.

2. $P_L^b(a, N)$: The probability that a cluster exists in both directions.

To find the required probabilities[2], in one "run", obstacles are inserted into the container until a wrapping has occurred in both directions. Then one extracts the number N_e of obstacles for the event "a wrapping cluster in any direction has occurred" and N_b for the event "a wrapping cluster in both direction has occurred". To get the probability distributions, two associative containers implemented as `std::map<int, int>` in the standard C++

[2]Here the letter e in $P_L^e(a, N)$ stands for "either" directions, and the letter b stands for "both" directions

library are used. They hold key-value pairs with unique keys. The key values are the different numbers N_e and N_b, and the associated values are the number of occurrences of the numbers N_e and N_b after performing N_r runs. Therefore, these maps contain the histograms for the probability densities $p_L^e(a, N)$ and $p_L^b(a, N)$. To retrieve the probability distributions $P_L^e(a, N)$, and $P_L^b(a, N)$ one performs a cumulative sum of the corresponding probability densities and divides by the total number of trials. Those distributions are still discrete as they are a function of N. To obtain the continuous distribution $R_L^e(\rho)$ and $R_L^b(\rho)$ the corresponding distributions $P_L^e(a, N)$ and $P_L^b(a, N)$ are convoluted with the Poisson distribution with mean $\lambda nL^2 = \rho L^2/a$ ¸[55]:

$$R_L(\rho) = e^{-\lambda} \sum_{N=0}^{\infty} \frac{\lambda}{N!} P_L(a, N). \tag{4.23}$$

From $R_L^e(\rho)$ and $R_L^b(\rho)$ one can now extract the percolation thresholds as explained in chapter 3.4. We will give an example of the probability densities $p_L^e(a, N)$, $p_L^b(a, N)$ and their corresponding probability distributions in section 5.3.

5 Results

In this chapter, we will first focus on the wind-tree model and test the kinetic theory of Hauge and Cohen [43, 44] for the normal and anomalous transport in the EWTM. Numerical simulations have been undertaken by Wood and Lado [25], but they have not settled the question of the discrepancies between the predicted logarithmic divergence and the observed power law behaviour in the case of overlapping obstacles. Also, in order to get further insight about the nature of the anomalous diffusion, we look at the van Hove correlation function and compare it to the well-known Gaussian form in the case of normal diffusion. These results are presented in the first section of this chapter. After investigating the system in the absence of a magnetic field, the question of magnetotransport naturally arises. We have seen that one of the most basic theory to explain the Hall effect is the Drude theory whose predictions are retrieved at low densities in the Grad limit of the Boltzmann equation. But those theories fail in the presence of a magnetic field. A non-Markovian description in terms of a generalised Boltzmann equation has been derived by Bobylev *et al.* [47, 48]. Even this more involved theory is not correct for higher densities. Still, the simple Drude model gives a robust prediction of the Hall coefficient R_H even at higher densities. In the second part of this chapter, we will investigate this phenomenon. Furthermore we address the question how the magnetotransport behaves for a vanishing magnetic field if in the limit of $B = 0$, the transport is anomalous. This question is investigated by considering the EWTM with overlapping obstacles at small magnetic fields. In the last section, we turn our attention to transport processes at the percolation transition. Here a non universal behaviour has been observed by Schirmacher *et al.*[82] for the Lorentz gas with circular scatterers. We shall investigate the EWTM in this regard.

5.1 The Wind-tree Model

In the following we present the results of the numerical simulations of the wind-tree model in the case of non-overlapping and overlapping obstacles. In the non-overlapping case the diffusion is still normal. We have compared the diffusion coefficients from our simulations to the predictions of Hauge and Cohen [43, 44]. We have shown that their predictions are in good agreement with the simulations at low densities. At higher densities, a transient sub-linear regime emerges at intermediate times and seems to be associated with the deviation from the theoretical predictions. In the case of overlapping scatterers, we have settled the question of the asymptotic behaviour of the MSD at long times. We have shown that the MSD grows[1] as $t^{1-2\rho/3}$ at long times t. We show that this prediction by van Beyeren and Hauge [45] is surprisingly robust as it seems still valid for densities as high as $\rho = 0.9$ (cf. the percolation transition for oriented squares is at $\rho_c = 1.09884280(9)$[55]). We have also proposed a model for the van Hove correlation function in the wind tree model by generalising the the Gaussian function to an arbitrary exponent $\beta \leq 2$. We have shown that this exponent β is also dependent on the density and takes the empirical form

$$\beta(\rho) = \frac{2}{1 + \frac{4}{3}\rho}. \tag{5.1}$$

[1] Hauge and Cohen have chosen the diagonals of the square obstacles to have the lenght $l = 2a$ for convenience. In the following however we choose the side length of the obstacles to be of length $l = a$. This results in a conversion factor of two for the reduced density ρ.

In the rest of this section we reprint the results as published in reference [91]:

Benjamin A. Sanvee, René Lohmann, and Jürgen Horbach Phys. Rev. E 106, 024104 – Published 3 August 2022

Contribution:
I have written the simulation code. I have carried out the simulations and evaluated the results. I have also participated in the preparation of the manuscript

5.1.1 Non-overlapping Squares

First, we consider the motion of a tracer particle in the wind-tree model with non-overlapping squares. In this model, the tracer particle exhibits a non-chaotic microscopic dynamics that is diffusive on long time scales [92]. Figure 5.1 shows a typical trajectory of the tracer at the density $\rho = 0.3$. From this snapshot, one can infer the most important events that lead to higher-order "corrections" to the simple Boltzmann theory [69] where uncorrelated collisions of the tracer with the obstacles are assumed. The most important contribution to those corrections is due to the motion through small escape channels between the obstacles (see zoomed-in region in Fig. 5.1). To a lesser extent also ring collisions and retracing events (in the following also called retroreflections) contribute significantly to the leading-order corrections to the Boltzmann theory (for details see Refs. [43, 44]). For a detailed description of retracing events, we refer to the next section 5.1.2.

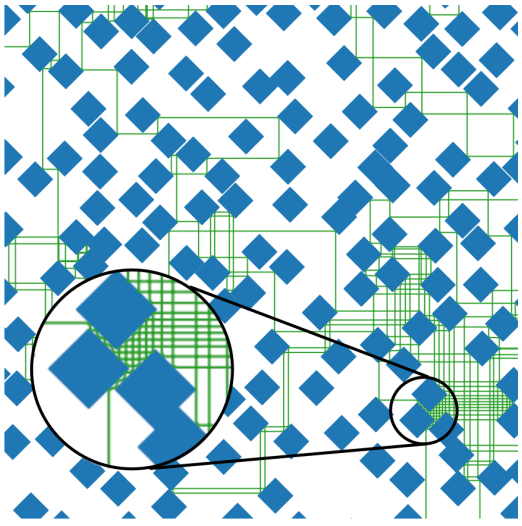

Figure 5.1 Trajectory of a tracer particle in the wind-tree model with non-overlapping (nov) squares at the density $\rho = 0.3$. In this case, small escape channels between the obstacles (see zoomed-in region) are important for the diffusive transport of the tracer.

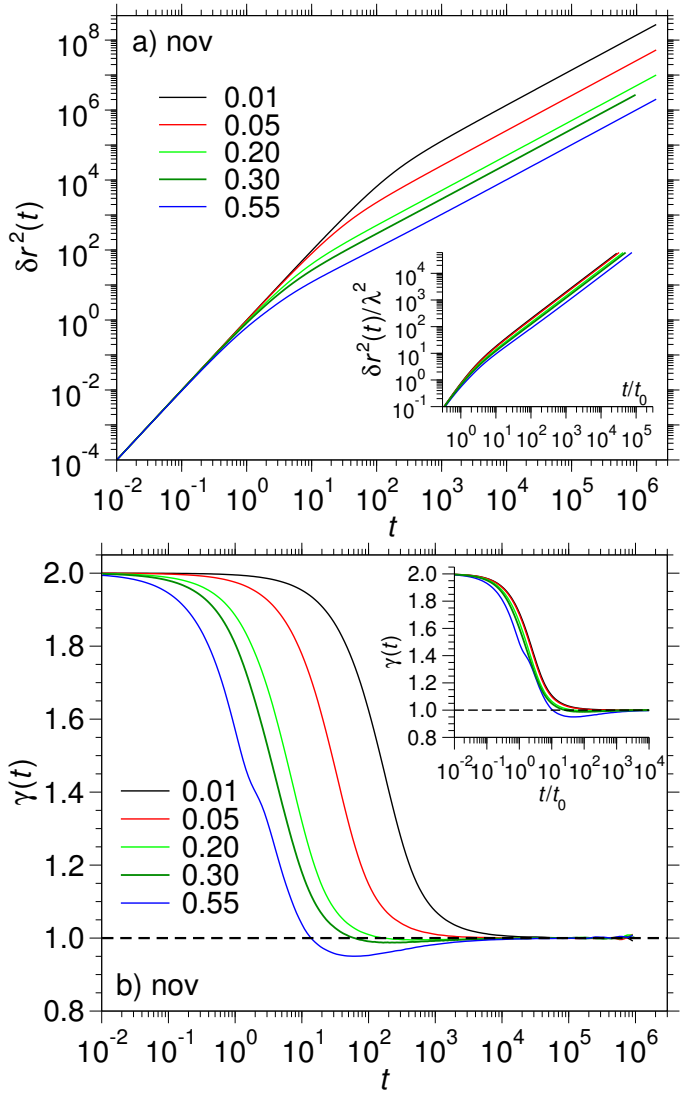

Figure 5.2 a) MSD $\delta r^2(t)$ for the wind-tree model with non-overlapping (nov) squares for different densities. The inset shows the MSD scaled with the squared mean-free path λ^2 as a function of t/t_0 (with t_0 the mean-free time). b) Exponent parameter $\gamma(t)$, as obtained from the MSDs in a) (for the definition of $\gamma(t)$ see text). The inset shows the same data as a function of t/t_0.

The central quantity, that we use to analyse the diffusion dynamics of the tracer particle, is the mean-squared displacement (MSD), defined by

$$\delta r^2(t) = \left\langle (\vec{r}_{\rm tr}(t) - \vec{r}_{\rm tr}(0))^2 \right\rangle \,, \tag{5.2}$$

with $\vec{r}_{\rm tr}(t)$ the position of the tracer particle at time t and $\langle \cdots \rangle$ an ensemble and time average over 10^5 independent trajectories. Formally, one can introduce a time-dependent exponent $\gamma(t)$ that can be obtained from the derivative of $\log(\delta r^2(t))$ with respect to $\log(t)$,

$$\gamma(t) = \frac{d\log\left(\delta r^2(t)\right)}{d\log(t)} \,. \tag{5.3}$$

For our analysis, the parameter $\gamma(t)$ will be important to quantify deviations from a linear behaviour of the MSD at intermediate and long times.

Figures 5.2a and 5.2b respectively show the MSD and the exponent $\gamma(t)$ for the system with non-overlapping obstacles for different densities. In all cases, the MSD displays a ballistic regime at short times ($\gamma = 2.0$) that crosses over to a diffusive regime in the long time limit ($\gamma = 1.0$). The time scale around which the MSD changes from the ballistic to the diffusive regime decreases with increasing density. This can be easily understood in terms of estimates of the mean-free length between two collisions, $\lambda = a/(\sqrt{2}\rho)$, and the corresponding mean-free time $t_0 = a/(\sqrt{2}v\rho)$. Although these expressions for λ and t_0 are expected to be only accurate in the dilute limit, the MSD data indicates that they are also sensible at high densities. If one plots the MSD scaled with the square of the mean-free length, $\delta r^2(t)/\lambda^2$, as a function of t/t_0, then the crossover to the diffusive regime starts around $t/t_0 = 1.0$ (see insets of Fig. 5.2a and 5.2b).

As can be inferred from the behaviour of $\gamma(t)$, from low to high densities the dynamics changes qualitatively in that towards high densities (here for $\rho \gtrsim 0.2$), a transient sublinear regime emerges on an intermediate time scale, i.e. before the diffusive regime with $\gamma = 1.0$ is reached. With respect to the reduced quantity $\delta r^2(t/t_0)/\lambda^2$, in the diffusive regime the dynamics slows down approximately by a factor of 2.5 when increasing the density from $\rho = 0.01$ to $\rho = 0.55$.

From the MSD, the self-diffusion coefficient D can be computed using the relation

$$D = \lim_{t\to\infty} \frac{\delta r^2(t)}{4t} \,. \tag{5.4}$$

According to the Boltzmann theory, the self-diffusion coefficient is given by [44, 69]

$$D_{\rm B} = \frac{1}{2}\frac{\lambda^2}{t_0} = \frac{\sqrt{2}av}{4\rho} \,. \tag{5.5}$$

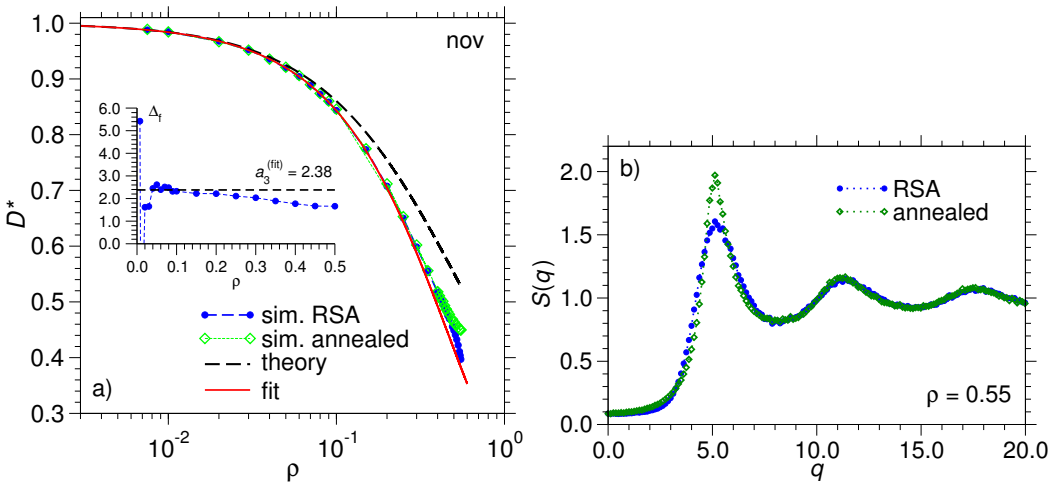

Figure 5.3 a) Reduced diffusion coefficient D^* as a function of ρ, as obtained from the simulation with obstacle configurations, generated by random sequential adsorption (RSA, blue circles) and annealing via Monte Carlo (green diamonds), in comparison to the theoretical prediction by Hauge and Cohen [44] (dashed line). For the details on the fit function (red line) see text. The inset shows Δ_f, as defined by Eq. (5.8), as a function of ρ. Here, the horizontal dashed line marks value of a_3, as used in the fit (red line) in the main plot. b) Static structure factor $S(q)$ of the obstacles at $\rho = 0.55$ for the RSA and the annealed samples.

For the wind-tree model with non-overlapping squares, Hauge and Cohen [44] have calculated the self-diffusion coefficient up to the lowest order corrections to the Boltzmann coefficient D_{B}. In terms of the reduced quantity $D^\star = D/D_{\mathrm{B}}$, their result can be written as

$$D^\star = \frac{\rho}{\kappa} \tag{5.6}$$

with

$$\kappa = \rho + a_2\rho^2 + a_3\rho^3 + \mathcal{O}(\rho^4)\,. \tag{5.7}$$

In the framework of the theory of Hauge and Cohen [44], it has been only possible to estimate the coefficient a_2 which is given by $a_2 = 1.62525$. We have estimated the coefficient a_3 from a fit of Eqs. (5.6) and (5.7) to our numerical data of $D^\star$. To see over which density range a fit up to third order in κ is sensible, we have first considered the quantity

$$\Delta_{\mathrm{f}} = \frac{(D^\star)^{-1} - 1 - a_2\rho}{\rho^2}\,, \tag{5.8}$$

which, according to Eqs. (5.6) and (5.7), is equal to $a_3 + \mathcal{O}(\rho)$. The inset of Fig. 5.3a shows Δ_{f} as a function of density. As can be inferred from this plot, a fit to $D^\star$ with Eqs. (5.6) and (5.7) should be sensible up to $\rho \approx 0.1$ and the value of a_3 is about 2.38 (horizontal dashed line in the figure). The main part of Fig. 5.3a shows the reduced self-diffusion coefficient $D^\star$ as a function of the logarithm of the density. The theoretical result, i.e. the result including the a_2 term in Eq. (5.7), is in excellent agreement with the simulation up to a density of about 0.05. It seems that the low-order kinetic theory starts to fail in a density regime where a transient sublinear regime in the MSD starts to emerge (cf. Fig. 5.2). As mentioned before, the reduced self-diffusion coefficient $D^\star$ up to a density $\rho \approx 0.1$ is well described, too, if one includes the a_3 term in Eq. (5.7). The corresponding result is the red solid line in Fig. 5.3 where we have considered a_3 as a fit parameter. We find the value $a_3 = 2.37961$ (note that we only give this number with this precision to allow the interested reader to reproduce the fit in Fig. 5.3a).

Also included in Fig. 5.3a are results for $D^\star$, as obtained from the annealed obstacle samples. While for low densities there is no significant difference between $D^\star$ from the annealed and the RSA samples, for $\rho \gtrsim 0.5$ the coefficient $D^\star$ for the annealed samples is larger than that for the RSA samples. This effect becomes more pronounced with increasing density such that at the highest considered density, $\rho = 0.55$, a deviation of about 10% is observed. The difference between the annealed and the RSA structure of

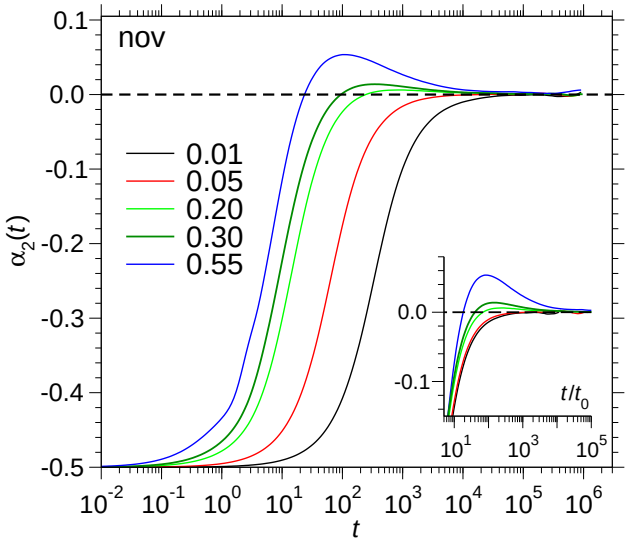

Figure 5.4 Non-Gaussian parameter $\alpha_2(t)$ at different densities for the wind-tree model with non-overlapping (nov) squares. The inset shows the same data as a function of t/t_0.

equally oriented squares can be quantified in terms of the static structure factor [93], defined by

$$S(q) = \left\langle \frac{1}{N} \left| \sum_{i=1}^{N} \exp\left(i\vec{q} \cdot \vec{r}_i\right) \right|^2 \right\rangle \tag{5.9}$$

with $\langle \dots \rangle$ an ensemble average, N the number of obstacles, $\vec{q}$ the wave vector, and $\vec{r}_i$ the position of the center of square i. Note that for a completely random system such as the overlapping squares discussed below, the static structure factor is equal to one for all values of q. Figure 5.3b displays the $S(q)$'s for the highest considered density $\rho = 0.55$. The main difference between the $S(q)$ for the RSA samples and that of the annealed samples is the amplitude of the first peak at $q_\mathrm{m} \approx 5.1$ (the so-called first sharp diffraction peak), which is about 25% higher for the case of the annealed samples. The peak at q_m measures the ordering of the samples on the length scale of nearest neighbours (i.e. on a length scale of the order of a). Our finding that the more pronounced correlations on this length scale are associated with a higher diffusion coefficient is an interesting feature and deserves further investigations.

Further insight into the dynamics in the intermediate time regime between the ballistic and the diffusive regime is provided by the non-Gaussian

parameter α_2, defined by [58]

$$\alpha_2(t) = \frac{\delta r^4(t)}{2\left[\delta r^2(t)\right]^2} - 1\,, \tag{5.10}$$

with $\delta r^4(t) = \langle(\vec{r}_{\rm tr}(t) - \vec{r}_{\rm tr}(0))^4\rangle$. Figure 5.4 shows $\alpha_2(t)$ for different densities, using the RSA protocol for generating the obstacle configurations. At very short times, the tracer particle moves ballistically with a constant velocity v which implies $\delta r^2(t) = v^2t^2$ and $\delta r^4(t) = v^4t^4$. Thus, one expects that initially $\alpha_2 = -0.5$ and, as can be seen in Fig. 5.4, this is indeed the case. In the long-time diffusive regime, the non-Gaussian parameter vanishes. In between the two latter regimes, the behavior of $\alpha_2(t)$ changes qualitatively with increasing density. While at the two low densities $\rho = 0.01$ and $\rho = 0.05$ this quantity is monotonously increasing towards zero, it exhibits a maximum with a positive amplitude for $\rho \gtrsim 0.2$. For $\rho = 0.55$, this maximum is located at $t/t_0 \approx 75$ (see inset of Fig. 5.4). Thus, the emergence of a sublinear regime in the MSD is associated with a maximum in $\alpha_2(t)$, the amplitude of which is increasing with increasing density. These features are not captured in the framework of the low-order kinetic theory by Hauge and Cohen [43, 44]. To go beyond their theory, valid approaches would be repeated-ring and self-consistent ring kinetic theories [69, 94–96].

5.1.2 Overlapping Squares

The diffusive transport in the wind-tree model with overlapping squares is very different from the one with non-overlapping squares. While in the latter case the transport is diffusive in the long-time limit $t \to \infty$, in the former case, a subdiffusive transport is asymptotically seen at any finite obstacle density and thus the diffusion coefficient is zero. In the following, we present a detailed analysis of this subdiffusive transport, considering the MSD and the distribution of particle displacement, i.e. the van Hove correlation function, as obtained from our simulation.

Figure 5.5 shows trajectories of the wind-tree model with overlapping squares for three different densities, each taken over a time of $10^5/t_0$. The trajectories indicate that the spatial region that is explored by the tracer particle over a given time (scaled by t_0) decreases drastically with increasing density. This is due to the fact that the tracer's trajectories display a strong intermittency. Regions where the particle is localized for a long time are followed by regions where it quickly moves over a relatively large distance. The latter parts of the trajectory appear to be the lighter regions in Fig. 5.5; the length scale associated with these regions decreases with increasing density.

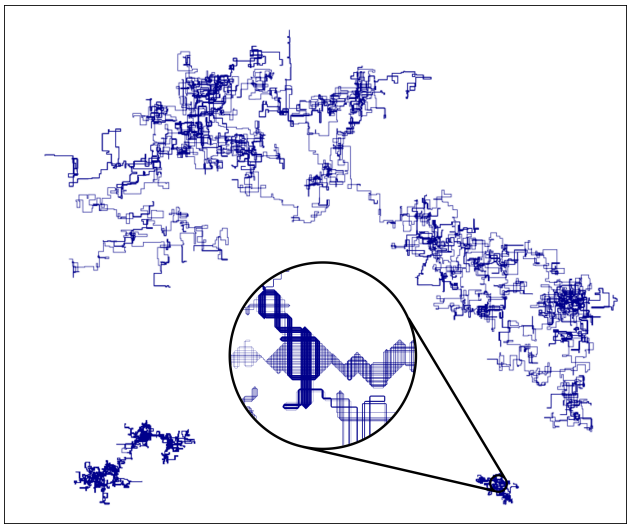

Figure 5.5 Trajectories of the wind-tree model with overlapping (ov) squares at the densities $\rho = 0.2$ (top), $\rho = 0.4$ (bottom left) and $\rho = 0.6$ (bottom right). The three trajectories are obtained over a time of $10^5/t_0$. For $\rho = 0.6$, a small region of the trajectory is magnified.

The dark regions of the trajectory where the particle is localized for a long time are due to back and forth reflections between obstacles.

These retracing events or retroreflections require the presence of at least one pair of overlapping squares such that a wedge-shaped free area is formed where the trajectory is reflected (see upper panel of Fig. 5.6). As a result, the particle almost returns to the point where it was before at an earlier time. The lower panel of Fig. 5.6 shows local parts of a trajectory at $\rho = 0.3$. Here, the zoomed-in regions display a high concentration of reflections and indicate that retroreflections dominate the transport in the wind-tree model with overlapping squares. We note that retracing events can also happen due to a pair of non-overlapping squares. However, in this case one would never get a high concentration of reflections as indicated by the trajectories in Fig. 5.6. As a consequence, retracing events do not dominate the transport in the case of non-overlapping squares (see Sec. IIIA).

The kinetic theory of Hauge and Cohen [43, 44] predicts that, as a consequence of retroreflections in the overlapping square case, the MSD grows asymptotically like $t/\ln t$. In a later heuristic approach, Van Beyeren and Hauge [45] found a different asymptotic behavior (i.e. in the limit $t \to \infty$) that can be written as

$$\delta r^2(t) = A \left(\frac{t}{t_0} \right)^{2/d_w} , \tag{5.11}$$

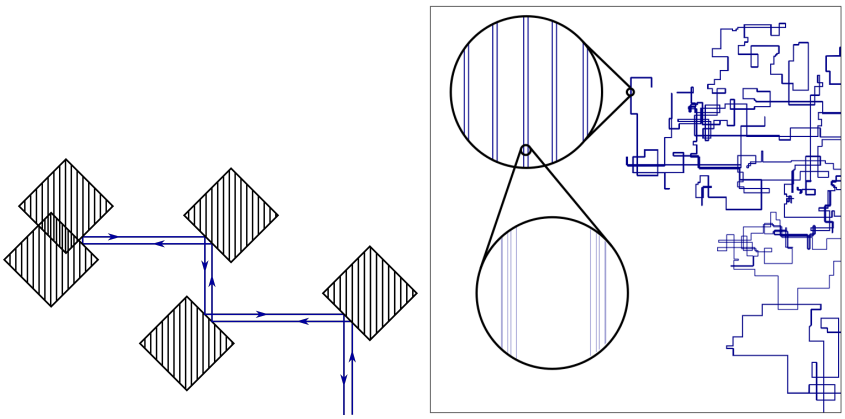

Figure 5.6 The *upper panel* illustrates a basic retracing (or retroreflective) path in the wind-tree model with overlapping (ov) squares. *Lower panel:* Detailed view on a trajectory at $\rho = 0.3$. The magnified regions indicate the occurrence of retroreflections.

with A an amplitude, that will be further specified below, and d_w the walk dimension [77] which is given by

$$d_w = \frac{2}{1 - \frac{2}{3}\rho} \,. \tag{5.12}$$

Thus, the walk dimension depends on density such that $d_w > 2$ (note that $d_w = 2$, corresponding to normal diffusion, is obtained in the limit $\rho \to 0$).

Figure 5.7a shows the MSD scaled with the mean-free path, $\delta r^2(t)/\lambda^2$, for different densities in the range $0.05 \leq \rho \leq 0.9$. At long times, the MSD follows a power law $\propto t^{\gamma_a}$ with a density-dependent exponent γ_a. While this exponent is close to one for small density, it significantly decreases below one for higher densities. This can be clearly inferred from the "time-dependent diffusion coefficient" $D(t)$, defined by the time derivative of the MSD,

$$D(t) = \frac{1}{4}\frac{d\delta r^2(t)}{dt} \,, \tag{5.13}$$

that is plotted in the inset of Fig. 5.7 a), scaled with the Boltzmann diffusion coefficient D_B, as given by Eq. (5.5). In the limit $\rho \to 0$, the ratio $D(t)/D_B$ is expected to be equal to 1.0, and indeed at the lowest density, $\rho = 0.05$, it is close to one and decreases by less than a factor of 2 from $t/t_0 \approx 1.0$ to $t/t_0 \approx 10^8$ (of course, also at this density, we expect $D(t)/D_B \to 0$ for $t \to \infty$). However, at the highest density, $\rho = 0.9$, the reduced quantity $D(t)/D_B$ decreases by about 5 orders of magnitude in the same time window.

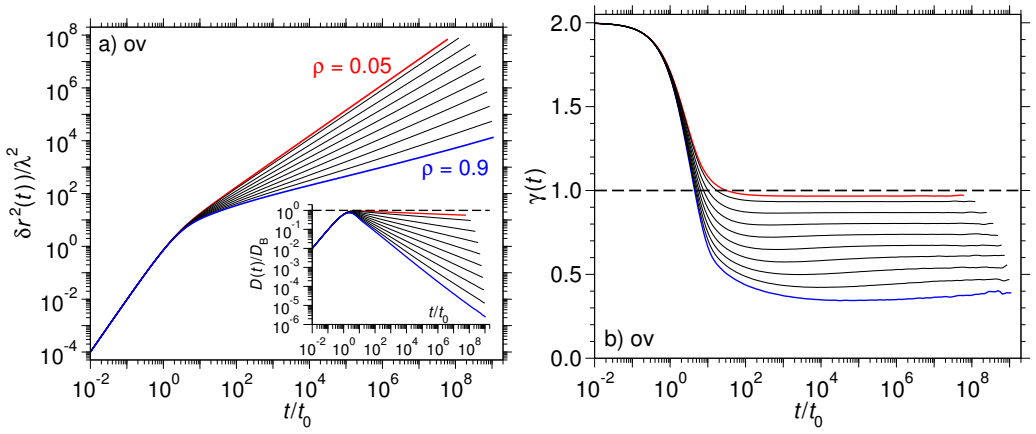

Figure 5.7 a) Scaled MSD $\delta r^2(t)/\lambda^2$, for the windtree model with overlapping (ov) squares at different densities, starting at $\rho = 0.05$ (top curve in red) and then in density steps of 0.1 from $\rho = 0.1$ to $\rho = 0.9$ (lowest blue curve). The inset shows $D(t)/D_B$, calculated from the derivative of the MSDs with respect to time. b) Exponent parameter $\gamma(t)$, as obtained from the MSDs.

To determine the asymptotic exponent γ_a for the different densities, we have determined the exponent parameter $\gamma(t)$ (Fig. 5.7b). For all the considered densities, one can read off a constant for long times which is the estimate for the asymptotic exponent γ_a. From Fig. 5.7b, one can also infer that with increasing density the regime at which one approaches the asymptotic exponent γ_a shifts to longer and longer times. This is the reason why we only consider densities $\rho \leq 0.9$. Thus, for higher densities much longer runs would be required and, by approaching the percolation transition at $\rho_c = 1.09\ldots$, also much larger system sizes have to be simulated to allow for a reasonable finite-size scaling analysis. Both requirements, i.e. longer runs and larger system sizes, are beyond the scope of the present study.

The values of $\gamma_a(\rho)$, as estimated from the simulation, are shown in Fig. 5.8 a) in comparison to the prediction according to Eqs. (5.11) and (5.12), $\gamma_a = 1 - \frac{2}{3}\rho$. Excellent agreement is found over the whole considered density range. This is surprising because the linear dependence of γ_a on ρ is only supposed to hold in the limit of low densities [45].

We now discuss the amplitude A in Eq. (5.11) for the MSD. In the limit $\rho \to 0$, the amplitude should approach $A_0 = 4D_B t_0$. Then, Eq. (5.11) reduces to $\delta r^2(t) = 4D_B t$, as required. For the amplitude A, we make an ansatz that is similar to the kinetic theory expression for the diffusion coefficient in the non-overlapping case, cf. Eqs. (5.6) and (5.7),

$$A(\rho) = 4t_0 \frac{av}{2\sqrt{2}} \frac{1}{\kappa}\,, \tag{5.14}$$

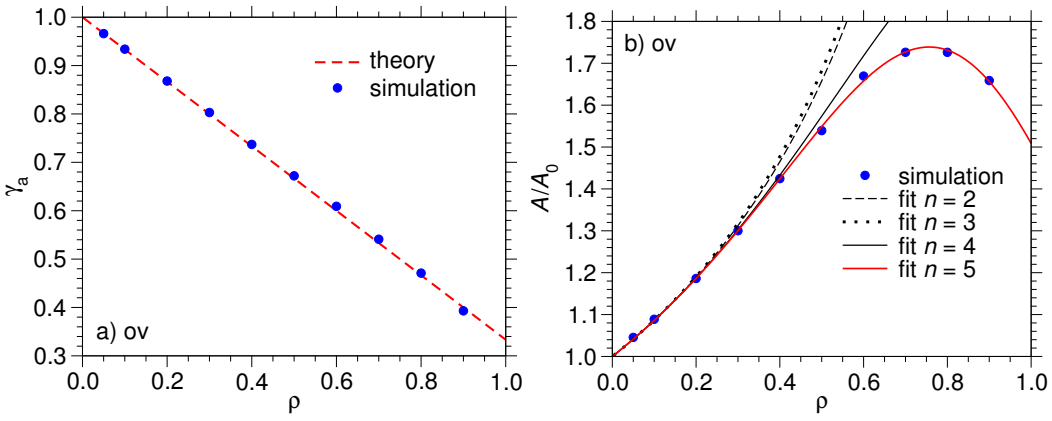

Figure 5.8 a) Asymptotic exponent $\gamma_a = \lim_{t\to\infty} \gamma(t)$ as a function of ρ versus the low-density prediction of kinetic theory, $\gamma_a = 1 - \frac{2}{3}\rho$ (red dashed line). b) Amplitude ratio A/A_0 as a function of density. The lines represent fits to Eq. (5.16) with different values of n.

with

$$\kappa = \sum_{j=1}^{n} c_j \rho^j + \mathcal{O}(\rho^{n+1}) \,. \tag{5.15}$$

Here, $c_1 = 1.0$ and the coefficients $c_2, \ldots, c_n$ are fit parameters. With Eqs. (5.14) and (5.15), we obtain

$$\frac{A}{A_0} = \frac{1}{1 + \sum_{j=2}^{n} c_j \rho^{n-1}} \,. \tag{5.16}$$

Using different values of n, this formula is employed in Fig. 5.8b as a fit function to the estimates of the ratio A/A_0, as obtained from the MSDs of our simulation. For the coefficients, we find the values $c_2 = -0.79351$, $c_3 = -0.0355161$, $c_4 = 0.328926$, and $c_5 = 0.16285$ (again, we give the coefficients with 5 or more digits to allow for a reproduction of the fit in Fig. 5.8). As indicated in the figure, the fit function with $n = 5$ is required to describe the data up to the density $\rho = 0.9$.

Further insight into the transport properties is provided by the van Hove correlation function,

$$G(\vec{r}, t) = \langle \delta \left(\vec{r} - (\vec{r}_{\rm tr}(t) - \vec{r}_{\rm tr}(0)) \right) \rangle \,, \tag{5.17}$$

which corresponds to the probability that the tracer particle has performed a displacement $\vec{r}$ within a time t. Due to the isotropy of the transport in our model, the van Hove correlation function only depends on the magnitude of

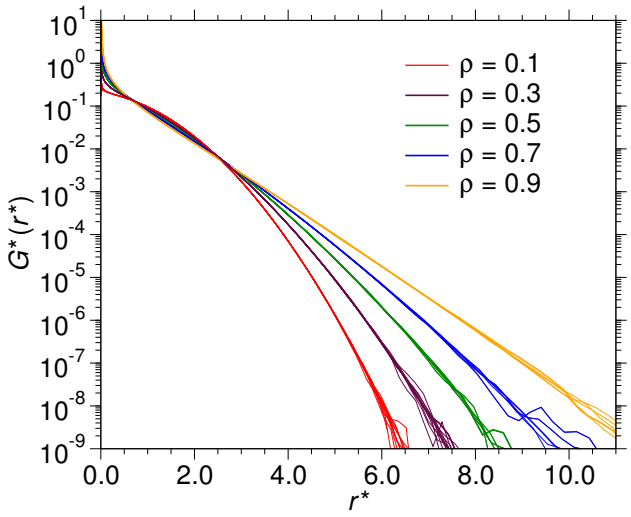

Figure 5.9 Scaled van Hove correlation function $G^\star(r^\star)$ of the wind-tree model with overlapping squares at different densities, calculated from $G(r,t)$ for times in the asymptotic subdiffusive regime (see text).

$\vec{r}$, i.e. on $r \equiv |\vec{r}|$. In the case of normal diffusion, the function $G(r,t)$ is a Gaussian,

$$G(r,t) = \frac{1}{2\pi\sigma^2(t)} \exp\left(-\frac{r^2}{2\sigma^2(t)}\right) , \tag{5.18}$$

where the standard deviation $\sigma(t)$ is given by $\sigma(t) = \sqrt{\delta r^2(t)/2}$. Note that the MSD $\delta r^2(t)$ is the second moment of $G(r,t)$. Obviously, in the case of a Gaussian distribution the following relation holds:

$$G^\star(r^\star) = G(r,t)\,\sigma^2(t)\,, \tag{5.19}$$

where $r^\star = r/\sigma(t)$. Thus, the function $G^\star(r^\star)$ only depends on $r^\star$ and not explicitly on time t.

For the wind-tree model with overlapping squares, we do expect that, in the asymptotic long-time regime, $G(r,t)$ is not a Gaussian, since this model exhibits asymptotically a density-dependent subdiffusive transport that deviates more and more from diffusive transport with increasing density. Thus, we expect that asymptotically $G(r,t)$ is a non-Gaussian function that changes its functional form with increasing density. However, as Fig. 5.9 demonstrates, the function $G^\star$ for this model is consistent with the property (5.19). Here, we have determined $G^\star$ for different densities, at each density based on $G(r,t)$ at 10 equidistant times, taken from the time intervals $4\times10^5 \le t \le 6.4\times10^7$ for $\rho \le 0.4$, $10^6 \le t \le 6.4\times10^7$ for $\rho = 0.5$ and $\rho = 0.6$, $7\times10^6 \le t \le 6.4\times10^7$ for $\rho = 0.7$, and $10^7 \le t \le 6.4\times10^7$ for

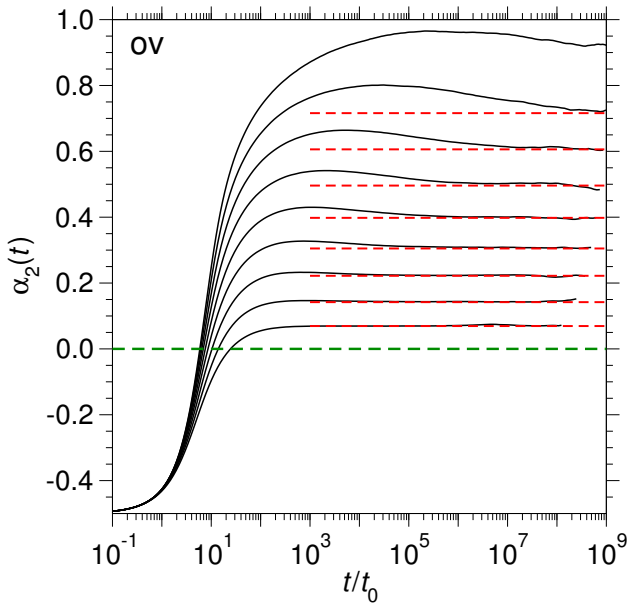

Figure 5.10 Non-Gaussian parameter $\alpha_2(t)$ for densities $\rho = 0.1$ (lowest curve) to $\rho = 0.9$ (top curve) in density steps of 0.1. The dashed red lines mark the asymptotic values of $\alpha_2(t)$.

$\rho = 0.8$ and $\rho = 0.9$. For $\rho \leq 0.8$, these time intervals correspond to the asymptotic subdiffusive regime. At all the considered densities, the curves for the different times fall onto a master curve and therefore we can conclude that Eq. (5.19) holds. Note that in Fig. 5.9 we have used $\sigma^2(t) = \delta r^2(t)/2$ to determine $G^\star(r^\star)$. Below we compute $G^\star$ using a slightly different formula for $\sigma^2(t)$ which, however, differs from the former expression only by a constant, cf. Fig. 5.11 and Eq. (5.24).

To further specify the functional form of the van Hove correlation function, we now consider the non-Gaussian parameter α_2, as defined by Eq. (5.10). Figure 5.10 shows $\alpha_2(t)$ for different densities. As can be inferred from the figure, α_2 approaches a density-dependent constant, $\alpha_2^{(a)}$, at long times (dashed red lines).

What is the form of the van Hove correlation function in the long-time regime by which the constant $\alpha_2^{(a)}$ and its density dependence could be described? The non-Gaussian parameter is obtained from $\delta r^4(t)$ and $\delta r^2(t)$, corresponding to the fourth and second moment of $G(r,t)$, respectively. The nth moment of $G(r,t)$ is defined by

$$\delta r^n(t) = \int d^2r\, r^n G(r,t)\,. \tag{5.20}$$

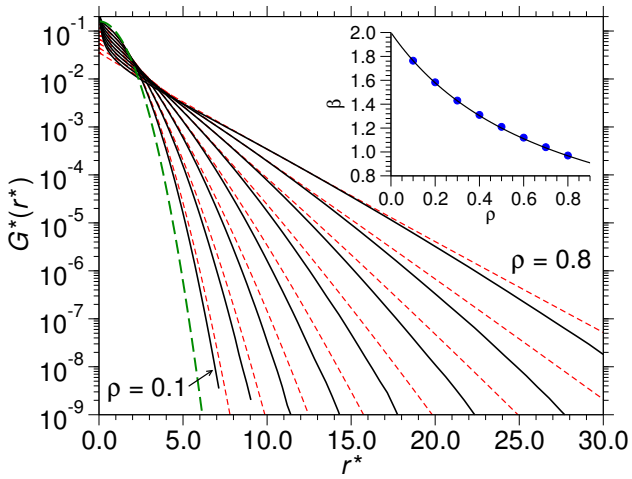

Figure 5.11 Averaged correlation function $G^\star(r^\star)$ for densities from $\rho = 0.1$ to $\rho = 0.8$ in steps of 0.1. The dashed green line is the Gaussian function $\exp\left[-(r^\star)^2/2\right]/(2\pi)$. The inset shows the exponent β as a function of density. Here, the solid black line is the function $\beta(\rho) = 2/(1 + \frac{4}{3}\rho)$.

Both the property (5.19) and the constant $\alpha_2^{(a)}$, that are obtained at long times, are reproduced by the following generalization of the Gaussian function (5.18),

$$G(r,t) = \frac{\beta}{2\pi 2^{2/\beta}\sigma^2\Gamma(2/\beta)} \exp\left[-\frac{1}{2}\left(\frac{r}{\sigma(t)}\right)^\beta\right], \tag{5.21}$$

with $\beta < 2$ an exponent that decreases with increasing density and $\Gamma(x) = \int_0^\infty dt\, t^{x-1}\mathrm{e}^{-t}$.

Using polar coordinates and Eq. (5.21) for $G(r,t)$, one obtains

$$\begin{aligned}\delta r^n(t) &= \frac{2\pi\beta}{2\pi 2^{2/\beta}\sigma^2\Gamma(2/\beta)} \int_0^\infty r dr\, r^n \exp\left[-\frac{1}{2}\left(\frac{r}{\sigma(t)}\right)^\beta\right] \\ &= 2^{n/\beta}\sigma^n \frac{\Gamma\left(\frac{n+2}{\beta}\right)}{\Gamma\left(\frac{2}{\beta}\right)}\,. \end{aligned} \tag{5.22}$$

Thus, with Eqs. (5.10) and (5.22) the non-Gaussian parameter is given by

$$\alpha_2 = \frac{1}{2}\frac{\Gamma\left(\frac{6}{\beta}\right)\Gamma\left(\frac{2}{\beta}\right)}{\left(\Gamma\left(\frac{4}{\beta}\right)\right)^2} - 1\,. \tag{5.23}$$

This equation implies that α_2 does not depend on σ. Therefore, at a given density it is a constant with a density-dependent exponent β.

Figure 5.11 shows $G^\star(r^\star)$ for densities from $\rho = 0.1$ to $\rho = 0.8$ in steps of 0.1, as obtained from averages over different times in the asymptotic regime. To obtain $G^\star(r^\star)$, we have determined σ from the MSD $\delta r^2(t)$, using the relationship between $\delta r^2(t)$ and $\sigma(t)$ that follows from Eq. (5.22),

$$\sigma^2 = 2^{-2/\beta} \frac{\Gamma\left(\frac{2}{\beta}\right)}{\Gamma\left(\frac{4}{\beta}\right)} \delta r^2(t) \,. \tag{5.24}$$

The value of β is computed via Eq. (5.23), using for α_2 the asymptotic value $\alpha_2^{(\mathrm{a})}$ (cf. Fig. 5.10). The resulting β as a function of density are displayed in the inset of Fig. 5.11. Here, the black solid line represents the function

$$\beta(\rho) = \frac{2}{1 + \frac{4}{3}\rho} \,. \tag{5.25}$$

It is not obvious how this function is related to the walk dimension d_w. So up to now we consider Eq. (5.25) as an empirical fit function that provides a very good description of the estimated exponents β from the simulation.

For comparison the Gaussian function $\exp[-(r^\star)^2/2]/(2\pi)$ is included in Fig. 5.11 (dashed green line). The plot indicates that the measured $G^\star(r^\star)$ deviate more and more from a Gaussian function with increasing density. The dashed red lines in Fig. 5.11 represent the function

$$\begin{aligned} G^\star(r^\star) = {} & \frac{1}{\pi 2^{1+4\rho/3}(1 + \frac{4}{3}\rho)\Gamma(1 + \frac{4}{3}\rho)} \times \\ & \times \exp\left[-\frac{1}{2}(r^\star)^{2/(1+4\rho/3)}\right] , \end{aligned} \tag{5.26}$$

which is obtained by combining Eqs. (5.19), (5.21), and (5.25). Keeping in mind that Eq. (5.26) does not contain any fit parameters, one can conclude that this formula provides a fair description of the scaled van Hove correlation function $G^\star(r^\star)$.

5.1.3 Summary and Conclusions

We have presented extensive event-driven molecular dynamics simulations of the EWTM with random obstacle configurations of equally-oriented non-overlapping or overlapping squares. For both cases, i.e. non-overlapping and overlapping squares, a regime of obstacle densities has been considered that goes well beyond the density regime $\mathcal{O}(\rho^2)$ where the kinetic theory of Hauge and Cohen (HC) [44] is expected to hold. For the case of overlapping squares,

we have investigated the EWTM for densities up to $\rho = 0.55$ and for non-overlapping squares densities up to $\rho = 0.9$ which is below the percolation threshold at $\rho_c = 1.09884280(9)$. For the overlapping squares, we have not considered the regime of very high densities close to ρ_c, because this would have required much longer runs to reach the asymptotic long-time regime (already at $\rho = 0.9$, this regime is hardly reached on the considered time scale of 10^9). Such runs go beyond the scope of the present study. However, apart from the regime close to ρ_c for the overlapping squares, our study provides reference data for future theoretical approaches to the EWTM beyond the low-density regime.

For the EWTM with non-overlapping squares, the HC theory is in good agreement with the simulation up to densities of the order of 0.05. In this density regime, i.e. $0 \leq \rho \lesssim 0.05$, the diffusion coefficient D decreases to about 10% below the Boltzmann diffusion coefficient D_B (cf. Fig. 5.3). For densities up to about 0.1, one has to take into account the term $\mathcal{O}(\rho^3)$ in the expansion of the inverse diffusion coefficient. From our simulation, we have estimated $a_3 \approx 2.38$, corresponding to the coefficient of this third-order term. We have seen that the higher-order terms (i.e. $\mathcal{O}(\rho^n)$ with $n \geq 3$) are associated with the emergence of a maximum in the non-Gaussian parameter α_2 and an emerging sublinear regime in the MSD. Furthermore, for $\rho \gtrsim 0.5$ the reduced diffusion coefficient $D^\star$ starts to depend on the protocol with which the obstacle samples are generated. Interestingly, the diffusion coefficient, as obtained from the annealed samples, is higher than that from the RSA samples. All these features could probably be described in the framework of kinetic theories that are suited for dense systems such as repeated-ring and mode-coupling approaches [94–96]. Whether these approaches would also lead to an accurate quantitative description, is an interesting issue for forthcoming studies.

The EWTM with overlapping squares is one of the rare examples of a simple model system that shows an asymptotic subdiffusive transport, i.e. the MSD grows sublinearly, $\delta r^2(t) = At^{2/d_\mathrm{w}}$, with a density-dependent walk dimension d_w. This subdiffusive behavior reflects the dominant contributions of retroreflections to the long-time diffusive transport. Van Beyeren and Hauge [45] have argued that the walk dimension is given by $d_\mathrm{w} = 2/(1 - 2\rho/3)$ in the low-density limit. Surprisingly, our simulation is consistent with this prediction up to densities as high as $\rho = 0.9$. However, the amplitude A of the MSD has a strong dependence on density and one has to take into account terms up to $\mathcal{O}(\rho^5)$ with respect to the expansion of A^{-1}, in order to fit the simulation data up to $\rho = 0.9$ (cf. Fig. 5.8b). An interesting theme for forthcoming studies is to investigate how the anomalous transport due to retroreflections is affected when approaching the percolation transition at ρ_c.

A possible scenario might be as follows: When approaching ρ_c from below, the prediction by van Beyeren und Hauge might still hold. However, the time scale, where the subdiffusive behavior with $d_w = 2/(1 - 2\rho/3)$ starts to emerge, increases with increasing density such that at ρ_c this time scale diverges. It has to be seen whether this conjecture about the interplay between subdiffusion due to retroreflection and the anomalous transport due to the percolation transition is correct.

We have also proposed a model for the long-time regime of the van Hove correlation function $G(r, t)$ for the EWTM with overlapping squares. Since, at long times, the non-Gaussian parameter approaches a constant and the scaling relation (5.19) holds, we have proposed that $G(r, t)$ has the form of a generalized Gaussian function, Eq. (5.21), with an exponent β that we have directly determined from the long-time limit of α_2. We find the empirical function $\beta(\rho) = 2/(1+4\rho/3)$ and thus a closed expression for $G^\star(r^\star)$, given by Eq. (5.26). We observe significant deviations of this function to the $G^\star(r^\star)$, as obtained from the simulation. This indicates that the generalized Gaussian function (5.21) is only an approximation to the long-time behavior of the van Hove correlation function $G(r, t)$.

Due to its simplicity, the EWTM could be well suited for the further development of kinetic theories for dense fluid systems. The results, presented in this paper, provide a reference for a quantitative check of such theories.

5.2 Magneto-transport

As we have seen in chapter 3.1, the Drude theory is only valid in the limit of low densities and in the limit of vanishing magnetic fields. However the prediction of the Hall coefficient is quite accurate even towards higher densities. In this section, we will investigate the origin of this robustness. Some of the data published in reference [30] is reused in this thesis and a part of the results presented here are to be published later. At the end of this section, the magneto-transport in the EWTM shall be investigated, especially the behaviour at low magnetic fields is interesting as at $B = 0$ we are faced with a vanishing diffusion coefficient at all densities.

5.2.1 Magneto-transport in the Lorentz Gas with Circular Scatterers

In the framework of the Drude model one obtains a direct relation between the longitudinal conductivity and the Hall conductivity if one divides equation (3.18) by (3.19):

$$\sigma_{xy} = \omega_c \tau \sigma_{xx}. \tag{5.27}$$

The Drude time (or mean free time) between two collisions is assumed to be independent of the magnetic field. We have seen in section 3.2 that this assumption cannot be upheld and a more general Boltzmann equation with a

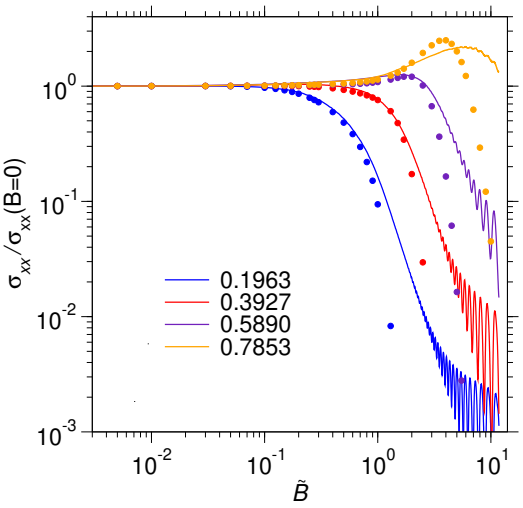

Figure 5.12 Comparison between experiment (solid lines) and simulation (circles) for the reduced conductivity $\sigma_{xx}/\sigma_{xx}(B = 0)$ as a function of $\tilde{B}$ for different values of ρ.

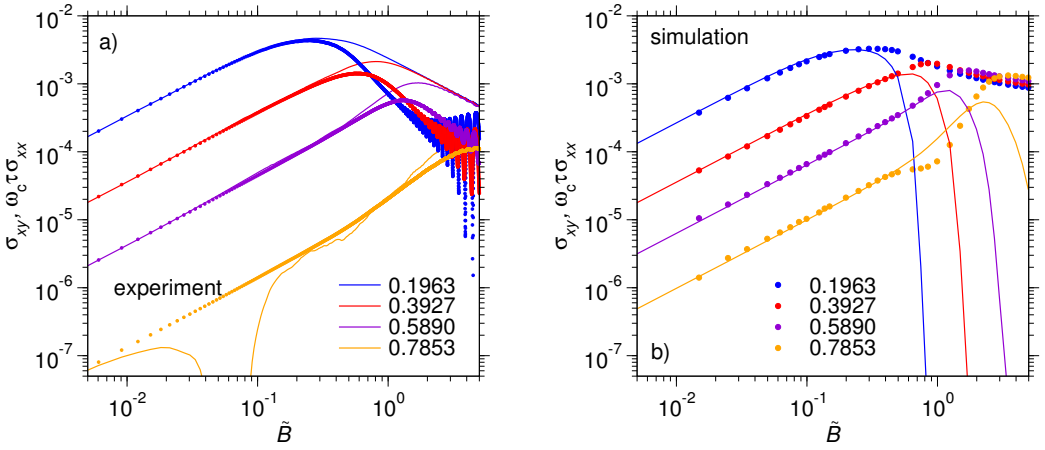

Figure 5.14 Hall conductivity σ_{xy} (circles) and $\omega_c\tau\sigma_{xx}$ (solid lines) as a function of $\tilde{B}$ for different densities for a) the experiment and b) the simulation.

magnetic field dependent τ_D was presented (see equations (3.33) and (3.38)). These theories are only valid in the low-density limit. However, we will see that the predictions of the Hall coefficient in the simpler Drude model is still accurate towards higher densities for sufficiently small magnetic fields. We will see that this is linked to a similar density dependence of the Drude time τ and the zero field conductivity $\sigma_{xx}(B = 0)$.

The measurements where done on systems with four different densities, namely $\rho = 0.1663, 0.3927, 0.5890$ and 0.7853. The obstacles have an effective radius of 1 μm. The same densities where also used in the simulations. For each density, the components D_{ij} of the diffusion tensor where computed for different magnetic fields ranging from $B = 5 \times 10^{-3}$ to $B = 8$. In each run, 10000 obstacles of radius $r = 0.5$ where placed randomly into the simulation box. We averaged over 2×10^4 trajectories distributed across 2000 different simulation boxes with independent obstacle configurations. The trajectories where computed over a time of $t = 10^6$.

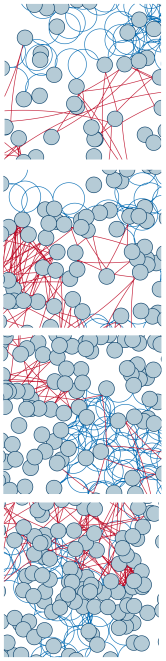

Figure 5.13 Trajectories from the simulation at $\tilde{B} = 0.05$ (red lines) and $\tilde{B} = 0.5$ (blue lines). From top to bottom the densities are $\rho = 0.1963$, 0.3927, 0.5890 and 0.7853.

Figure 5.13 shows example trajectories from the simulations at these densities. A juxtaposition of the reduced conductivities $\sigma_{xx}/\sigma_{xx}(B = 0)$ obtained from the experiments (solid lines) and from the simulations (circles) is shown in figure 5.12. The results are plotted on a double-logarithmic scale with $\tilde{B} = B/B_0$ on the x-axis. One can see that at low B-fields the values of σ_{xx} are very close to those of $\sigma_{xx}(B = 0)$ for all densities. For low densities, the conductivity decreases monotonically with increasing magnetic field. For higher densities, the conductivity raises to a maximum before the monotonous decrease. It has been conjectured in reference [54] that for higher densities, trajectories with a certain radius can traverse the Lorentz gas more

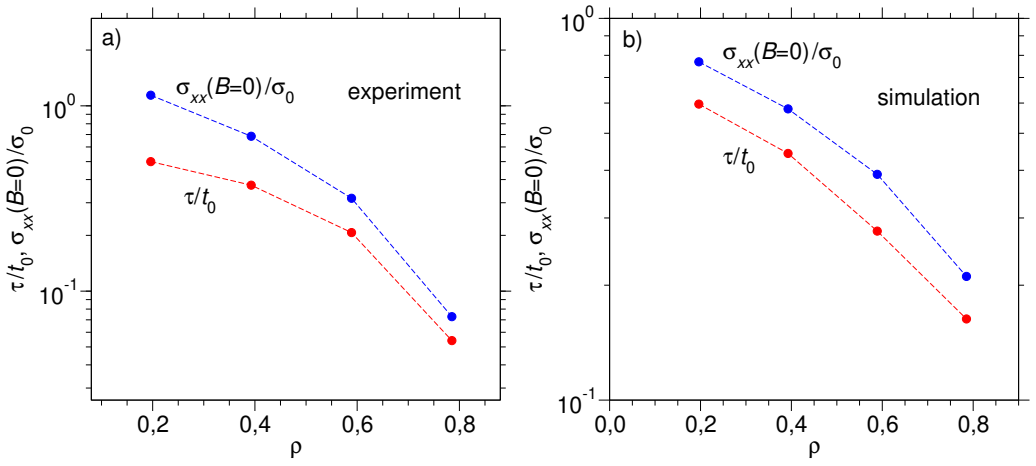

Figure 5.15 Reduced Drude time τ/t_0 and reduced conductivity $\sigma_{xx}(\tilde{B}=0)/\sigma_0$ as a function of ρ for a) the experiment and b) the simulation.

easily. Therefore, one observes a maximum of the conductivity at the corresponding magnetic field. At low magnetic fields ($\tilde{B} < 1.0$), the data shows a good agreement between simulation and experiment. As one can see in the experimental results, the conductivity decays slower than in the simulations. One also observes Shubnikov-de Haas oscillations [97]. These oscillations are due to the quantisation of the electron orbits into discrete Landau levels. In the classical case, the density of states of the electrons is independent of the magnetic field. Here, while the magnetic field is increased, the density of electron states available for transport varies leading to oscillations in the magnetoresistance. This is not captured by the simulations. For the highest density in the experiments ($\rho = 0.7853$), the experimental data shows a strange behaviour. These artefacts can be caused by obstacles obstructing the Ohmic contacts used for the measurements.

We can see in figure 5.14 that for sufficiently small magnetic fields, equation (5.27) describes the data fairly well for $\tilde{B}$ with $\omega_c\tau < 0.5$. The solid lines corresponds to the quantity $\omega_c\tau\sigma_{xx}$. Here, τ is a fit parameter used to obtain the best agreement between σ_{xy} and $\omega_c\tau\sigma_{xx}$. In figure 5.15, the reduced Drude time τ scaled with the mean free time $t_0 = \pi/(2r_{obs}\rho)$ and the reduced conductivity $\sigma_{xx}(B=0)/\sigma_0$ are shown as a function of the reduced density ρ. We see that τ/t_0 and $\sigma_{xx}(B=0)/\sigma_0$ decrease with ρ albeit the dependence of the reduced Drude time on ρ is stronger than that of the reduced conductivity. One can obtain the dependence of the magnetoresistance ρ_{xx} and the Hall resistance ρ_{xy} on $\tilde{B}$ by inserting equation (5.27) in

the respective formulas (3.20) and (3.21). One obtains

$$\rho_{xx} = \frac{1}{1+\omega_c^2\tau^2}\frac{1}{\sigma_{xx}}, \tag{5.28}$$

$$\rho_{xy} = \frac{\omega_c\tau}{1+\omega_c^2\tau^2}\frac{1}{\sigma_{xx}}. \tag{5.29}$$

For $B \to 0$, one has $\omega_c \to 0$, and equation (5.29) can be approximated by

$$\rho_{xy} \approx \frac{\omega_c\tau}{\sigma_{xx}(B=0)} = \frac{e\tau B}{m^\star\sigma_{xx}(B=0)} = R_H B, \tag{5.30}$$

where we have introduced the Hall coefficient

$$R_\mathrm{H} = \frac{e\tau}{m^\star\sigma_{xx}(B=0)}. \tag{5.31}$$

Figure 5.16 a) shows the magnetoresistance ρ_{xx} obtained from the experiment (solid lines). The dashed lines show the approximations calculated via equation (5.28). In figure 5.16 b), the same is shown for the simulations. As equation (5.27) holds up to values of $\tilde{B}$ with $\omega_c\tau \approx 0.5$, this is also valid for equations (5.28) and (5.29). For low magnetic fields $\tilde{B}$, the approximations of the magnetoresistance ρ_{xx} are in good agreement with the data. As τ decreases with increasing density ρ (figure 5.15), we see a better agreement between the actual data and the approximation of ρ_{xx} for higher magnetic fields at higher densities.

Figures 5.17 and 5.18 show the Hall resistance as obtained from the experiments and the simulations respectively. The solid lines represent the actual data. The dashed lines are the approximations calculated via equation (5.29). The black dotted lines show the linear approximation $\rho_{xy} = R_H B$ where the Hall coefficient is given by equation (5.31).

We see that these approximations are robust in the limit $\tilde{B} \to 0$ for high densities. As we can see in figure 5.15, the Drude time and the zero-field conductivity exhibit a similar dependence on the density. Recalling equation (3.5), one notes that the Drude time τ represents the time scale on which an electron dissipates the energy gained by the applied E and B-fields. With rising obstacle density, this time scale becomes smaller as in the dissipation happens though collisions with the obstacles. On the other hand, with rising density, the mobility of the electrons is impaired leading to a decrease of the conductivity. This density dependence of both quantities cancels out in equation (5.31) leading to a weaker dependence of R_H on the density. This explains the robustness of the prediction of R_H towards higher densities.

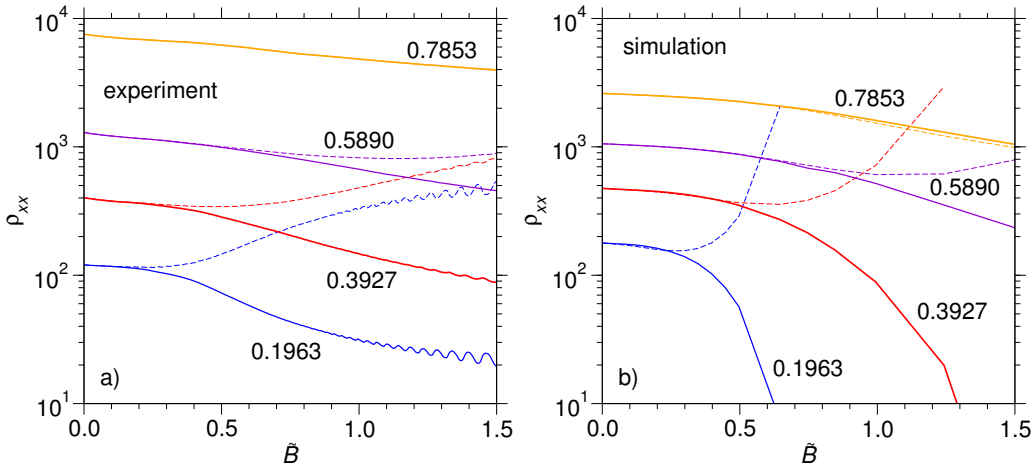

Figure 5.16 Magnetoresistance $\rho_{xx}(\tilde{B})$ at different densities, as obtained from a) the experiment and b) the simulation. The solid lines correspond to the data while the dashed lines are calculated via equation (5.28).

5.2.2 Magneto-transport in the Wind-tree Model

In contrast to the Lorentz gas with circular scatterers, the diffusion coefficient in the wind-tree model vanishes at all densities in the limit $B \to 0$. Thus we also expect that $\sigma_{xx}(B)$ vanishes in the limit $B \to 0$. Therefore, the behaviour of ρ_{xy} according to equation (5.31) cannot be upheld as the definition of the Hall coefficient involving $\sigma_{xx}(B = 0)$ is not well defined in the limit $B \to 0$. Therefore, we await a non-linear response of ρ_{xy} to small magnetic fields.

We have simulated three different densities $\rho = 0.1$, 0.2, and 0.3. The simulation box sizes were $L = 500$ for $\rho = 0.1$ and $\rho = 0.3$. For $\rho = 0.5$ we chose $L = 200$. For magnetic fields $B < 0.1$, the average was taken over 2×10^6 trajectories and 2×10^4 independent obstacles configurations. For lower magnetic fields ($B \leq 0.1$), the statistics of the Hall conductivity deteriorated rapidly and averages over more than 10^8 trajectories where needed to extract meaningful data.

Figure 5.19 a) shows the MSD at different magnetic fields plotted against the time. The orange line represents the MSD with no magnetic field. The MSDs with B-field follow exactly this "master" curve before deviating above a time scale $\tilde{\tau}$. This effect can be better seen in figure 5.19 b) where the derivative of the MSD with respect to time is shown. Due to the curvature of the tracer trajectories in the presence of a magnetic field, the retroreflection is destroyed for times larger than $\tilde{\tau}$ and the system becomes diffusive again in the long time limit. This leads to normal diffusion in the asymptotic limit.

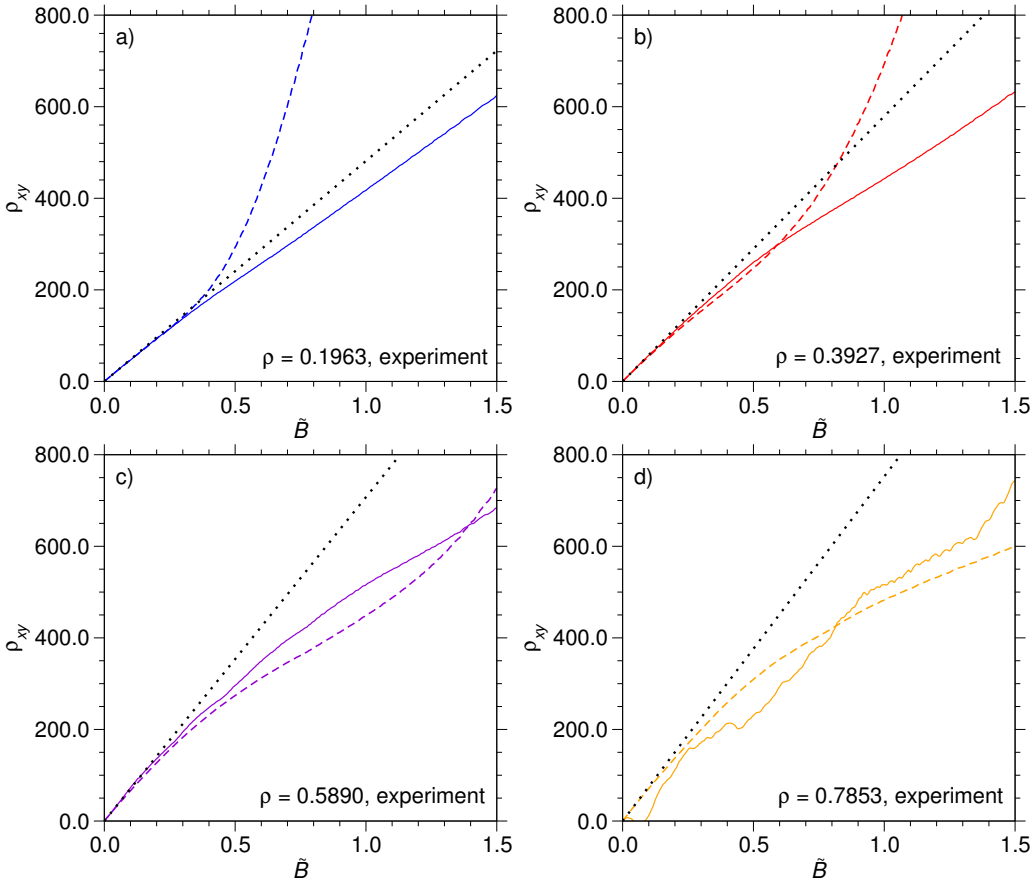

Figure 5.17 Hall resistance $\rho_{xy}(\tilde{B})$, as obtained from the experiment, at the densities a) $\rho = 0.1963$, b) $\rho = 0.3927$, c) $\rho = 0.5890$, and d) $\rho = 0.7853$. The blue solid lines represent the data, while the blue dashed lines are calculated via equation (5.29). The black dotted lines represent the expected behaviour at low magnetic fields, $\rho_{xy} = R_{\mathrm{H}}B$ with the Hall coefficient R_{H} given by equation (5.31).

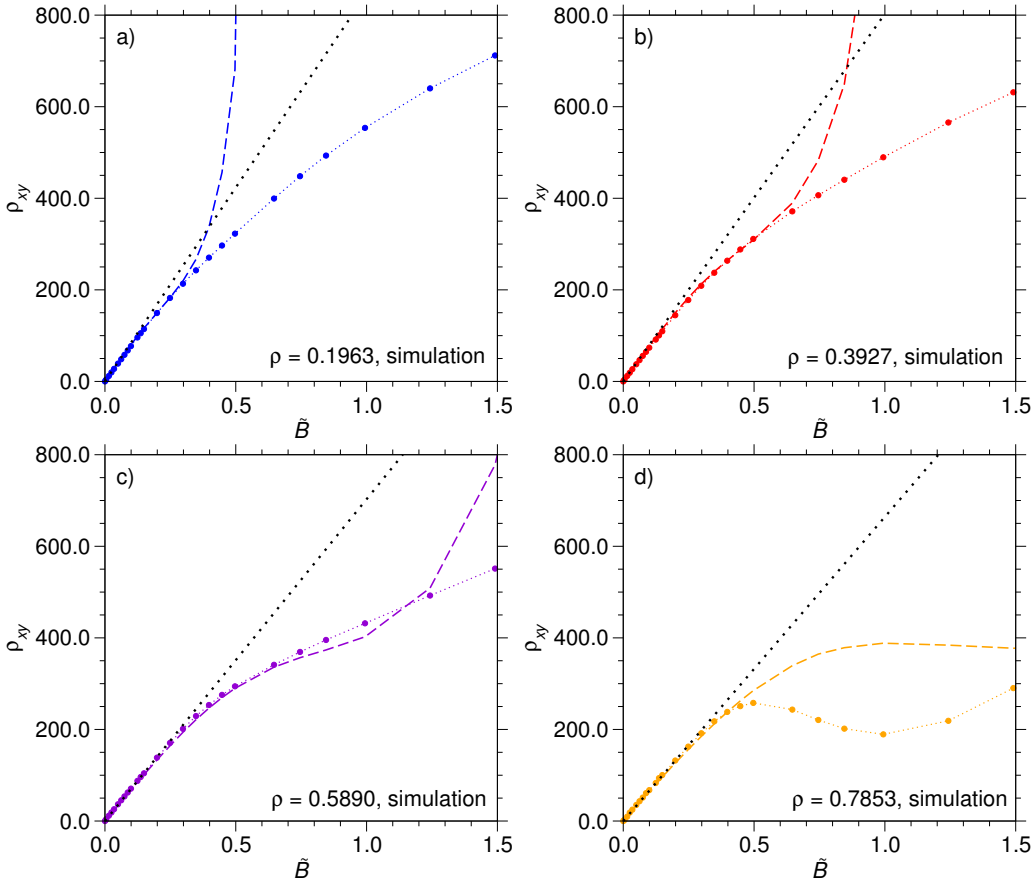

Figure 5.18 Hall resistance $\rho_{xy}(\tilde{B})$, as obtained from the simulations, at the densities a) $\rho = 0.1963$, b) $\rho = 0.3927$, c) $\rho = 0.5890$, and d) $\rho = 0.7853$. The blue solid lines represent the data, while the blue dashed lines are calculated via equation (5.29). The black dotted lines represent the expected behaviour at low magnetic fields, $\rho_{xy} = R_{\mathrm{H}}B$ with the Hall coefficient R_{H} given by equation (5.31).

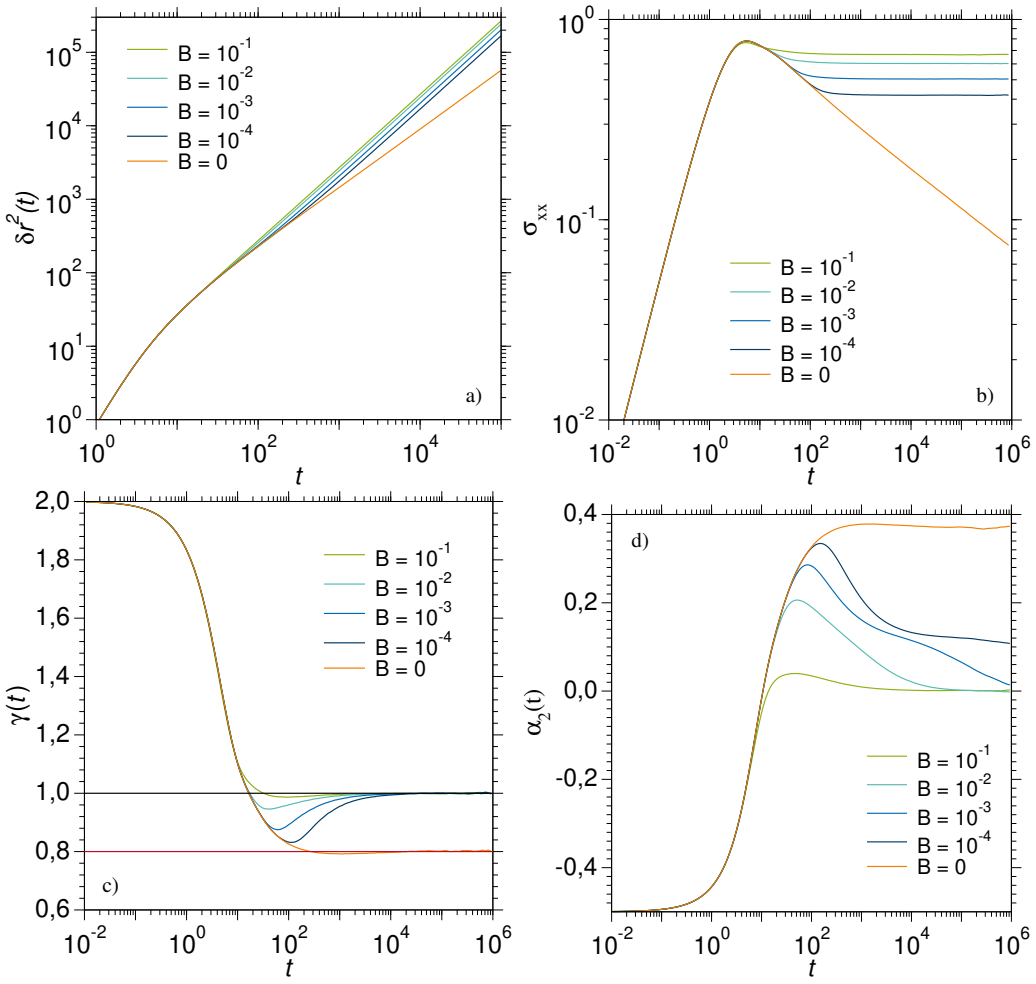

Figure 5.19 Simulation results for a system of oriented random overlapping squares at a density of $\rho = 0.3$. a) MSDs at five different magnetic fields $B = 0$, 10^{-1}, 10^{-2}, 10^{-3}, and 10^{-4}. b) Shows $\mathrm{d}\delta r^2(t)/\mathrm{d}t$ for the same magnetic fields. c) Exponents $\gamma(t)$ of the MSD. The red line shows the expected value in the wind-tree model. d) Non-Gaussian parameter $\alpha_2(t)$

We can already infer from figures 5.19 a) and 5.19 b) that $\tilde{\tau}$ increases if the magnetic field becomes smaller. This is expected as for weaker magnetic fields the curvature of the trajectory approaches zero and the retroreflection survives on longer timescales. Figure 5.19 c) shows the exponent of the MSD. In the case $B = 0$, we retrieve the asymptotic behaviour predicted by van Beyeren and Hauge [45] for the wind-tree model already treated in the previous section. For decreasing magnetic fields, a subdiffusive regime emerges at intermediate times. It is also associated with the retroreflection changing the dynamics of the particles at intermediate times scales. As we can see in figure 5.19 d), the non-Gaussian parameter is a more sensitive quantity with regard to anomalous diffusion. For small magnetic fields $B < 10^{-2}$, the non-Gaussian parameter α_2 shows that the dynamics of the tracer particles are yet not completely diffusive, although the exponent of the MSDs has already converged to one.

B	δ	δ/ρ
0.1	0.022	0.22
0.3	0.078	0.26
0.5	0.127	0.25

Table 5.1 Exponents δ of the magnetoductivity at low magnetic fields. The ratio δ/B seems to only weakly depend on the obstacle density

In figure 5.20 a) we show the magnetoconductivity σ_{xx} as a function of the magnetic field on a double logarithmic scale. For small magnetic fields ($B < 10^{-2}$) the data seems to exhibit a power law behaviour, i.e. $\sigma_{xx} \propto B^{-\delta}$ towards $B = 0$. Although data for much smaller magnetic field needs to be computed to get reliable data, we give an overview of the exponents extracted so far in table 5.1. It might be interesting to further investigate the relationship between δ and the reduced density. As we see in table 5.1, the quantity δ/ρ seems to only weakly depend on the obstacle density.

In figure 5.20 b) the Hall conductivity is shown. Here, we observe a negative Hall resistance for weak magnetic fields for the densities $\rho = 0.3$ and $\rho = 0.5$. Figure 5.21 a) shows the magnetoresistance ρ_{xx} as a function of the magnetic field. We observe a divergence for small magnetic fields as expected. Here also, a power law behaviour is observed with the same exponents as for σ_{xx} (but with a negative sign). In figure 5.21 b) we show the behaviour of the Hall resistance for small magnetic fields. For comparison we have added the data for the non-overlapping case at a density of $\rho = 0.1$, and for the overlapping case an additional density ($\rho = 0.05$) was also computed. We clearly see the linear response of the system with non-overlapping squares. In the overlapping case the Hall resistance is not linear as a function of the magnetic field. Looking at equation (5.31) we see that a σ_{xx} vanishes for $B = 0$, the Hall coefficient has a singularity at $B = 0$. This seems to be the origin of the non-linear behaviour or ρ_{xy} for $B \to 0$. The Hall resistance even becomes negative for higher densities. We have not found an explanation for this phenomenon yet.

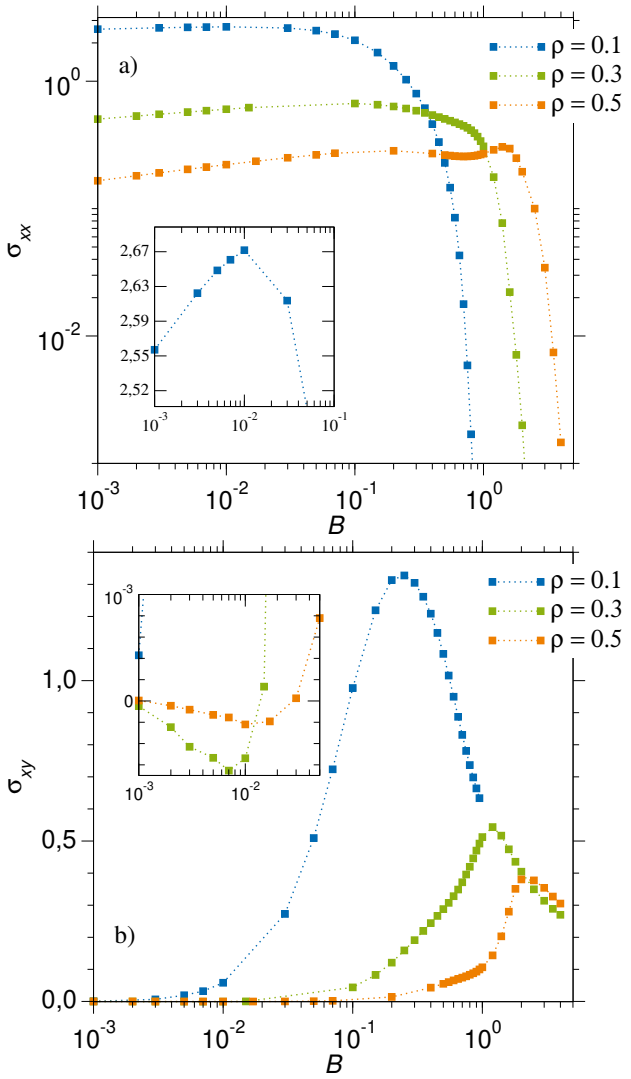

Figure 5.20 a) Magnetoconductivity $\sigma_{xx}(B)$ and b) Hall conductivity $\sigma_{xy}(B)$ at different densities, as obtained from the simulations. The inset in a) shows a magnification of the data for $\rho = 0.1$ to emphasize the decrease of σ_{xx} at low B-fields. The inset in b) shows the negative dip of ρ_{xx} for higher densities.

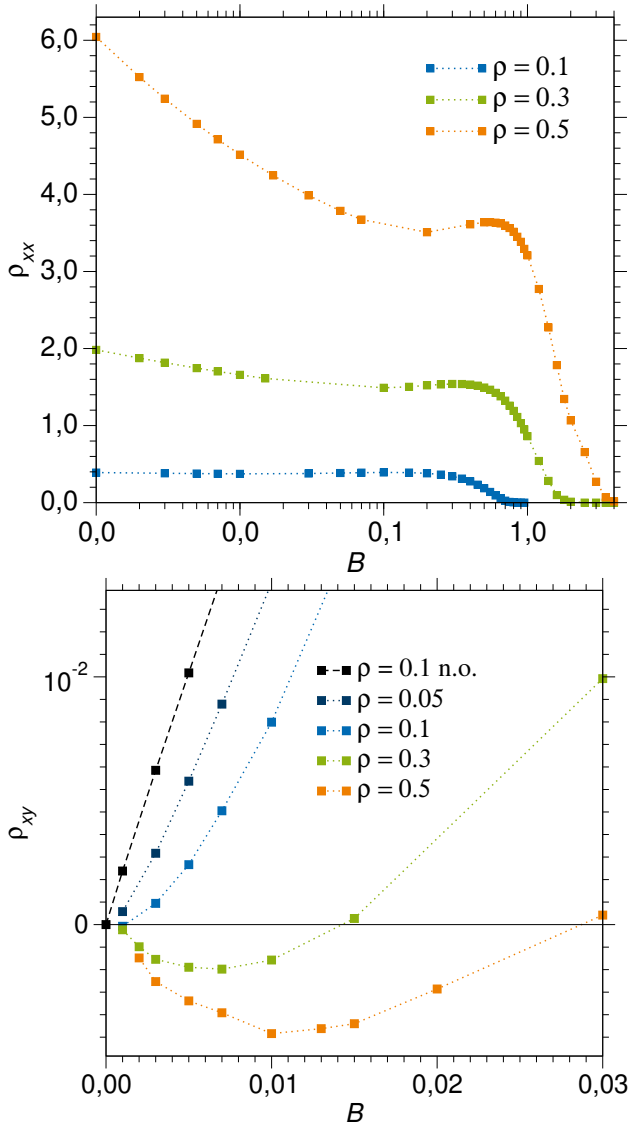

Figure 5.21 a) Magnetoresistance $\rho_{xx}(B)$ at different densities, as obtained from the experiment. b) Hall resistances at low B-fields. We clearly see the linear behaviour of ρ_{xy} in the case of non overlapping squares at low B-Fields (Black dashed line). Even for small densities the Hall resistance is not linear and eventually becomes negative for higher densities in the overlapping case.

5.2.3 Summary and Conclusions

We have presented a direct comparison between the experimental measurements on a 2DEG with circular scatterers and simulations of the system at the same densities. We have seen that the robustness of the prediction for the Hall coefficient in the Drude model is due to the cancellation of the density dependence in equation (5.31), leading to a weak density dependence of R_H. At higher densities and magnetic field the assumption of a constant Drude time cannot be upheld. Thus, the linear relation between ρ_{xy} and the magnetic field does not hold any more. This is shown in the experiments and also in the simulations. Furthermore we have investigated the magneto transport for random overlapping squares. In the case $B = 0$, we retrieve the wind-tree model investigated in the previous section. We found a non-linear Hall resistivity at low magnetic fields that becomes negative for sufficiently high densities.

5.3 Percolation Thresholds

It was conjectured by Schirmacher *et al.* [82] that the exponent of the MSD at the percolation threshold of the magnetic-field-induced percolation transition exhibits a different universal behaviour. Their findings where based on calculations of the Lorentz gas with circular scatterers. In this thesis we will investigate this transition for the EWTM with overlapping obstacles. Consequently we needed to compute the field-induced percolation threshold for different densities. We have therefore computed the phase diagram for the EWTM. In this section, we first present the results of the calculations of the static percolation threshold of the EWTM and then we will investigate the behaviour of the exponent of the MSD at the percolation thresholds for the EWTM compared to the Lorentz gas with circular scatterers.

5.3.1 Static Percolation Thresholds in the Lorentz Gas

To validate the code, we compute the percolation threshold for oriented squares and compare it with the results of Mertens *et al.* [55]. As explained in section 4.3, the probabilities densities $p_L^e(a, N)$ and $p_L^b(a, N)$ are computed first by randomly inserting obstacles in containers of different sizes. Then, the cumulative distributions $P_L^e(a, N)$ and $P_L^b(a, N)$ are derived from $p_L^e(a, N)$ and $p_L^b(a, N)$ respectively, by a simple cumulative sum. From those distributions, one now obtains the distributions $R_L^e(\rho)$ and $R_L^b(\rho)$ by convolution with the Poisson distribution with parameter $\lambda = \rho L^2/a$.

We chose 25 different container sizes ranging from $L = 30d_{obs}$ to $L = 1000d_{obs}$, where d_{obs} is the diameter of the smallest covering circle of the obstacle. In one "run" the obstacles are inserted until a wrapping cluster in the x- and y-direction has been detected. As the computation time on the cluster queues are limited, 10 trial runs are performed and the total wall time is measured. Then, the maximum number of runs that can be performed without trespassing the time limit on the queues is computed. This has the advantage that it allows to work on heterogeneous clusters that have nodes with different computational power without exceeding the time limit. The simulations where performed on the central HPC system "HILBERT" at the Heinrich-Heine University of Düsseldorf. The regular working queue of this cluster has time limit of 72 Hours. The total runtime was chosen smaller than this limit. 60 Hours of runtime where chosen as the individual runs vary in wall time, especially for the bigger containers sizes. Between $5 \cdot 10^9$ and $2 \cdot 10^8$ runs were performed for system sizes between $L = 30d_{obs}$ and $L = 100d_{obs}$. Approximately $5 \cdot 10^5$ runs were performed for a container size of $L = 10000d_{obs}$. Examples of the distributions $p_L(a, N)$ (defined in

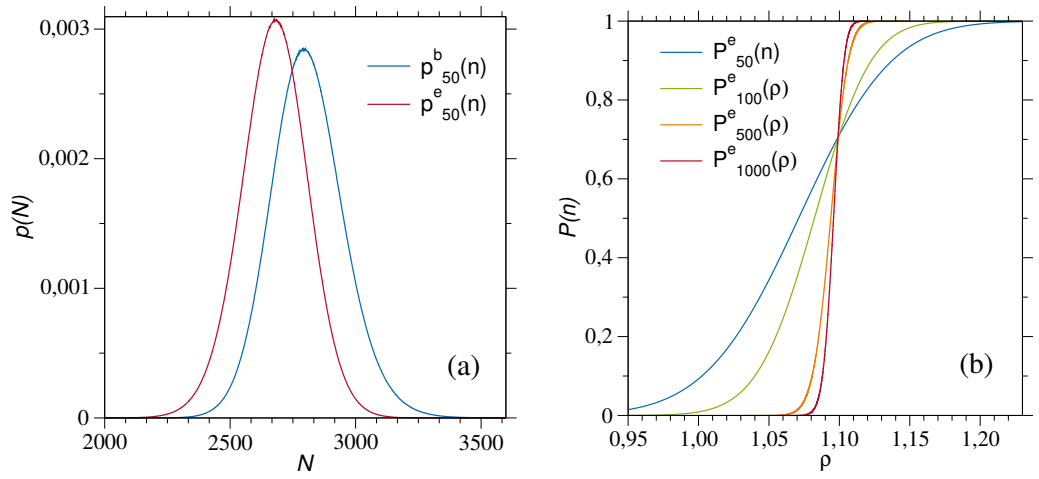

Figure 5.22 (a) Histograms directly recovered from the simulations: the curves represents the distributions of the number of obstacles at which a percolation cluster occurs. The red curve represents the distribution for a cluster occurring in the x or in the y-direction. The blue curve represents the distribution for the percolation cluster to occur in both directions. (b) Wrapping probabilities $P_L^e(a, N)$ for a cluster occurring in both directions for different container Length. The x-axis is rescaled by Na/L^2 and one can see the cross-over at R_∞^e

section 4.3) directly extracted from the simulations are shown in figure 5.22 a). An example of the distributions $P_L^e(a, N)$ is shown in figure 5.22 b).

Once the distributions $R_L^e(\rho)$ and $R_L^b(\rho)$ have been computed from $P_L^e(a, N)$ and $P_L^b(a, N)$, we used a simple Newton-Raphson method [98] to find the root of the functions $R_L^e(\rho) - R_\infty^e$ and $R_L^b(\rho) - R_\infty^b$. The roots are the critical filling factors ρ_L^e and ρ_L^b. As the function $R_L(\rho)$ becomes steep for large L, an initial guess for the Newton-Raphson method must be close to the root in order to ensure convergence. The initial guess can be derived from the abscissa at the maximum of $p_L(a, N)$ by dividing it by L^2/a. Recalling the finite size scaling relation (3.78), the values ρ_L^e and ρ_L^b must lie on a straight line if plotted against $L^{-11/4}$. Figure 5.23 shows the results of ρ_L^e and ρ_L^b plotted against $L^{-11/4}$. As one can see in figure 5.23, the data points for large L are more scattered and therefore have a larger variance. To obtain better results, the data points are fitted using a weighted linear regression [55]. This has the advantage that data points with a higher variance are incorporated with lighter weights. The errors used as weights are derived as [55]:

$$\sigma_{\rho_L} = \frac{1}{N^{1/2} L^{3/4}}. \tag{5.32}$$

One obtains two values ρ_c^e and ρ_c^b by extrapolating the fitted lines to zero.

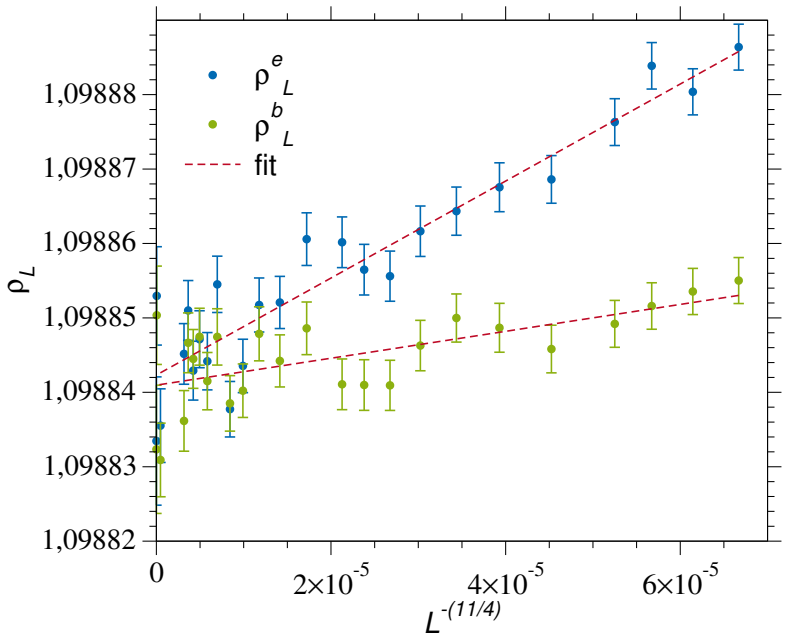

Figure 5.23 ρ_L^e and ρ_L^b plotted against $L^{-11/4}$. The dashed red lines show the results from the weighted linear regression.

The final result is obtained by taking the average between the two values. We have obtained a value of

$$\begin{aligned}\rho_c^{\square} &= 1.09884164 \pm 9.64 \cdot 10^{-7} \\ &= 1.09884(1)\end{aligned}$$

in good agreement with the value $\rho_c^{\square} = 1.09884280(9)$ computed by Mertens *et al.* considering the relative short simulation time.

With the validated code, the phase diagram for the EWTM in the presence of a magnetic field was computed. We have taken 45 values of the magnetic field between $B = 0.01$ and $B_c = 10000$. A table with all the computed values can be found in the appendix. Figure 5.24 shows the percolation thresholds for the EWTM in the presence of a magnetic field. The inset shows the phase diagram with linear scales. The orange curve shows the critical magnetic field of the field-induced percolation transition as a function of the reduced density. The red line represents the percolation transition at $\rho_c = 1.09884280(9)$ [55]. The green line at $B = 0$ represents the EWTM, therefore on the complete x-axis where $\rho \leq \rho_c$, one has anomalous diffusion. The red and orange lines do never touch, as for any density $\rho < \rho_c$ there exists a magnetic field B_c where the tracer particles are localized around isolated clusters for $B > B_c$. An interesting point is the intersection of the blue

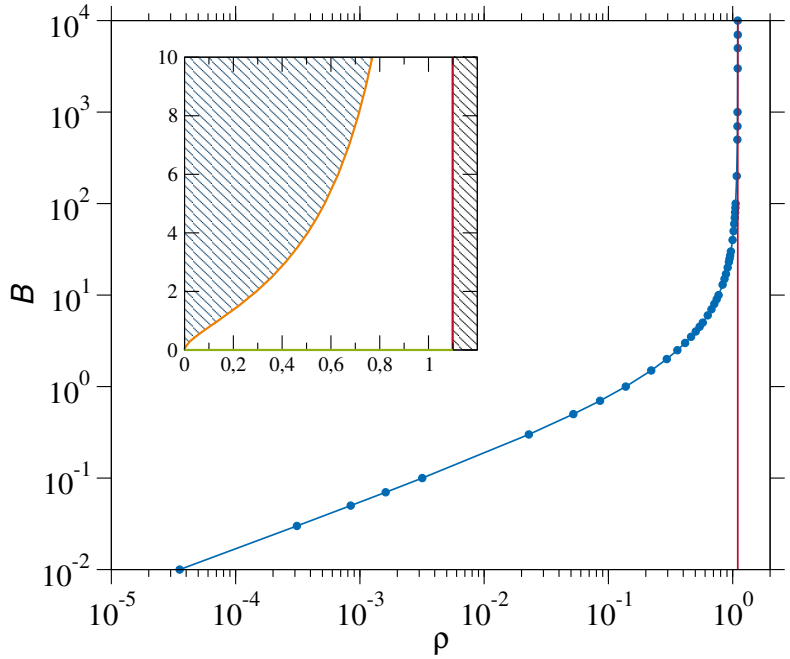

Figure 5.24 Phase diagram for Lorentz gas with randomly distributed oriented and overlapping square obstacles. The red line shows the percolation threshold as computed in [55]. The inset shows the phase diagram with a linear x-axis. The orange line represents the field-induced percolation threshold. The green line shows the limiting case of $B = 0$ where the transport properties are that of the wind-tree model. In the hatched area, the particles become localized.

and red line. Here, we are faced with anomalous diffusion due to two overlapping phenomena. Firstly the diffusion is anomalous due to the retroreflection in the EWTM, and secondly we are faced with anomalous diffusion at the percolation threshold.

5.3.2 Universal Exponents at the Percolation Threshold

Now that the percolation thresholds for the wind-tree model have been computed we can extract the critical exponents z and μ (see equations (3.76) and (3.77)) and compare them with the known results for the Lorentz gas with circular scatterers. We have used a system size of $L = 10^4 d_0$ at a density of $\rho = 0.1$ where $d_0 = 1$ corresponds to the diameter of the circular obstacles and the side length of the square obstacles. This corresponds roughly to 12.8×10^6 circular obstacles and 10^7 square obstacles. For higher densities, i.e. $\rho = 0.8$ and at the percolation threshold $\rho = \rho_c$, the same number of obstacles was used and the size of the container rescaled accordingly.

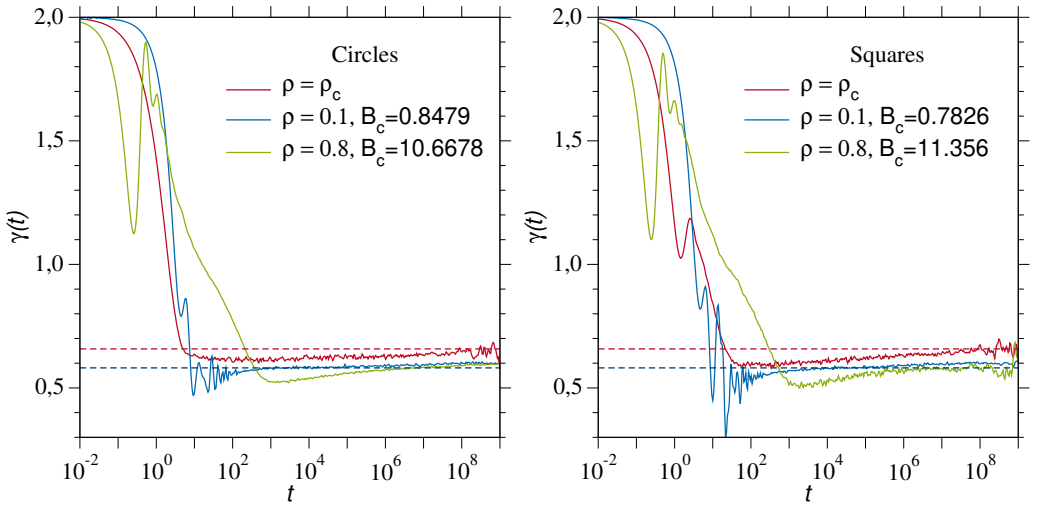

Figure 5.25 Exponents of the MSD for circles (left panel) and squares (right panel) at different percolation thresholds (see text).

Figure 5.25 shows the exponents $\gamma(t)$ as a function of time for circular and square obstacles. The red curve corresponds to the exponent $\gamma(t)$ for both systems at the percolation threshold ρ_c as computed by Mertens *et al.* [55]. The red dashed line shows the expected asymptotic exponent $\gamma = 0.658$ [55]. The blue curve shows $\gamma(t)$ at the field-induced percolation threshold at $\rho_c = 0.1$, with $B_c = 0.8479$ obtained from the formula given by Kuzmany and Spohn [54]. For the square obstacles at $\rho = 0.1$ we have derived the value of $B_c = 0.7826$ from the phase diagram computed previously. The value was obtained by cubic interpolation of the data points listed in table A.1. The blue curve shows $\gamma(t)$ at a density of $\rho = 0.8$ corresponding to $B_c = 10.6678$ for the circular obstacles and $B_c = 11.356$ for the square obstacles. Here, B_c was also obtained from the phase diagram as already explained. The black dashed line shows the exponent γ at the B-field-induced transition as computed in [82].

We can confirm and extend the results of Schirmacher *et al.* [82]: The exponents γ_B of the B-field-induced transition seem to be independent of the magnetic field. As one can see in figure 5.25, at high magnetic fields, a shoulder emerges in the plots of $\gamma(t)$. This is due to a change in the dynamics of the particles: at high magnetic fields the particles start to move along the edges of the obstacles in skipping orbits. On that time scale, the tracer particles exhibit a superdiffusive transport regime $\gamma > 1$. On longer timescales the transport becomes subdiffusive again. Also, we see that the exponents of the MSD at the B-field-induced percolation transition seem to differ from those at the high density percolation transition. While the exponents of the

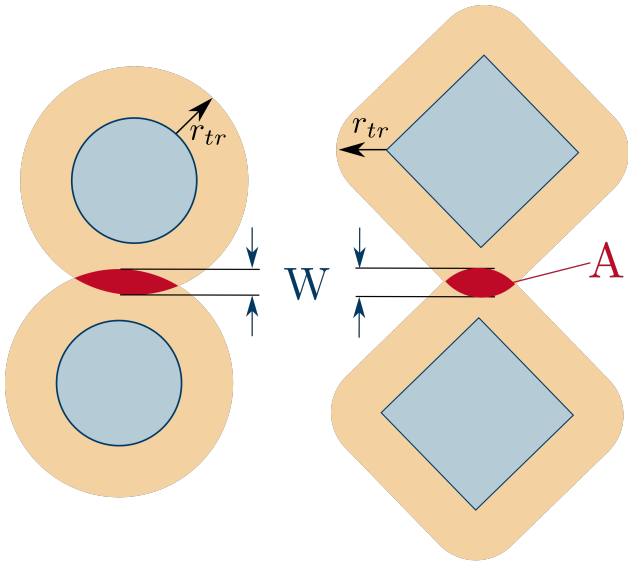

Figure 5.26 Visualisation of the weak-link scenario of the B-field-induced percolation transition for circles (left) and squares (right). If the yellow regions overlap (red), then a tracer particle can jump from obstacle to obstacle. The red areas represent the surface A where the two obstacles are closer as $2 \times r_{tr}$. For vanishing width W, this area scales with $A \sim W^{3/2}$.

MSD for the static percolation threshold converge to $\gamma = 2/z = 0.656$, where the universal exponent $z = 3.0455$ is given by equation (3.76), we have obtained a value of $\gamma = 2/z = 0.595$. This corresponds to a value of $z = 3.36$ close to the value of $z = 3.44$ obtained in [82]. This difference between the exponents at the two percolation thresholds was attributed to the fact that at the field-induced percolation threshold, the diffusion is dominated by weak links. These weak links correspond to obstacles just close enough for a tracer particle to jump between them (see figure 5.26). It was shown that percolation transitions dominated by the presence of weak links do not exhibit universal behaviour [99]. Schirmacher *et al.* [82] have identified the area of the red surfaces A (see figure 5.26) as transition rates of these weak links. They showed that while approaching the percolation threshold, A vanishes as $A \sim W^{3/2}$ where W corresponds to the width of the area A, leading to an exponent $z = 3.18$ according to the results in references [99] and [100]. This is closer to the observed value but still not satisfactory. In the scenario of the EWTM we have the same behaviour of the weak links. As one can see in figure 5.26, the shape of the area A is identical for circles and for squares, and therefore we await the same behaviour as W vanishes. But still, the predicted values are not in perfect agreement with the simulation results and

we consider the explanation of this discrepancy to be still an open question.

5.3.3 Summary and Conclusions

We have computed the phase diagram for the EWTM in the presence of a magnetic field. The method used can easily be applied to any geometry. Furthermore we have confirmed the findings of Schirmacher *et al.* [82] also for the EWTM: The dynamic exponent z of the MSD at the field-induced percolation transition does not depend on the magnetic field. Secondly, at both transitions, the MSD exhibits different exponents. At the high density percolation threshold , the exponents are in good agreement with the known universal values. At the B-field-induced transition, the behaviour seems to be correspond to another universality class. Although it was conjectured by Schirmacher *et al.* that this difference is due to the presence of weak links that dominate the transport at the percolation threshold, there is still a discrepancy between the predicted exponents and the simulation data.

6 Conclusion and Outlook

In this thesis, various aspects of transport phenomena in Lorentz gases were investigated.

Ehrenfests' Wind-Tree Model (EWTM) The EWTM serves as a model system for testing kinetic theories in the low density limit. In comparison to the Lorentz gas with circular scatterers, the density expansion up to the second order is better behaved. In the case of circular obstacles, terms involving collisions with two obstacle diverge as $\log(\rho)$ in the limit $\rho \to 0$. This is not the case in the EWTM due to the discrete velocity space. The calculations of Hauge and Cohen [1, 43] can be considered as a "tour de force", but their prediction of the asymptotic behaviour of the EWTM with overlapping obstacles seems to be erroneous. We could confirm the density-dependent exponent of the MSD as proposed by van Beyeren and Hauge. Such a dependence for the asymptotic exponent describing subdiffusion is unique and, to the best of our knowledge, no other model system with such behaviour is known. It would be interesting to investigate other geometries with a restricted velocity space like crosses, or octagons in that regard. Further investigations should also be carried out towards the percolation transition in the overlapping EWTM as it is a rare, if not the only example of the overlap of two different processes causing anomalous diffusion.

Magnetotransport We could explain the robustness of the prediction of the Hall coefficient in the Drude model even at higher densities. This is due to the weak dependence of R_H on density. We also investigated the EWTM at low magnetic fields. In the limit of low fields, the diffusion coefficient vanishes, therefore the Hall coefficient $R_H = e\tau/(m^\star \sigma_{xx}(B = 0))$ diverges for $B = 0$. We have observed a non-linear response of the magnetoresistance at low magnetic fields. We have even observed a negative Hall resistance

pointing to a reversal of the Hall current at low densities. Further investigations to find an explanation of this phenomenon are needed. Especially the behaviour of other geometries exhibiting anomalous diffusion in the limit $B = 0$ [29] would need to be investigated in that regard.

Percolation It is still not clear why the the exponents of the field-induced percolation transition differ from the universal exponents of the percolation transition at high densities. This was associated with the non universal behaviour of resistor networks in the presence of weak links. Still, no satisfying theory exists for the observed phenomenology in Lorentz gases. We have devised a method to compute the magnetic-field-induced percolation transition, but this method can be applied to compute the low-density percolation transition for any system where the maximal extent of the tracer particle from the obstacles is restricted. It might therefore be interesting to construct such a system with non-physical trajectories where the weak links vanish with another exponent than in the case of circular trajectories. This might settle the question whether the different behaviour at both transitions is due to the weak links.

A Percolation Thresholds

A.1 Percolation Thresholds for Crosses

Percolation thresholds for the crosses used in the experiments of reference [29]. The dimensions of the crosses are given in the sketch on the right.

Percolation threshold for oriented crosses:

$$\rho^+ = 0.776645(9). \tag{A.1}$$

Percolation threshold for non-oriented crosses:

$$\rho^+ = 0.69767(4). \tag{A.2}$$

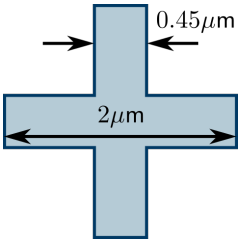

A.1.1 Thresholds for the Magnetic-field-induced Percolation Transition

The magnetic-field-induced percolation thresholds in the EWTM used to compute the phase diagram in figure 5.24 are given in table A.1 on the next page.

Table A.1 Percolation thresholds for the magnetic-field-induced percolation transition.

B	$\tilde{\rho}_c$	B	$\tilde{\rho}_c$
0.01	$3.54555(9) \cdot 10^{-}5$	15.0	0.85923(6)
0.03	0.00031119(4)	17.0	0.88277(1)
0.05	0.00084332(2)	20.0	0.91052(9)
0.07	0.0016131(3)	23.0	0.93196(6)
0.1	0.0031760(0)	25.0	0.94373(8)
0.3	0.022893(1)	27.0	0.95396(0)
0.5	0.052212(8)	30.0	0.96699(6)
0.7	0.085678(3)	40.0	0.99741(4)
1.0	0.13784(3)	50.0	1.01643(0)
1.5	0.22094(4)	60.0	1.02944(3)
2.0	0.29470(3)	70.0	1.03890(5)
2.5	0.35875(1)	80.0	1.04609(8)
3.0	0.41420(8)	90.0	1.05174(9)
3.5	0.46239(8)	100.0	1.05630(7)
4.0	0.50452(0)	200.0	1.07722(5)
4.5	0.54157(6)	500.0	1.09010(8)
5.0	0.57438(6)	700.0	1.09259(1)
6.0	0.62980(5)	1000.0	1.09445(9)
7.0	0.67475(3)	3000.0	1.09737(8)
8.0	0.71190(1)	5000.0	1.09796(1)
9.0	0.74310(1)	7000.0	1.09821(3)
10.0	0.76966(4)	10000.0	1.09840(0)
13.0	0.82995(8)		
15.0	0.85923(6)		

Bibliography

[1] E. H. Hauge and E. G. D. Cohen, *Divergences in non-equilibrium statistical mechanics and Ehrenfest's wind-tree model*, Arkiv for Det Fysiske Seminar i Trondheim **7** (1968).

[2] E. H. Hauge, *What can one learn from Lorentz models?*, in *Lecture notes in physics* (Springer, Berlin, 1974), p. 337.

[3] J. Kurzidim, D. Coslovich, and G. Kahl, *Single-particle and collective slow dynamics of colloids in porous confinement*, Phys. Rev. Lett. **103**, 138303 (2009).

[4] J. Kurzidim, D. Coslovich, and G. Kahl, *Impact of random obstacles on the dynamics of a dense colloidal fluid*, Phys. Rev. E **82**, 041505 (2010).

[5] J. Kurzidim, D. Coslovich, and G. Kahl, *Dynamic arrest of colloids in porous environments: disentangling crowding and confinement*, J. Phys.: Condens. Matter **23**, 234122 (2011).

[6] T. O. E. Skinner, S. K. Schnyder, D. G. A. L. Aarts, J. Horbach, and R. P. A. Dullens, *Localization dynamics of fluids in random confinement*, Phys. Rev. Lett. **111**, 128301 (2013).

[7] F. Evers, R. D. L. Hanes, C. Zunke, R. F. Capellmann, J. Bewerunge, C. Dalle-Ferrier, M. C. Jenkins, I. Ladadwa, A. Heuer, R. Castañeda-Priego, and S. U. Egelhaaf, *Colloids in light fields: particle dynamics in random and periodic energy landscapes*, Eur. Phys. J. Spec. Top. **222**, 2995 (2013).

[8] J. Bewerunge, I. Ladadwa, F. Platten, C. Zunke, A. Heuer, and S. U. Egelhaaf, *Time- and ensemble-averages in evolving systems: the case of brownian particles in random potentials*, Phys. Chem. Chem. Phys. **18**, 18887 (2016).

[9] L. Ning, P. Liu, F. Ye, M. Yang, and K. Chen, *Diffusion of colloidal particles in model porous media*, Phys. Rev. E **103**, 022608 (2021).

[10] S. K. Schnyder, T. O. E. Skinner, A. L. Thorneywork, D. G. A. L. Aarts, J. Horbach, and R. P. A. Dullens, *Dynamic heterogeneities and non-gaussian behavior in two-dimensional randomly confined colloidal fluids*, Phys. Rev. E **95**, 032602 (2017).

[11] S. G. Anekal, Y. Zhu, M. D. Graham, and J. Yin, *Dynamics of virus spread in the presence of fluid flow*, Integr. Biol. **1**, 664 (2009).

[12] F. Höfling and T. Franosch, *Anomalous transport in the crowded world of biological cells*, Rep. Prog. Phys. **76**, 046602 (2013).

[13] Y. Yura, H. Takayasu, D. Sornette, and M. Takayasu, *Financial brownian particle in the layered order-book fluid and fluctuation-dissipation relations*, Phys. Rev. Lett. **112**, 098703 (2014).

[14] K. Kanazawa, T. Sueshige, H. Takayasu, and M. Takayasu, *Kinetic theory for financial Brownian motion from microscopic dynamics*, Phys. Rev. E **98**, 25 (2018).

[15] S. Cordier, L. Pareschi, and G. Toscani, *On a kinetic model for a simple market economy*, J. Stat. Phys. **120**, 253 (2005).

[16] S. Cordier, L. Pareschi, and C. Piatecki, *Mesoscopic modelling of financial markets*, J. Stat. Phys. **134**, 161 (2009).

[17] L. Boltzmann, *Über die Anzahl der Atome in den Gasmolekülen und die innere Arbeit in Gasen*, in *Wissenschaftliche Abhandlungen* (Cambridge University Press, 1867), p. 34.

[18] L. Boltzmann, *Ueber die Unentbehrlichkeit der Atomistik in der Naturwissenschaft*, Ann. Phys. **296**, 231 (1897).

[19] L. Boltzmann, *Nochmals über die Atomistik*, Ann. Phys. **297**, 790 (1897).

[20] A. Einstein, *Über die von der molekularkinetischen Theorie der Wärme geforderte Bewegung von in ruhenden Flüssigkeiten suspendierten Teilchen*, Ann. Phys. **322**, 549 (1905).

[21] R. Brown, *A brief account of microscopical observations made in the months of june, july and august 1827, on the particles contained in the pollen of plants and on the general existence of active molecules in organic and inorganic bodies*, Philos. Mag. **4**, 161 (1828).

[22] H. Fischer, *A history of the central limit theorem* (Springer, New York, 2011).

[23] I. Bronstein, Y. Israel, E. Kepten, S. Mai, Y. Shav-Tal, E. Barkai, and Y. Garini, *Transient anomalous diffusion of telomeres in the nucleus of mammalian cells*, Phys. Rev. Lett. **103**, 018102 (2009).

[24] M. J. Saxton, *A biological interpretation of transient anomalous subdiffusion. I. Qualitative model*, Biophysical Journal **92**, 1178 (2007).

[25] W. W. Wood and F. Lado, *Monte carlo calculation of normal and abnormal diffusion in Ehrenfest's wind-tree model*, J. Comput. Phys. **7**, 528 (1971).

[26] S. Schnyder, *Anomalous transport in heterogeneous media*, PhD thesis (Heinrich-Heine Universität, Düsseldorf, 2014).

[27] J. Horbach, N. H. Siboni, and S. K. Schnyder, *Anomalous transport in heterogeneous media*, Eur. Phys. J. Spec. Top. **226**, 3113 (2017).

[28] R. Lohmann, *Magnetotransport in retroreflective Lorentz gases*, MA thesis (Heinrich-Heine Universität Düsseldorf, Düsseldorf, 2019).

[29] R. Lohmann, B. Horn-Cosfeld, J. Schluck, D. Mailly, N. H. Siboni, H. W. Schumacher, K. Pierz, T. Heinzel, and J. Horbach, *Anomalous transport due to retroreflection*, Phys. Rev. B **102**, 081302 (2020).

[30] N. Siboni, J. Schluck, K. Pierz, H. Schumacher, D. Kazazis, J. Horbach, and T. Heinzel, *Nonmonotonic classical magnetoconductivity of a two-dimensional electron gas in a disordered array of obstacles*, Phys. Rev. Lett. **120**, 056601 (2018).

[31] J. Schluck, M. Hund, T. Heckenthaler, T. Heinzel, N. H. Siboni, J. Horbach, K. Pierz, H. W. Schumacher, D. Kazazis, U. Gennser, and D. Mailly, *Linear negative magnetoresistance in two-dimensional Lorentz gases*, Phys. Rev. B **97**, 115301 (2018).

[32] B. Horn-Cosfeld, J. Schluck, J. Lammert, M. Cerchez, T. Heinzel, K. Pierz, H. Schumacher, and D. Mailly, *Relevance of weak and strong classical scattering for the giant negative magnetoresistance in two-dimensional electron gases*, Phys. Rev. B **104**, 045306 (2021).

[33] B. Horn-Cosfeld, J. Schluck, J. Lammert, M. Cerchez, T. Heinzel, K. Pierz, H. W. Schumacher, and D. Mailly, *Relevance of weak and strong classical scattering for the giant negative magnetoresistance in two-dimensional electron gases*, Phys. Rev. B **104**, 045306 (2021).

[34] H. A. Lorentz, *The motion of electrons in metallic bodies*, Proc. K. Ned. Akad. Wet. **7**, 438 (1905).

[35] H. van Beijeren, *Transport properties of stochastic Lorentz models*, Rev. Mod. Phys. **54**, 195 (1982).

[36] J. van Leeuwen and A. Weijland, *Non-analytic density behaviour of the diffusion coefficient of a Lorentz gas I. Divergencies in the expansion in powers in the density*, Physica **36**, 457 (1967).

[37] J. van Leeuwen and A. Weijland, *Non-analytic density behaviour of the diffusion coefficient of a Lorentz gas*, Physica **38**, 35 (1968).

[38] C. P. Dettmann, *Diffusion in the Lorentz gas*, Commun. Theor. Phys. **62**, 521 (2014).

[39] S. K. Schnyder, M. Spanner, F. Höfling, T. Franosch, and J. Horbach, *Rounding of the localization transition in model porous media*, Soft Matter **11**, 701 (2015).

[40] G. Gallavotti, *Rigorous theory of the Boltzmann equation in the Lorentz gas*, Nota interna n. 358, Istituto di Fisica G. Marconi, Universitá di Roma (1972).

[41] H. Grad, *Principles of the kinetic theory of gases*, in, Encyclopedia of Physics (Springer, Berlin, 1958), p. 205.

[42] P. Ehrenfest and T. Ehrenfest, *Begriffliche Grundlagen der statistischen Auffassung in der Mechanik*, in *Encykl. Math. Wissenschaften* (Springer, Wiesbaden, 1907), p. 773.

[43] E. H. Hauge and E. G. D. Cohen, *Normal and abnormal diffusion in Ehrenfest's wind-tree model*, Phys. Lett. A **25**, 78 (1967).

[44] E. H. Hauge and E. G. D. Cohen, *Normal and abnormal diffusion in Ehrenfests' wind-tree model*, J. Math. Phys. **10**, 397 (1969).

[45] H. Van Beyeren and E. H. Hauge, *Abnormal diffusion in Ehrenfest's wind-tree model*, Phys. Lett. A **39**, 397 (1972).

[46] E. Hall, *XVIII. On the "rotational coefficient" in nickel and cobalt*, Lond. Edinb. Dubl. Phil. Mag **12**, 157 (1881).

[47] A. V. Bobylev, F. A. Maaø, A. Hansen, and E. H. Hauge, *There is more to be learned from the Lorentz model*, J. Stat. Phys. **87**, 1205 (1997).

[48] A. V. Bobylev, F. A. Maaø, A. Hansen, and E. H. Hauge, *Two-dimensional magnetotransport according to the classical Lorentz model*, Phys. Rev. Lett. **75**, 197 (1995).

[49] A. V. Bobylev, A. Hansen, J. Piasecki, and E. H. Hauge, *From the Liouville equation to the generalized Boltzmann equation for magnetotransport in the 2d Lorentz model*, J. Stat. Phys. **102**, 1133 (2001).

[50] W. Götze and E. Leutheußer, *Magneto-transport in the two dimensional Lorentz model*, Z. Phys. B: Condens. Matter **45**, 85 (1981).

[51] A. Dmitriev and V. Y. Kachorovskii, *Magnetotransport in a 2d system with strong scatterers: renormalization of Hall coefficient caused by non-Markovian effects*, Semiconductors **42**, 934 (2008).

[52] V. V. Cheianov, A. Dmitriev, and V. Y. Kachorovskii, *Non-Markovian effects on the two-dimensional magnetotransport: low-field anomaly in magnetoresistance*, Phys. Rev. B **70**, 245307 (2004).

[53] A. Nota, C. Saffirio, and S. Simonella, *Two-dimensional Lorentz process for magnetotransport: Boltzmann-Grad limit*, in Annales de l'institut Henri poincaré, probabilités et statistiques, Vol. 58 (Institut Henri Poincaré, Paris, 2022), p. 1228.

[54] A. Kuzmany and H. Spohn, *Magnetotransport in the two-dimensional Lorentz gas*, Phys. Rev. E **57**, 5544 (1998).

[55] S. Mertens and C. Moore, *Continuum percolation thresholds in two dimensions*, Phys. Rev. E **86**, 061109 (2012).

[56] R. W. Zwanzig, *Nonequilibrium statistical mechanics* (Oxford University Press, New York, 2001).

[57] L. Van Hove, *Correlations in space and time and Born approximation scattering in systems of interacting particles*, Phys. Rev. **95**, 249 (1954).

[58] A. Rahman, *Correlations in the motion of atoms in liquid argon*, Phys. Rev. **136**, A405 (1964).

[59] T. Heinzel, *Mesoscopic electronics in solid state nanostructures* (Wiley-VCH Verlag, Weinheim, 2010).

[60] J. Schluck, *Classical electron magnetotransport in controlled potential landscapes*, PhD thesis (Heinrich Heine Universität Düsseldorf, Düsseldorf, 2018).

[61] K. Ploog, *Molecular beam epitaxy of III-V compounds: technology and growth process*, Annu. Rev. Mater. Sci. **11**, 171 (1981).

[62] R. Dingle, H. L. Störmer, A. C. Gossard, and W. Wiegmann, *Electron mobilities in modulation-doped semiconductor heterojunction superlattices*, Appl. Phys. Lett. **33**, 665 (1978).

[63] P. Drude, *Zur Elektronentheorie der Metalle*, Ann. Phys. **306**, 566 (1900).

[64] E. Rutherford, *The scattering of α and β particles by matter and the structure of the atom*, London Edinburgh Philos. Mag. J. Sci. **21**, 669 (1911).

[65] W. Kaiser, *Early theories of the electron gas*, Hist. Stud. Nat. Sci. **17**, 271 (1987).

[66] N. W. Ashcroft and N. D. Mermin, *Solid State Physics* (Saunders College Publishing, Philadelphia, 1976).

[67] R. Kubo, *Statistical-mechanical theory of irreversible processes. I. General theory and simple applications to magnetic and conduction problems*, J. Phys. Soc. Japan **12**, 570 (1957).

[68] P. Dirac, *On the theory of quantum mechanics*, Proc. R. Soc. Lond. A **112**, 661 (1926).

[69] J. R. Dorfman, H. van Beijeren, and T. R. Kirkpatrick, *Contemporary kinetic theory of matter* (Cambridge University Press, Cambridge, 2021).

[70] H. Spohn, *Large scale dynamics of interacting particles* (Springer, Berlin, 1991).

[71] C. Cercignani, *On the Boltzmann equation for rigid spheres*, Transp. Theory. Stat. Phys. **2**, 211 (1972).

[72] N. N. Bogoliubov and G. E. Uhlenbeck, *Problems of a dynamical theory in statistical physics*, in (North Holland Publishing Co, Amsterdam, Holland, 1962).

[73] J. R. Dorfman and E. G. D. Cohen, *On the density expansion of the pair distribution function for a dense gas not in equilibrium*, Phys. Lett. **16**, 124 (1965).

[74] R. Peierls, *Surprises in theoretical physics*, Princeton Series in Physics (Princeton University Press, Princeton, NJ, 1979).

[75] K. Kawasaki and I. Oppenheim, *Logarithmic term in the density expansion of transport coefficients*, Phys. Rev. **139**, A1763 (1965).

[76] R. Zwanzig, *Method for finding the density expansion of transport coefficients of gases*, Phys. Rev. **129**, 486 (1963).

[77] D. Stauffer and A. Aharony, *Introduction to percolation theory* (Taylor & Francis, London, 1994).

[78] P. Grassberger, *Conductivity exponent and backbone dimension in 2-d percolation*, Physica A **262**, 251 (1999).

[79] D. ben-Avraham and S. Havlin, *Diffusion and reactions in fractals and disordered systems* (Cambridge University Press, Cambridge, 2000).

[80] H. T. Pinson, *Critical percolation on the torus*, J. Stat. Phys. **75**, 1167 (1994).

[81] M. E. Newman and R. M. Ziff, *Fast Monte Carlo algorithm for site or bond percolation*, Phys. Rev. E **64**, 016706 (2001).

[82] W. Schirmacher, B. Fuchs, F. Höfling, and T. Franosch, *Anomalous magnetotransport in disordered structures: classical edge-state percolation*, Phys. Rev. Lett. **115**, 240602 (2015).

[83] G. Zhang and S. Torquato, *Precise algorithm to generate random sequential addition of hard hyperspheres at saturation*, Phys. Rev. E **88** (2013).

[84] B. J. Brosilow, R. M. Ziff, and R. D. Vigil, *Random sequential adsorption of parallel squares*, Phys. Rev. A **43**, 631 (1991).

[85] A. S. Glassner, J. Arvo, D. Kirk, A. Wexelblat, M. F. Cohen, and R. T. Stevens, *The AP professional graphics CD-ROM*, Vol. 3 (Academic Press, San Diego, CA, 1995).

[86] D. Goldberg, *What every computer scientist should know about floating-point arithmetic*, ACM Computing Surveys **23**, 5 (1991).

[87] J. E. Bresenham, *Algorithm for computer control of a digital plotter*, IBM Syst. J. **4**, 25 (1965).

[88] J. E. Bresenham, *A linear algorithm for incremental digital display of circular arcs*, Commun. ACM **20**, 100 (1977).

[89] J. E. Bresenham, *Algorithms for circular arc generation*, in *Fundamental algorithms for computer graphics* (Springer, Berlin, 1991).

[90] J. Machta, Y. S. Choi, A. Lucke, T. Schweizer, and L. M. Chayes, *Invaded cluster algorithm for potts models*, Phys. Rev. E **54**, 1332 (1996).

[91] B. A. Sanvee, R. Lohmann, and J. Horbach, *Normal and anomalous diffusion in the disordered wind-tree model*, Phys. Rev. E **106**, 081302 (2022).

[92] C. P. Dettmann, *Microscopic chaos and diffusion*, J. Stat. Phys. **101**, 775 (2000).

[93] J. P. Hansen and I. R. McDonald, *Theory of simple liquids* (Academic Press, New York, 1986).

[94] W. Götze, E. Leutheusser, and S. Yip, *Diffusion and localization in the two-dimensional Lorentz model*, Phys. Rev. A **25**, 533 (1982).

[95] E. Leutheusser, *Self-consistent kinetic theory for the Lorentz gas*, Phys. Rev. A **28**, 1762 (1983).

[96] A. Masters and T. Keyes, *Diffusion, percolation, and trapping in the Lorentz gas via variational kinetic theory*, Phys. Rev. A **26**, 2129 (1982).

[97] L. Schubnikow and W. J. de Haas, *A new phenomenon in the change of resistance in a magnetic field of single crystals of bismuth*, Nature **126**, 500 (1930).

[98] P. Deuflhard and A. Hohmann, *Numerische Mathematik* (De Gruyter, Berlin, 2002).

[99] R. Fisch and A. B. Harris, *Critical behavior of random resistor networks near the percolation threshold*, Phys. Rev. B **18**, 416 (1978).

[100] J. Machta and S. M. Moore, *Diffusion and long-time tails in the overlapping Lorentz gas*, Phys. Rev. A **32**, 3164 (1985).

Eidesstattliche Versicherung

Ich versichere an Eides Statt, dass die Dissertation von mir selbständig und ohne unzulässige fremde Hilfe unter Beachtung der „Grundsätze zur Sicherung guter wissenschaftlicher Praxis an der Heinrich-Heine-Universität Düsseldorf“ erstellt worden ist.

Düsseldorf, den 08.11.2022 Benjamin Ahlin Sanvee